Fluorescent proteins for two-photon FLIM analysis of presynaptic protein interactions

Dissertation

zur

Erlangung des Doktorgrades (Dr. rer. nat.)

der

Mathematisch-Naturwissenschaftlichen Fakultät

der

Rheinischen Friedrich-Wilhelms-Universität Bonn

vorgelegt von

Polina Gulakova

aus

Schelesnogorsk, Russland

Bonn, 2019

Angefertigt mit Genehmigung der Mathematisch-Naturwissenschaftlichen Fakultät der
Rheinischen Friedrich-Wilhelms-Universität Bonn

1. Gutachter Prof. Dr. Susanne Schoch
2. Gutachter Prof. Dr. Walter Witke

Tag der Promotion: 8.10.2019
Erscheinungsjahr: 2020

Table of contents

1 Introduction

Proteins are an essential constituent of the organism and participate in almost all processes happening in the cell. Therefore, studying proteins and their interactions is an important topic in biology. Traditionally used biochemical methods detect protein-protein interactions (PPIs), but struggle to monitor their dynamics over time (e.g. upon cell stimulation) and space (differences betoutween cellular compartments). Genetically encoded labeling using fluorescent proteins (FPs) enabled tracking the localization of proteins of interest in living cells via microscopy. Further developments of this approach made it possible to study the PPIs as a measure of interaction between the FPs, attached to them, – the effect called Förster Resonance Transfer (FRET).

1.1 Förster Resonance Energy Transfer (FRET)

Fluorescence is a type of luminescence, which is defined as emission of light from a molecule in an electronically excited state. Fluorescence is characterized by a short light emission (nanosecond range) after absorption of the photon. When the delay is longer (milliseconds to hours), it is called phosphorescence (Lakowicz 2006).

When a fluorescent molecule is irradiated with high-intensity light, its valence electron may be boosted up into a higher energy orbit, resulting in an excited state of the molecule. Relaxation back to the ground energy state can happen through various non-radiative (such as converting the absorbed energy into heat, passing energy to the molecular environment, crossing into the triplet state and returning to the ground state from there) and radiative (fluorescence) pathways (Lakowicz 2006).

The electronic states and transitions between them can be nicely demonstrated using a Jablonski diagram (Jablonski 1933) (fig. 1). Fluorophore can exist at different fluorescent states: non-excited ground state S_0, the first electronic state S_1 etc. (indicated by thick horizontal lines), at each of them there is a number of vibrational energy states (depicted by thin horizontal lines). Radiative (involving absorption/emission of photon) transitions of energy (like fluorescence) are indicated with straight arrows, while the non-radiative transitions (like vibrational relaxation) are indicated with squiggly arrows.

Absorbance of a photon with an appropriate energy amount leads to the excitation of the valence electron to a higher energy level. This is an extremely fast process happening on the order of 10^{-15} s. After absorption the photon usually lands on some higher vibrational level of S_1 or S_2 energy state. It rapidly relaxes to the lowest vibrational level of S_1. It

happens typically by the means of vibrational relaxation (transition from higher to lower vibrational levels) and internal conversion (transition from higher to lower energy states, which is possible if their vibrational levels overlap). These processes have the same mechanics and a quick speed on the order of 10^{-12} s. Another way to give away the energy is the photon emission – a process called fluorescence, it allows returning the electron to the ground energy state S_0. It is usually slow (on the order of 10^{-9}-10^{-7} s), therefore happens after vibrational relaxation and internal conversion. As a result, emitting photon has a lower energy than the absorbed one, which leads to a shift of the emission to a longer wavelength in comparison to the excitation – this phenomenon is called Stokes shift (Stokes 1852) and it defines a principle of fluorescent microscopy. Due to transitions across a number of electronic states with multiple vibrational levels fluorescence emission is distributed across a range of wavelengths. Since relaxation to S_1 level occurs extremely fast, the emission spectrum doesn't depend on the excitation wavelength. Typically, excitation and emission spectra are symmetric, because of the similarity of vibrational states and transitions between them happening during absorption and emission (Lakowicz 2006).

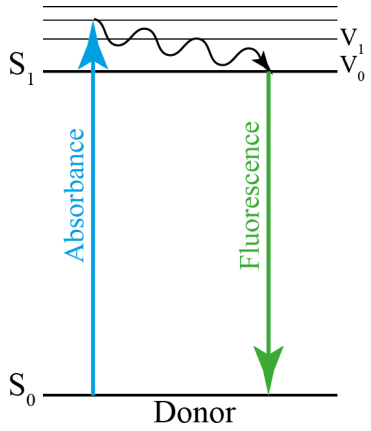

Figure 1. *Jablonski diagram illustrating electronic states S_i, vibrational states V_i and transitions between them. Straight arrows depict absorbance and fluorescence, accompanied with photon absorption and emission, respectively. Squiggly arrows show non-radiative relaxation transitions.*

If the rate of all non-radiative energy transitions is labeled as κ_{nr} and of all radiative transitions as κ_r, then the fluorescence lifetime of a molecule τ, which is the average time it spends in the excited state before returning to S_0, is defined as the following:

$$\tau = \frac{1}{\kappa_{nr}+\kappa_r} \qquad \text{(Equation 1)}$$

Fluorescence emission is a random process and therefore can be described by an exponential decay of intensity *I(t)* (eq. 2).

$$I(t) = \sum_i a_i * e^{-t/\tau_i} \qquad \text{(Equation 2)}$$

Where a is the normalization factor, t is time, τ is the fluorescence lifetime. In the simplest case the fluorescence intensity decay has a single component $i = 1$ (as shown on fig. 2), but for some fluorescent probes the decay is multi exponential $i > 1$. It might happen, for example, if the molecule can adopt several conformations, each of which has its own pattern of energy transitions and therefore individual lifetime components τ_i.

Lifetime is an important characteristic of a fluorophore, describing the time, when 1/e = 36.8% of molecules will return to the ground state. It depends on its intrinsic properties, namely absorbance, emission spectra and extinction coefficient (strength of the light absorbance at a particular wavelength). Local environment, such as pH and ion concentrations, might affect the chemical and physical properties of the fluorescent molecules due to protonation / deprotonation, change in solubility and other effects, which in turn influence the optical properties, leading to alteration of the fluorescence intensity and the fluorescence lifetime (Lakowicz 2006).

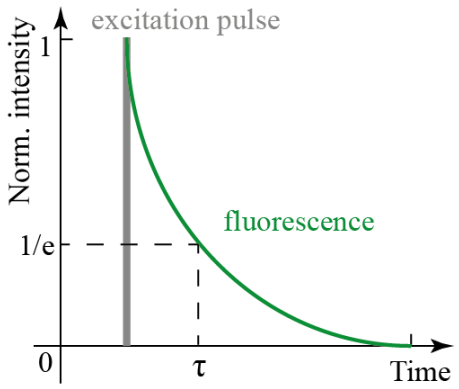

Figure 2. *Intensity decay of the fluorophore upon excitation.*

Electrons are bound to the molecules and are therefore restricted in movement. Usually there is a preferable direction for the electron movement, what creates an electric dipole in the molecule, characterized by the dipole moment. Light is absorbed more effectively, if its electric filed is oriented parallel to the dipole of the fluorophore. Typically, the dipole moment of a fluorophore is larger in the excited state, than in the ground state (Lakowicz 2006).

When the excited fluorophore (called donor) is located in close proximity to a second molecule (called acceptor) in a ground state and the emission spectrum of the donor overlaps with the absorption spectrum of the acceptor, the donor can relax to the ground state by transferring the energy to the acceptor (fig. 3, eq. 3). The excited electron of the donor returns to the ground state simultaneously with the transition of the acceptor electron to an excited state. This process, called Förster Resonance Energy Transfer (FRET), is described by a dipole-dipole coupling between two chromophores and thereby involves

neither direct interaction between electron clouds of the molecules nor emission and re-absorption of the light (Förster 1965). If the acceptor is a fluorescent molecule, then its relaxation is accompanied by the photon emission; if the acceptor is non-fluorescent, than the energy is dissipated as heat.

$$D^* + A = D + A^* \qquad \text{(Equation 3)}$$

The rate of energy transfer κ_{RET} is defined by the following equation:

$$\kappa_{RET}(R) = \frac{1}{\tau_D}\left(\frac{R_0}{R}\right)^6 \qquad \text{(Equation 4)}$$

Where τ_D is the donor lifetime in absence of acceptor, R is the distance between the fluorophores and R_0 is so called Förster Radius, which describes R, at which the efficiency of FRET equals 50%, R_0 is typically in a range 3-6 nm.

κ_{RET} is added to the other non-radiative energy transfers happening to the donor molecule κ_{nr}, increasing its value. Since τ is reverse proportional to the sum of all rate constants (eq. 1), donor lifetime gets decreases upon FRET.

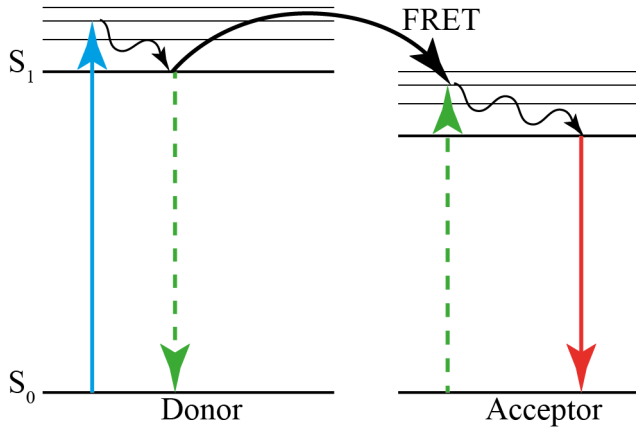

Figure 3. *Jablonski diagram demonstrating a non-radiative process of Förster Resonance Energy Transfer.*

The FRET efficiency E characterizes the percentage of the excitation photons, which contribute to FRET (eq. 5). The higher the FRET efficiency is, the bigger will be the lifetime reduction of the donor.

$$E = \frac{\kappa_{RET}(R)}{\tau_D^{-1} + \kappa_{RET}(R)} = \frac{R_0^6}{R_0^6 + R^6} = \frac{1}{1 + \left(\frac{R}{R_0}\right)^6} \qquad \text{(Equation 5)}$$

FRET efficiency can also be estimated from the donor lifetimes in presence (τ_{DA}) and absence (τ_D) of the acceptor:

$$E = 1 - \frac{\tau_{DA}}{\tau_D} \qquad \text{(Equation 6)}$$

There are some important conditions for FRET to take place (Förster 1965; Lakowicz 2006). (1) Since FRET efficiency is inversely proportional to the 6th power of the distance

between the interacting chromophores *R* (eq. 5), it decreases very fast with the increasing distance, hence the chromophores must be located in a very close proximity to each other (up to 10 nm).

(2) The emission spectrum of the donor and the excitation spectrum of the acceptor must overlap (>30%) (Bajar, E. Wang, et al. 2016).

(3) The chromophores must be located in an orientation suitable for FRET: ideally the chromophore dipoles should be parallel to each other.

Since the FRET efficiency strongly depends on the proximity between the molecules (eq. 5), the Förster Radius R_0 could potentially be a good predictor of *E*. R_0 (nm) could be estimated from the following equation (Lakowicz 2006):

$$R_0 = \sqrt[6]{\frac{9ln10}{128\pi^5 N}\frac{\kappa^2 Q_D J(\lambda)}{n^4}} = 0.02108\sqrt[6]{\kappa^2 n^{-4} Q_D J(\lambda)} \qquad \text{(Equation 7)}$$

Where $N = 6.022*10^{20}$ is Avogardo's number per mmole, *n* is the refractive index of the medium (equals 1.33 for water), κ^2 is the orientation factor for dipole-dipole coupling, Q_D is the donor fluorescence quantum yield, which is a ratio of a number of photons emitted by the donor to a number of absorbed ones; $J(\lambda)$ is the spectral overlap between the donor emission and acceptor excitation spectra.

The angular dependence of the dipole interaction is described by the orientation factor κ^2, which may range from 0 (perpendicular orientation between the two dipoles) to 4 (parallel orientation). It is difficult to calculate it in experimental systems, but usually in biological applications, the unbound FPs freely diffuse inside the cells and orient randomly over time. In these conditions κ^2 is assumed to be 2/3 (a value for the dynamic isotropic random averaging of the donor and the acceptor) (Lakowicz 2006).

The spectral overlap $J(\lambda)$ ($nm^4M^{-1}cm^{-1}$) is defines as follows (Stryer 1978):

$$J(\lambda) = \frac{\int F(\lambda)\varepsilon(\lambda)\lambda^4 d\lambda}{\int F(\lambda)d\lambda} = \frac{\sum_i F_D(\lambda_i)\varepsilon_A(\lambda_i)\lambda_i^4}{\sum_i F_D(\lambda_i)}, \qquad \text{(Equation 8)}$$

Where F_D is the donor emission intensity at wavelength λ_i (nm) across the peak-normalized intensity spectrum, ε_A ($M^{-1}cm^{-1}$) is the molar extinction of the acceptor, calculated for each λ_i (nm) as

$$\varepsilon_A(\lambda_i) = \varepsilon_{at\ \lambda_{exc\,max}} * I_{exc\ norm.to\ I(\lambda_{exc\,max})} \qquad \text{(Equation 9)}$$

The calculated R_0 for the FRET pairs tested in this study are listed in the table 1.

FRET has a large range of applications in studying biological events. One of the first FRET reporters used organic dyes as chromophores. For example, a sensor of cyclic AMP was developed in collaboration between Roger Tsien and Susan Taylor. They observed FRET between fluorescein and rhodamine, which were fused to catalytic and regulatory

subunits of the cAMP-dependent protein kinase A, which would dissociate upon cAMP binding (Adams et al. 1991). However, technical challenges of an organic dyes' application (covalent labeling, delivery into the cells and others) led to an increased interest towards genetically encoded fluorescent labels – fluorescent proteins (FPs), because they can be expressed in a fusion construct with the protein of interest upon DNA manipulations, therefore FPs lack the disadvantages of the organic dyes.

Table 1. *Calculated Förster radii of the FRET pairs tested in this work*

Donor	Acceptor	Max. ε ($M^{-1}cm^{-1}$)	J(λ), $*10^{15}$ ($nm^4M^{-1}cm^{-1}$)	Q_D	R_0 (Å)
mNeon	mRFP	50 000	1.84	0.8	55.01
	TagRFP	100 000	3.85		62.19
	mCherry2	79 400	2.97		59.55
	mRuby3	128 000	4.84		**64.63**
mEGFP	mRFP	50 000	1.43	0.6	50.28
	TagRFP	100 000	3.14		57.32
	mCherry2	79 400	2.32		54.47
mClover	mRuby2	113 000	4.61	0.76	63.54
mClover3	mRuby3	128 000	4.95	0.78	64.59
mCerulean	YPet	104 000	2.55	0.62	55.67
	Venus	92 200	2.36		54.96
mTurquoise2	YPet	104 000	2.50	0.93	59.36
	Venus(L68V)	101 000	2.63		59.87
	mOrange2	58 000	1.46		54.28
	mNeon	116 000	3.04		**61.32**
mTFP1	YPet	104 000	3.00	0.85	60.27
	Venus(L68V)	101 000	3.14		60.73
	mOrange2	58 000	1.74		55.05

1.2 Fluorescent proteins

The discovery of FPs (Shimomura et al. 1962), their cloning (Chalfie et al. 1994) and their evolution (Olenych et al. 2007) (fig. 4) have revolutionized molecular biology, allowing to genetically label proteins of interest and study them in living systems. Furthermore, development of the FP color palette provided an opportunity to use the FRET effect to study interactions between proteins of interest *in vitro* and *in vivo*. In order to underline the importance of the FPs in modern science methodology, scientists O. Shimomura (who first discovered the green fluorescent protein GFP from a bioluminescent hydrozoan jellyfish *Aequorea victoria*), M. Chalfie (who first cloned and expressed GFP) and R. Tsien (who evolved multiple advanced variants of GFP and other color variants) were awarded with the Nobel prize (in chemistry) in 2008 for their pioneering work on the

genetically encoded fluorophores. Nowadays, a broad color palette covers the whole emission spectrum from blue (424 nm) to far-red (655 nm).

1.2.1 Color palette

GFP was the first FP to be genetically expressed (Tsien 1998). The wild type version avGFP had several drawbacks such as tendency to form dimers, pH sensitivity, low photostability, low fluorescence quantum yield and others. These properties of the wild type avGFP lead to a weaker fluorescence, and when a FP is fused to the cellular protein its dimerization might result in a wrong localization and misfunction of the protein of interest, therefore it was important to improve its characteristics. GFP was evolved (fig. 4) by introducing mutations into the protein structure. In particular, brighter versions of avGFP were generated, namely enhanced GFP (EGFP) (Cormack et al. 1995) along with monomeric versions such as mEGFP (Zacharias 2002) and mClover3 (Bajar, E. S. Wang, et al. 2016), probes with increased Stokes shift (Sapphire (Cubitt et al. 1999)), and others. mEGFP and mClover are often used as FRET donors in pairs with orange or red acceptors.

Another direction of the GFP evolution aimed to develop other color variants in order to have an opportunity to label multiple proteins of interest simultaneously. One of the first spectral variants derived from GFP was enhanced blue fluorescent protein EBFP, but due to its low brightness and photostability it is not widely used. Its enhanced versions such as Azurite and SBFP2 perform better and therefore are more promising for multi-color imaging, although they still have a weak tendency to dimerize (Shaner et al. 2007).

Proteins emitting in the cyan region (~470-500 nm) are more widely used for the protein labeling, than the BFPs. The most commonly used variant is enhanced cyan FP (ECFP (Heim & Tsien 1996)), which is often chosen for both multicolor labeling and as a FRET donor (in a pair with a yellow or orange acceptor). It has some spectroscopic disadvantages, such as low quantum yield, low extinction coefficient and double exponential lifetime, that is why a lot of effort was put to evolve FPs with improved characteristics. The resulting proteins were mCerulean (Rizzo, Springer, Granada & Piston 2004a), CyPet (Ohashi et al. 2007), SCFP3A (Kremers et al. 2006), mTurquoise2 (Goedhart et al. 2012) and others. However, new variants also have certain disadvantages, for example, mCerulean and SCFP3A have double exponential lifetimes and decreased photostability, and CyPet is poorly expressed at 37 °C. In comparison to them, mTurquoise2 has a single exponential long lifetime (which is easier to analyze and interpret), high photostability and quantum yield and a faster maturation.

Additionally, new FPs are being identified in other living organisms and the resulting improved FPs have promising characteristics. Among them are the cyan protein mTFP1 from corals *Clavularia sp.* (Ai et al. 2006) and a green protein mNeonGreen from lancelets *Branchiostoma lanceolatum* (Shaner et al. 2013). Both of these proteins are very bright, photostable, have high quantum yields and single exponential lifetimes.

Another useful class of FPs evolved from GFP is the yellow FPs (YFPs), as they are one of the brightest proteins developed; they derive from GFP as a result of the mutation T203Y. The original EYFP mutant has such disadvantages as low photostability, high pH sensitivity, and sensitivity to halides. Further work has been aiming to decrease these drawbacks, in particular, sensitivity to the environment, and such popular variants as mCitrine (Griesbeck et al. 2001) and mVenus (Nagai et al. 2002) were created along with the others. The YPet ("**y**ellow fluorescent **p**rotein for **e**nergy **t**ransfer") variant has even higher resistance to acidic environment than other YFP variants, and was optimized to be the best FRET acceptor so far in pair with CFPs (Nguyen & Daugherty 2005); some papers suggest that the possible explanation of such superior FRET performance is the dimerization with the cyan donor (Ohashi et al. 2007; Vinkenborg et al. 2007).

Despite multiple trials to create orange and red proteins (~560-650 nm) out of the GFP of *Aequorea victoria*, these attempts never succeeded. The red palette was achieved by cloning of proteins from non-fluorescent anthozoan corals and anemones. Natural red proteins are usually obligated tetramers, so great efforts have been made to create monomeric derivatives, which are usually less bright and have slower maturation times. Additionally, they experience green-emitting by-products during maturation (more details in section 1.2.2), which may disturb during multi-color imaging.

One of the first monomeric red proteins created was mRFP (or mRFP1) (Campbell et al. 2002), which was developed from DsRed, the latter is a mammal optimized derivative of drFP583 from a coral *Discosoma sp.* 33 mutations were introduced into DsRed to achieve improved properties of mRFP, however, it still has a small fraction of a green chromophore and a slight tendency to dimerize. Further work has enabled to create a palette of mFruit proteins (562-649 nm) (Shaner et al. 2004): mStrawberry, mOrange, mPlum etc. They all have improved brightness, photostability and maturation characteristics in comparison to mRFP; the most popular among them is mCherry (recently a new version mCherry2 (Shen et al. 2017) was developed).

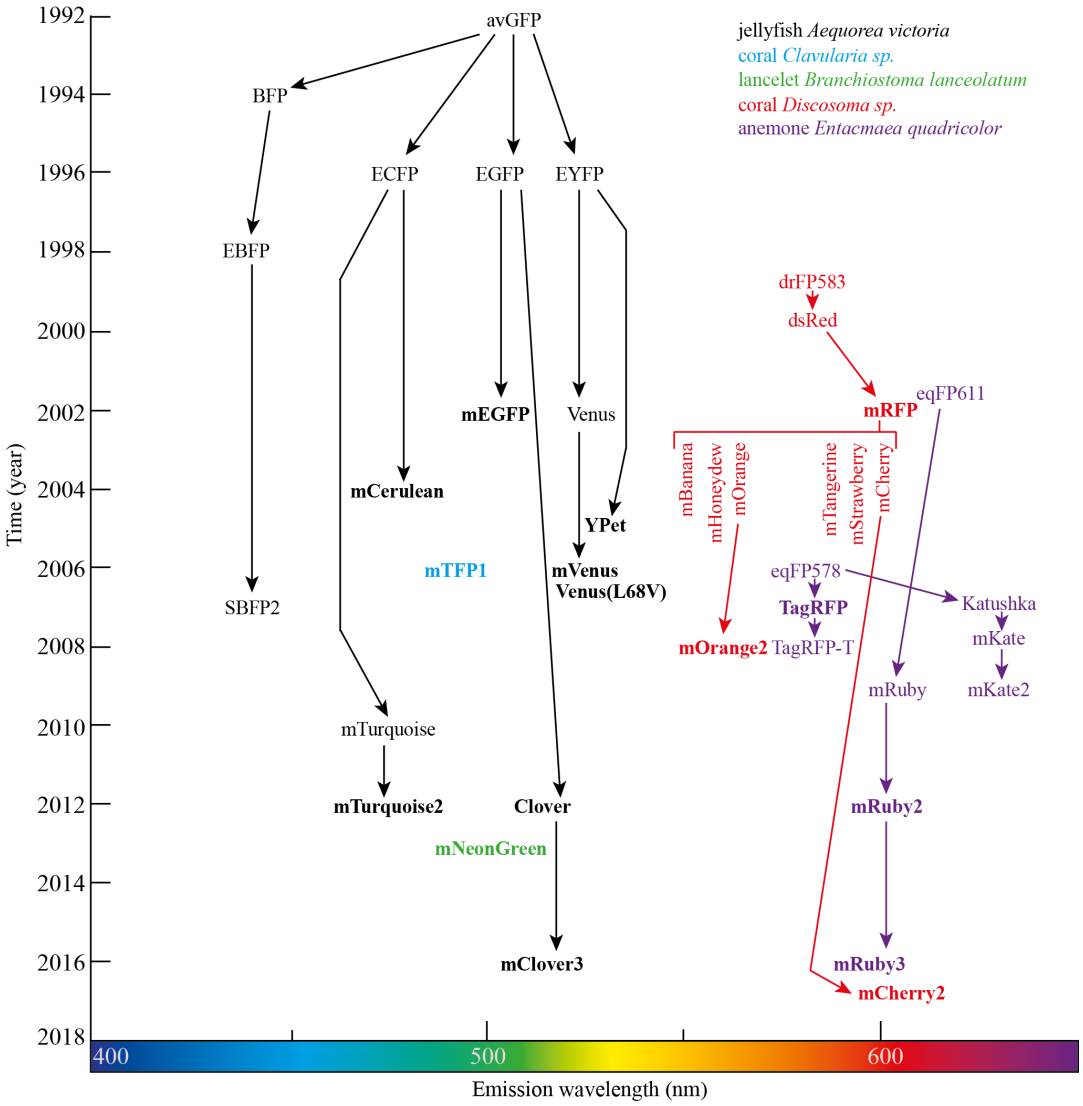

Figure 4. *An overview of the development of some fluorescent proteins, including the ones used in this work (marked bold). Each protein is positioned at the year of its first publication (y-axis) and approximate emission wavelength (x-axis). Font color indicates the organism from which ancestor FP was cloned (see the legend). Modified from (Patterson 2004).*

Another red protein eqFP578 from an anemone *Entacmaea quadricolor* was used to create TagRFP (Merzlyak et al. 2007), which is a bright monomeric protein with a relatively fast maturation, good pH stability, but a relatively low photostability. Shaner et al. have developed mOrange2 and TagRFP-T – variants of mOrange and TagRFP with improved photostability (Shaner et al. 2008).

In order to evolve FPs with improved characteristics, different approaches might be used. One of them is a site-directed mutagenesis, which was applied, for instance, to develop mRFP from DsRed. This method is especially useful when the exact role of certain amino acids is known. For example in case of the FPs from *Aequorea victoria*

mutations F64L and V68L lead to more efficient chromophore formation, whereas S72A, V163A, S175G increase protein folding efficacy (Mastop et al. 2017).

Combination of direct evolution with random mutagenesis and flow cytometry is another approach, which was used, in particular, to develop mFruits (Shaner et al. 2004; L. Wang et al. 2004).

Although a lot is already known about the structure of FPs, some mutations still produce unpredictable results. For example, when monomerizing mutations T122R and 194A were introduced into a red protein eqFP611 from the anemone *Entacmaea quadricolor*, it lost almost all the fluorescence. In order to restore it, 20 other mutations were introduced using site-directed and random mutagenesis. The resulting protein was localized in peroxisomes, and 10 other mutations were needed to achieve cytoplasmic expression. Altogether seven rounds of random mutagenesis and four rounds of multi site-directed mutagenesis were applied to evolve mRuby from eqFP611 (Kredel et al. 2009).

Enormous work has been done to create the existing variability of FPs with multiple promising candidates in each spectral class. However, none of the proteins have all possible characteristics in an ideal way. That's why further evolution of the FPs is relevant. In addition, when choosing the FP, one should take into consideration the conditions and techniques which would be applied (more details in section 1.4). In general, recently developed blue, cyan and green proteins are relatively bright and photostable; yellow proteins are even brighter than GFPs, but unfortunately less photostable; in contrast, orange FPs have a very high photostability; red and far-red proteins are dimmer in comparison to other classes. All the FPs from all spectral classes can potentially aggregate due to poor folding, independently of monomeric characteristics (Shaner et al. 2007).

FPs used in this work and their properties are listed in table 2, their discovery and evolution is briefly shown in fig. 4.

Another powerful class of FPs is optical highlighters – those are proteins, which under illumination with intense light of a certain wavelength can undergo the process of photoactivation (activation from a non-fluorescent, quiescent state) and photoconversion (conversion from one fluorescence emission bandwidth to another one). Photoactivatable and photoconvertable FPs may be a gentle tool for labeling and investigating distinct pools of molecules within a cell in contrast to such techniques as FRAP (fluorescence recovery after photobleaching) and FLIP (fluorescence loss in photobleaching), which require harsh illumination of the region of interest (Shaner et al. 2007).

Table 2. *List of properties of FPs used in this work: maximal excitation and emission wavelengths λ (nm), quantum yield QY, brightness (10^3 $M^{-1}cm^{-1}$), extinction coefficient ε ($M^{-1}cm^{-1}$), pK_a, aggregation. Additionally, amino acids in chromophore, organisms in which wt FP variants were found and the references are mentioned.*

FP	λ_{ex}	λ_{em}	QY	Brightness	ε	pK_a	Aggregation	Chromophore	Organism	Reference
mCerulean	433	475	0.62	26.7	43000	4.7	Weak dimer	TWG	*Aequorea victoria*	(Rizzo, Springer, Granada & Piston 2004b)
mTurquoise2	434	474	0.93	27.9	30000	3.1	Monomer	SWG	*Aequorea victoria*	(Goedhart et al. 2012)
mTFP1	462	492	0.85	54.4	64000	4.3	Monomer	AYG	*Clavularia sp.*	(Ai et al. 2006)
mEGFP	488	507	0.60	33.6	56000	6.0	Weak dimer	TYG	*Aequorea victoria*	(Zacharias 2002)
Clover	505	515	0.76	84.36	111000	6.2	Weak dimer	GYG	*Aequorea victoria*	(Lam et al. 2012)
mNeonGreen	506	517	0.80	92.8	116000	5.7	Monomer	GYG	*Branchiostoma lanceolatum*	(Shaner et al. 2013)
mClover3	506	518	0.78	85.02	109000	6.5	Monomer	GYG	*Aequorea victoria*	(Bajar, E. S. Wang, et al. 2016)
mVenus	515	527	0.64	67.2	105000	5.5	Monomer	GYG	*Aequorea victoria*	(Kremers et al. 2006)
Venus(L68V) = SYFP2	515	527	0.68	68.7	101000	6.0	Monomer	GYG	*Aequorea victoria*	(Kremers et al. 2006)
YPet	517	530	0.77	80.08	104000	5.6	Weak dimer	GYG	*Aequorea victoria*	(Nguyen & Daugherty 2005)
mOrange2	549	565	0.60	34.6	58000	6.5	Monomer	TYG	*Discosoma sp.*	(Shaner et al. 2008)
TagRFP	555	584	0.48	48	100000	3.8	Monomer	MYG	*Entacmaea quadricolor*	(Merzlyak et al. 2007)
mRuby3	558	592	0.45	57.6	128000	4.8	Monomer	MYG	*Entacmaea quadricolor*	(Bajar, E. S. Wang, et al. 2016)
mRuby2	559	600	0.38	42.9	113000	5.3	Monomer	MYG	*Entacmaea quadricolor*	(Lam et al. 2012)
mRFP	584	607	0.25	12.5	50000	4.5	Monomer	QYG	*Discosoma sp.*	(Campbell et al. 2002)
mCherry2	589	610	0.22	17.5	79400	3.3	Monomer	MYG	*Discosoma sp.*	(Shen et al. 2017)

Additionally, optical highlighters may be a useful tool for superresolution microscopy techniques such as PALM (photoactivated localization microscopy) and STORM (stochastic optical reconstruction microscopy), as they rely on recording of sparsely located photoactivatable individual molecules (Betzig et al. 2006; Hess et al. 2006). The first photoactivatable protein PA-GFP (Patterson & Lippincott-Schwartz 2002) was developed from wild type GFP. Despite a large palette of photoactivatable and photoswitchable FPs created since then, an increase of dynamic range and improvement of properties is still required for many of these proteins.

1.2.2 Structure of fluorescent proteins

Although, GFPs and RFPs share a very low amino acid homology (about 20-30%), their tertiary structure is very similar (fig. 5). Monomeric FPs are 4.2 x 2.4 nm cylinders weighing 25-30 kDa and consisting out of 220-240 amino acids. Tetramers consist out of a pair of dimers; each monomer interacts with 2 neighbor monomers and is oriented antiparallel to them, chromophores (parts that are responsible for the color) of neighboring monomers are mirrored relative to each other. The monomer represents a β-barrel out of 11 strands of hydrogen-bonded β-sheets; inside the β-barrel there is an α-helix, containing the chromophore. The barrel is tightly packed, leaving little room for diffusion of small molecules. When looking from above GFP has a ring-shape, whereas RFP has an elliptical shape – this leads to different microenvironments inside these barrels. N- and C-termini of the FP monomers are outside the barrel, therefore, it is easy to fuse a protein of interest to the FP from either side without disturbing the function of the FP (Piatkevich et al. 2010; Shaner et al. 2007).

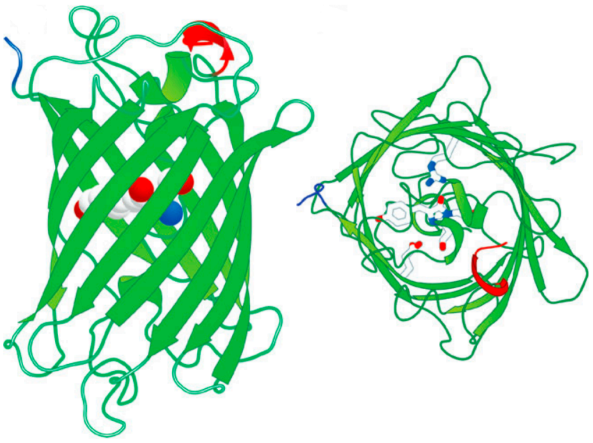

Figure 5. *Schematic structure of GFP – side view (left) and view from the top of the barrel (right), its chromophore and the catalytic residues Arg^{96} and Glu^{222} from (Craggs 2009). Carbon atoms are colored in white, nitrogen in blue and oxygen in red. The N- and C- termini are depicted in red and blue, respectively.*

The chromophore of GFP consists of the amino acids Ser^{65}-Tyr^{66}-Gly^{67}. Only Gly^{67} is essential for chromophore formation and therefore is highly conserved. Tyr^{66} is less conservative and can be replaced by any aromatic group – in particular, this property was used to develop blue and cyan FPs (Tsien 1998).

Along with protein folding, chromophore formation is included into a protein maturation process. Maturation happens auto-catalytically, chromophore formation requires only molecular oxygen. After the β-barrel is formed, amino acids 65-67 undergo through several chemical reactions (fig. 6). First, the nitrogen atom of the peptide bond of Gly^{67} serves as a nucleophile in the attack against the carbon atom of the carbonyl group; as a result cyclization takes place, followed by dehydrogenation of Tyr^{66} performed with the help of the molecular oxygen. The resulting structure with an extended electron conjugation is capable of fluorescing (Olenych et al. 2007).

In case of RFPs the formation of a green intermediate is followed by a second autocatalytic oxidation by molecular oxygen, as a result of which an acyclimine bond is formed, thereby the conjugated π-system gets extended (fig. 7) – in other words the chromophore becomes physically larger, which leads to a longer wavelength emission. In case of natural RFPs and their early derivatives like DsRed the maturation procedure is temperature sensitive, and stable green intermediates are easily trapped, leading to a mixture of different emission colors (Wall et al. 2000; Yarbrough et al. 2001).

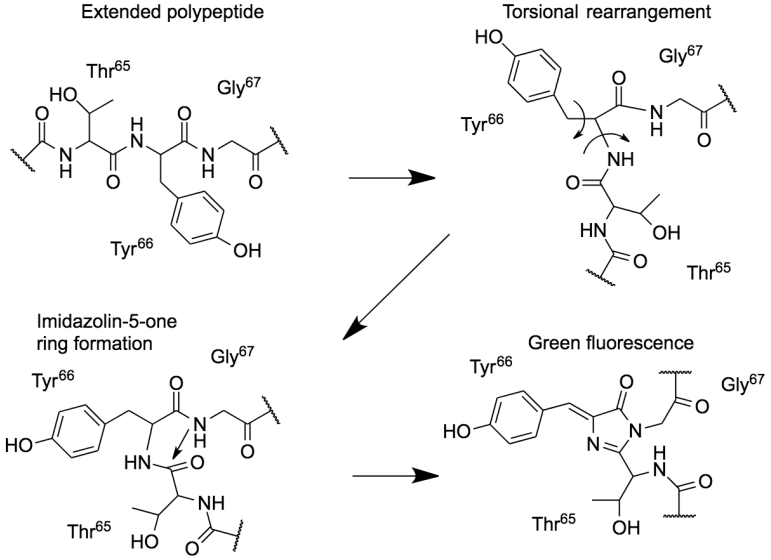

Figure 6. *Schematic diagram of maturation of the EGFP chromophore, from (Olenych et al. 2007). First, the chromophore polypeptide stretches into a linear configuration. Next, a series of torsional adjustments is taking place, as a result carboxyl carbon of Thr^{65} comes into a close proximity to the amino nitrogen of Gly^{67}. Nucleophilic attack by this carbon atom on the amide nitrogen, followed by dehydration, causes the formation of an imidazole-5-one ring system. Finally, molecular oxygen oxidizes the tyrosine α-β carbon bond, resulting in extension of the electron conjugation, leading to the fluorescence occurrence.*

The evolution tree (Shagin et al. 2004) of red proteins has shown, that RFPs appeared relatively recently in several independent lines.

Although the chromophore amino acid sequence is found in many proteins, it doesn't lead to chromophore formation in them, which indicates an essential role of the protein tertiary structure in chromophore maturation. In particular, amino acid alignment of multiple proteins has shown that 4 amino acid residues remain highly conservative in FPs: Tyr^{66}, Gly^{67} from the chromophore, Arg^{96} and Glu^{222} (numbering according to avGFP). Arg^{96} performs a catalytic function for chromophore formation, stabilizing the intermediate products (Wood et al. 2005; Sniegowski et al. 2005), Glu^{222} apparently plays a similar role, although exact steps should still be confirmed with further experiments (Craggs 2009).

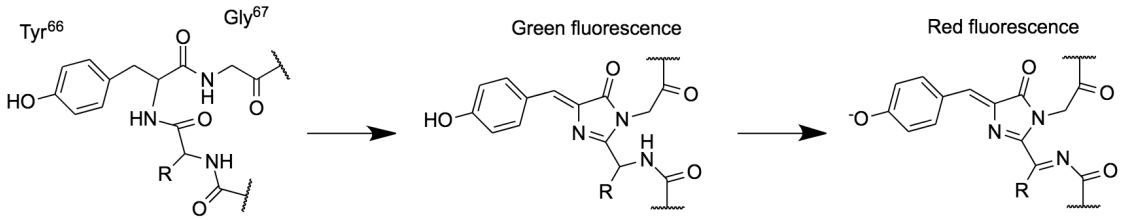

Figure 7. *Scheme of two-step maturation of RFPs from (Remington 2006), resulting in extended electron conjugation.*

The microenvironment around the chromophore affects its properties. For example, the chromophore Met-Tyr-Gly demonstrates a wide 175-nm emission range from AmCyan1 (486 nm emission, mutant of amFP486 (Matz et al. 1999)) to far-red AQ14 (663 nm (Shkrob et al. 2005)), including ZsGreen1 (Matz et al. 1999), TagRFP (Merzlyak et al. 2007), mCherry2 (Shen et al. 2017) and others.

Continuing efforts in a search of the new FP variants in nature along with the protein engineering of already existing FPs should further expand the color palette and optimize the other characteristics of FPs.

1.3 Application of FPs and FRET

FPs are widely applied for labeling and tracing proteins of interest. Unlike traditionally used approaches (some of which will be explained in section 1.3.1), protein labeling with FPs allows performing experiments in living cells, studying them in dynamic environment and tracing them on subcellular level.

The development of a fluorescent color palette has allowed multi-color imaging, as well as other applications (including the ones based on the FRET effect), which enforced and broadened the possible tools, used by the researchers.

1.3.1 Protein-protein interactions

One of the most commonly used applications in biology, involving FRET between FPs, is the study of interactions between proteins of interest.

Protein-protein interactions (here and further PPIs) are involved in most of the processes in cells: cell survival, proliferation, cell growth, motion, morphology, communication and so on. That's why PPI studies are important to understand how the living organisms function on a molecular level.

PPIs vary in strength, duration and speed of interaction, depending on their role in certain cellular processes. For example, permanent interactions characterize multi-subunit complexes, which carry out structural or functional roles. Whereas transient interactions are temporary, and they typically need a biological context in order to happen, such as phosphorylation, conformational change etc., therefore they are usually involved in some biochemical cascades. Transient interactions may be fast or slow, strong or weak. PPIs happen in certain areas of proteins called binding domains. Such domains have varying length, specificity, binding strength and have a specific tertiary structure, which allows binding of the interacting partner (Nooren & Thornton 2003; Perkins et al. 2010).

There are multiple methods, created to detect and investigate PPIs, some of which will be listed further. All the methods have their advantages and disadvantages, that's why one should think carefully about the purpose of their study before choosing the method to apply.

The most popular technique to study PPIs is co-immunoprecipitation (here and further co-IP) (Phizicky & Fields 1995). It is based on the isolation of the protein of interest using a specific antibody and the subsequent identification of its interaction partners by Western blotting. In case of absence of a good antibody, one may choose a pull-down assay; the difference from co-IP is that the protein of interest is bound to agarose beads. Both these methods are useful for the detection of stable and strong interactions. It is also possible, that they would detect indirect interactions.

In case of a transient weak or fast interaction one may use a chemical cross-linking, which allows creating covalent bonds between interacting partners. For certain approaches, cleavable or photo-activatable cross-linkers might be helpful (Phizicky & Fields 1995).

Pull-down assays (Lucas 2004) and cross-linking may be applied for screening for interaction partners: in this case, they could be combined with mass-spectrometry to identify the binding proteins. High throughput screening with direct information about the sequence of interacting partners is achieved with such methods as phage display and two-hybrid system (Phizicky & Fields 1995). In both these approaches, one creates libraries of polypeptides expressed in the cell type / organism of interest. In case of yeast two-hybrid system, the protein of interest is fused to a transcription factor e.g. Gal4-binding domain, and tested proteins are fused to the transcriptional activation domain. When co-expressed in the same cell, their interaction leads to activation of the marker (LacZ) encoded in the mutant host yeast cell. Next, the plasmids of the labeled cells are purified and sequenced. In the phage display method, a polypeptide library is fused to a coat protein (pVIII or pIII) of phage M13; after infection of *E. coli*, the expressed library is located on the outer membrane. The library is enriched by binding to the immobilized target and sequenced. Both these methods have multiple modifications, for example – different host organisms (when proteins of interest require post-translational modifications). They are good for a rough initial screening for potential interacting partners, which should be verified due to a high number of false positive results.

When the binding partner is known, and one needs to investigate the interaction in details, namely the dynamics of ongoing interaction on a subcellular level in living cells, the usage of FPs would be a good option. Two FPs – a donor and an acceptor of FRET – should be fused to the proteins of interest; when the proteins of interest interact, the FPs come close enough for FRET to take place (fig. 8). FRET may be detected via various microscopy approaches, based on the measurement of spectroscopic characteristics or the lifetime (described in details in section 1.4 below), and is therefore a sign (and under certain circumstances also a measure) of interaction between the proteins of interest (Sekar & Periasamy 2003).

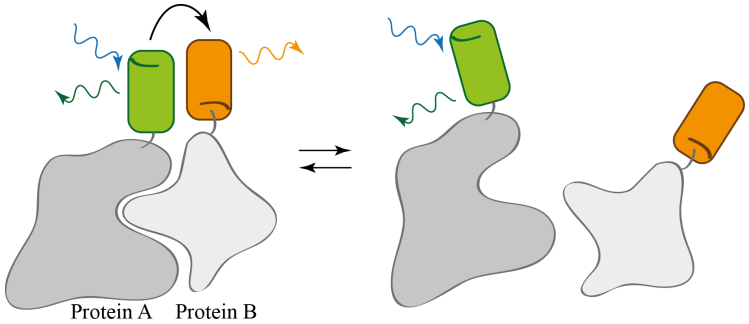

Figure 8. *Scheme of protein-protein interaction studies, using fluorescent proteins, attached to the proteins of interest. FRET between the FPs reports interaction between the proteins of interest.*

The necessity of close proximity between the FPs for FRET, on one hand, increases the specificity of the method by decreasing a chance of false positive signal. On the other hand, it gives restriction for the fusion of the FPs and the proteins of interest. The FRET signal might be absent even if the proteins of interest interact, if FPs attached to them are located too far from each other or are not properly oriented (fig. 9). Such potential risk might be especially critical when working with large multi-domain proteins.

Figure 9. *FRET between FPs attached to interacting proteins of interest takes place, if the FPs are in close proximity and are appropriately oriented to each other.*

However, the advantages of this approach overcome the technical issues, as one may investigate both strong and weak interactions in natural conditions in living cells, which is hard or sometimes impossible with traditional methods mentioned earlier. This technique doesn't require strong overexpression of the proteins of interest, it is noninvasive and nondestructive, it may be performed in living cells – *in vitro* or even *in vivo*. The latter allows performing experiments in conditions close to natural, allowing tracking the same protein molecules and the same cells over time, reducing the amount of samples needed (Lakowicz 2006). Furthermore, FRET-based methods are advantageous over the multi-color imaging in regard of the protein-protein interaction studies, because they exclude co-localization of the proteins of interest, as FRET requires such a close proximity, which is usually possible only between interacting molecules.

Therefore, FRET-based approaches for PPI studies have become a popular method in biology and were used to study in detail, for example, the interactions of SNARE proteins with each other (Degtyar et al. 2013; Takahashi et al. 1AD) and with other proteins (Rickman & Duncan 2010; Burré et al. 2014), the functioning of receptors (Laviv et al. 2011; Doré et al. 2014; Aow et al. 2015) etc.

1.3.2 Biosensors

A modification of the FP-based approach was the development of biosensors – reporters of biological events. Biosensors may detect and reflect changes in the cellular / subcellular

environment, certain signaling pathways, reorganization of cytoskeleton and other phenomena.

Biosensors may be single FP-based, and this FP would be quenched or enhanced depending on the presence or absence of a certain molecule. Examples of such sensors are a series of Ca^{2+} sensors GCaMP (Ye et al. 2017; Yang et al. 2018), a dual pH and Cl^- sensor ClopHensorN (Raimondo et al. 2013), voltage sensor ArcLight (Borden et al. 2017), glutamate sensor iGluSnFR (Marvin et al. 2013; Marvin et al. 2017).

However, biosensors might also involve FRET between FPs (fig. 10). The principle is the same as used for PPI studies, just in this case the interaction is a marker of some process, happening in the cell. Examples of such biosensors are Rho GTPases called RhoA and Cdc42, which are involved in the reorganization of the actin cytoskeleton in spines upon stimulation and used to study long-term synaptic plasticity in neurons. RhoA and Cdc42 could be fused to a donor FP, and upon activation they would bind their partner proteins Rhotekin and Pak3, respectively (fig. 10 panel D), and thereby generate FRET effect, which marks long-term potentiation (Murakoshi et al. 2011).

Even more frequently biosensors are based on intramolecular FRET (fig. 10 panels A-C), when two FPs are attached to the same core and FRET takes place / disappears upon conformational changes of the core. Such sensors are especially popular for studying protein kinase activity (Oldach & Zhang 2014). Camuiα (Lee et al. 2009; Shibata et al. 2015) is a reporter of activity of the protein kinase CaMKIIα, and it is used to study long-term potentiation and the underlying Ca^{2+} signaling dynamics. Donor and acceptor (typically mEGFP and mCherry) are attached to CaMKIIα on N- and C-termini, and the lifetime of the donor increases upon the activation of the kinase. A group of sensors was developed to study cAMP signaling: those are Epac-camps (Nikolaev et al. 2004; Klarenbeek et al. 2011) and ICUEs (DiPilato & Zhang 2009). Another example is the protein kinase A (PKA), whose activity may be investigated either by the conformational changes of the AKAR sensors (Allen & Zhang 2006; Chen et al. 2014), consisting of a surrogate substrate of PKA and the phosphoaminoacid binding domain PAABD; or through its interaction with AKAP79/150 protein (Smith 2006).

It is possible to use several types of biosensors at a time, investigating different processes simultaneously or monitoring cell response to the stimulus on different levels. For this purpose signals from multiple FRET pairs should be well separated (Laviv et al. 2016).

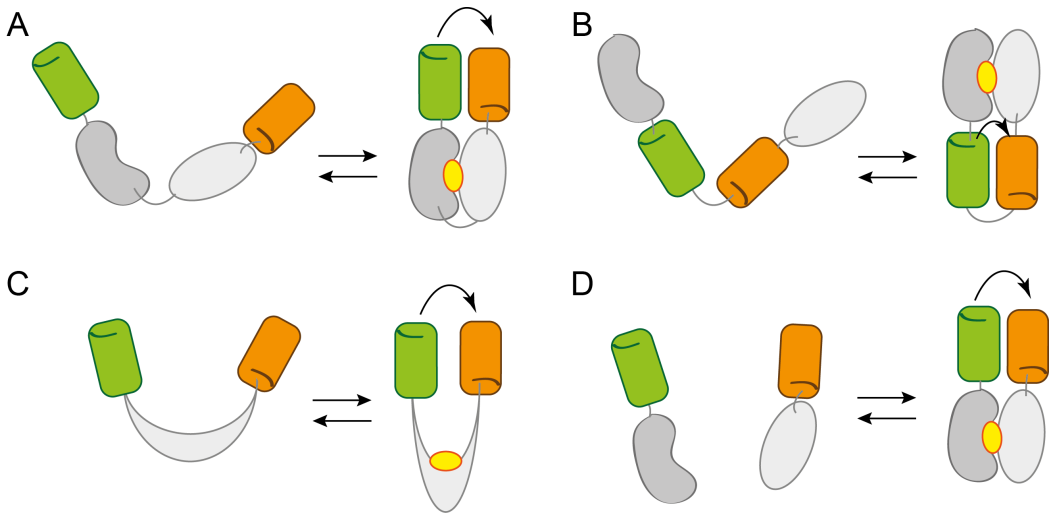

Figure 10. *Scheme of FRET-based unimolecular (A-C) and bimolecular (D) biosensors. Biosensors include a sensing unit (grey) and a reporting unit – FPs (green and orange cylinders). Sensing unit recognizes a biological event, such as ligand binding or phosphorylation (yellow oval), which leads to conformational change (A, C) or binding to a different segment (B, D), resulting in FRET between the attached FPs (curved arrow). Modified from (Zhou et al. 2012).*

1.4 Methods of FRET detection

Typically, FPs are monitored using a fluorescence microscopy. The simplest microscope model requires a source of light, a magnifying lens and an acquisition device. Since fluorophores have characteristic excitation and emission spectra, one should place an excitation filter before the sample and an emission filter behind the sample. It is important to, firstly, decrease the excitation light contamination of the emitted signal, and secondly, to increase the specificity of the fluorophores being excited and the signal being collected respectively.

Wide-field microscopy is the simplest technique, which could be applied, for example, to monitor Ca^{2+} signaling (Miyawaki et al. 1997) or dynamic protein kinase activity in single living cells (Ting et al. 2001). The main disadvantage of the wide-field microscopy is generation and registration of the out-of-focus signals.

Nowadays it is getting more common to use confocal and multi-photon laser microscopy, which lack this drawback. Lasers produce high intensity, monochromatic light, therefore an excitation filter is not required in such systems. The camera is usually replaced by a photomultiplier tube (PMT), which multiplies the signal of the detected photons. Confocal microscopy allows imaging of deeper areas of the specimen in comparison to wide-filed microscopy, but is limited to defined excitation laser wavelengths. Multi-photon microscopy avoids this limitation by using tunable infrared

lasers (700-1000 nm). Besides, it provides an even deeper penetration into the specimen, reduced photobleaching and increased cell viability (Sekar & Periasamy 2003).

There are different approaches, how FRET might be detected using fluorescence microscopy. Spectrally resolved microscopy techniques (sections 1.4.1-1.4.4) give advantage in discrimination of different fluorophores, whereas lifetime-based methods (section 1.4.5) allow discrimination of different fractions of the same fluorophore in different states of interaction.

1.4.1 Acceptor photobleaching

When two FPs are co-localized and correctly oriented, FRET might take place – the donor FP would transfer its energy to the acceptor FP. If the acceptor is photobleached, FRET will be interrupted and the fluorescence of the donor will be increased. The difference of the donor fluorescence intensity before and after photobleaching is used to calculate the FRET efficiency E:

$$E = 1 - \frac{I_{D,pre}}{I_{D,post}} \qquad \text{(Equation 10)}$$

The advantages of this approach are its simplicity, accuracy and the possibility to use almost any microscope with a powerful enough light source. This method has a good spatial resolution, allowing resolving local variations of FRET efficiency.

However, there are some disadvantages, which limit the application of this approach. Firstly, it is important, that only the acceptor is bleached, that's why it is preferable to use appropriate excitation filters. This method is not applicable for multi-photon microscopy, because multi-photon cross-sections of fluorophores (which is a probability of multi-photon absorption) are typically broader, than the one-photon absorption spectra; as a result it is usually impossible to selectively excite the acceptor. Another disadvantage is that some fluorophores are known to photoconvert to other spectral forms during photobleaching (Kremers et al. 2009), which might lead to incorrect FRET estimation. Furthermore, the temporal resolution is not very high, because acceptor photobleaching requires some time. Additionally, since photobleaching is irreversible, this method is inappropriate for dynamic studies. Moreover, in living cells, acceptor fluorescence might be recovered relatively fast due to diffusion of the FPs from not photobleached areas. Finally, the sample might be damaged by the high intensity light, therefore the application of this method in living cells is constrained.

1.4.2 Photoactivation

In a similar approach one uses photoactivatable FPs (PA-FPs) as acceptors for FRET, for example PA-GFP with a CFP donor (Patterson & Lippincott-Schwartz 2002). When PA-GFP is in a dark state, it cannot accept energy, but after a brief strong illumination it gets activated and switches to a fluorescent state; if it is close enough to the donor at this moment, it might accept the FRET energy. Using this method one might investigate dynamic interactions in living cells, however efficiency of the photoactivation could be a limitation factor (Demarco et al. 2006).

1.4.3 Sensitized emission

In a different approach one takes profit of the fact that the acceptor gets excited by the donor via FRET: in this case one tries to selectively excite the donor, and the acceptor channel is measured. Both the amount of FRET and the amount of the acceptor molecules determine the strength of the acceptor signal. To correct for this, a second image, where only the acceptor is excited and imaged, is taken and used to normalize the first FRET image.

However, due to spectral overlap it is impossible to excite the donor exclusively, so the acceptor fluorescence due to FRET will be contaminated with the direct excitation of the acceptor. Moreover, donor emission may also be partially detected in the acceptor channel. These crosstalk events are called spectral bleed-through (SBT, fig. 11) and they require correction of the FRET signal. Typically, it is important to use two control samples, containing only donor and only acceptor. They both should be excited using the donor excitation settings, and the emission signal in the acceptor channel should be collected from both control samples to estimate the value of the SBT. After the experimental sample is imaged, the control measurements should be subtracted – and the resulting fluorescence is considered to be the FRET signal (Berney & Danuser 2003).

Careful selection of the filters, mirrors, excitation source and calibration approach is required for this method. For example, two-photon microscopy is not very appropriate here, due to large two-photon cross sections of the majority of the FPs (Drobizhev et al. 2011; Drobizhev et al. 2009).

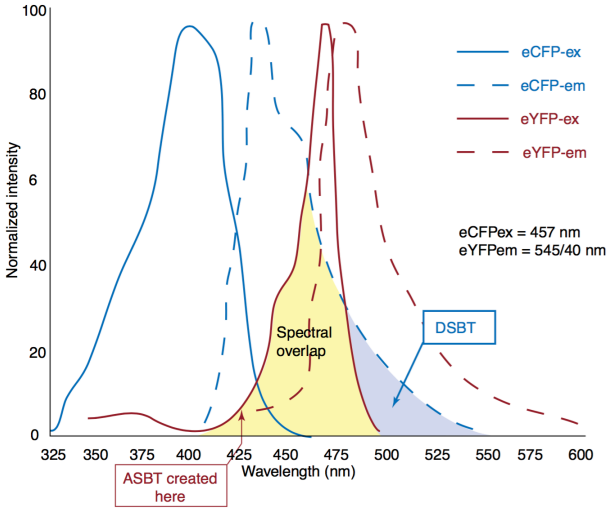

Figure 11. *Excitation (solid lines) and emission (dashed lines) spectra of a FRET pair of enhanced cyan (eCFP) and yellow (eYFP) fluorescent proteins show a good overlap (marked yellow). SBT is a combination of ASBT (acceptor spectral bleed-through) and DSBT (donor spectral bleed-through). From (Wallrabe & Periasamy 2005).*

1.4.4 Spectral imaging methods

Spectral imaging microscopy (Day & Davidson 2012; J. Kim et al. 2011) allows creating λ stacks, which are images acquired over a broad range of emission wavelengths. It gives a possibility to analyze the fluorescent spectra in each pixel location of the image.

The donor in the sample gets excited, the donor and the acceptor emission signals are collected across the spectral range. A spectrum acquired from a control sample, where only the donor is expressed, is later used to remove the donor emission from the image – a procedure called linear unmixing. Direct excitation of the acceptor is neutralized by the SBT correction approach, described in the section 1.4.3.

Spectral imaging methods could be applied for the experiments in living cells, including studies of dynamic processes. However, the necessity of separate control samples for the SBT corrections is a drawback of this method.

1.4.5 Time-resolved fluorescence

A totally different approach is achieved with FLIM – fluorescence lifetime imaging microscopy (Piston & Kremers 2007; Sun et al. 2011). This technique is based on the lifetime τ measurement, which is the average time the fluorophore stays excited after photon absorption before returning to the ground state. Lifetime is an intrinsic characteristic of a fluorophore, and it depends on the local environment: concentration of ions, pH, etc.

FLIM measures the spatial distribution of the donor lifetimes. Since FRET is a quenching process that decreases the population of the donor molecules in the excited state, FRET shortens the donor lifetime (fig. 12, more details in section 1.1). This effect is used for the FRET efficiency estimation:

$$E = 1 - \frac{\tau_{DA}}{\tau_D} \qquad \text{(Equation 6)}$$

Where τ_D and τ_{DA} are the donor lifetimes in absence and presence of the acceptor respectively.

Unlike other methods, which aim to separate signals from different fluorophores (donor vs. acceptor), FRET-FLIM is sometimes capable to discriminate different fractions of the same fluorophore (donor) in different states (experiencing and not experiencing FRET).

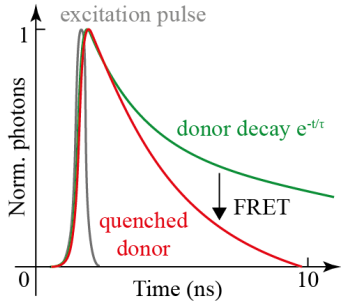

Figure 12. *Donor intensity decay curves in presence and absence of the acceptor for the time domain FLIM method (section 1.4.5.1). A fast laser pulse excites the donor, the emitted photons are detected and the intensity decay is measured. Donor lifetime may be estimated by fitting the decay with a mono exponential or double exponential model. In presence of the acceptor the decay gets faster and the lifetime becomes shorter.*

FLIM lacks serious disadvantages of the steady-state intensity-based approaches, namely lifetime is independent of the fluorophores' concentrations, excitation intensity and unintended photobleaching. Moreover, under certain conditions the FRET-FLIM approach is able to provide information about distances as well as interacting and noninteracting fractions of proteins (Berezin & Achilefu 2010).

Measurement of the lifetime changes using FLIM may be applied to study various effects and events (Becker 2012), for example:

1. Lifetime change of a fluorescent biosensor by various ions, such as Ca^{2+} and Cl^-, which are especially important for the nervous system (Kaneko et al. 2004; Funk et al. 2008; Kuchibhotla et al. 2009);
2. Oxygen effects on the fluorescence lifetime of the endogenous fluorophores nicotinamide adenine dinucleotide (NADH) and flavin adenine nucleotide (FAD) (Chance et al. 1979);

3. Change of the fluorescence lifetime upon binding of the fluorophore to the biological target. For instance, nucleic acid dye SYTO13 demonstrates same spectral characteristics but different lifetimes when bound to DNA and RNA (van Zandvoort et al. 2002); FPs may have a slightly different lifetime when attached to a protein of interest (Treanor et al. 2005);
4. Many fluorescent molecules may be used as pH indicators, as their protonated and deprotonated forms show different lifetimes (Sanders et al. 1995; Hanson et al. 2002);
5. "Molecular rotors" allow measuring local viscosity, as the rotation inside the fluorescent molecules creates a nonradiative decay path (Kuimova et al. 2008; Levitt et al. 2009);
6. FRET between two fluorescent molecules as a measure of protein-protein interactions or protein conformation change (see section 1.3). This is the most widely used application of the FLIM technique;
7. And others.

FLIM also has some limitations, as it requires expensive equipment and some understanding of the lifetime physics for the analysis and interpretation of the results. Additionally, it is preferable to apply this method to live specimens, because fixation and especially mounting may cause significant fluorescence lifetime changes (Joosen et al. 2014).

FLIM techniques can be roughly classified into the frequency domain (FD) and the time domain (TD) methods.

1.4.5.1 Time domain (TD) FLIM

Time correlated single photon counting (TCSPC) FLIM (Becker 2012; Lakowicz 2006) is based on the precisely timed registration of the arrival times of single photons from a fluorophore in respect to a reference signal, usually the light source. It is nicely compatible with confocal and multi-photon laser scanning microscopes; an important requirement is that the illumination is given by a focused beam of high-frequency pulsed laser, because a sufficient amount of photons is required for the data fitting.

The principle of the TCSPC method may be compared to a stopwatch (fig. 13). The clock starts when the light source sends a pulse to the sample and stops, when the photon from the sample reaches the detector. Both the photon and its arrival time after the pulse generation are recorded. Then the next pulse is given, and the clock starts again. After millions of trials the resulted data is summarized in a histogram of arrival times.

Each photon may be emitted from the sample at a random time point, however there is a certain probability of the event to happen, which is depicted as the distribution of the arrived photons over time (fig. 13 panel C); this probability is specific for each chromophore and is characterized by the lifetime value. For a homogenous population of molecules the resulting fluorescence decay histogram is a single exponential function:

$$F(t) = I_{t=0}e^{-t/\tau} \qquad \text{(Equation 11)}$$

This lifetime measurement may be performed in every pixel of the image, leading to a three-dimensional data array: pixel, located in (x, y) spatial coordinates, contains photons, distributed in a large number of time channels, which represent consecutive times after the excitation pulses.

This approach allows reaching a high time resolution and an accurate lifetime measurement. TCSPC is also able to resolve complex lifetime decays; it is applicable for studies of dynamic processes.

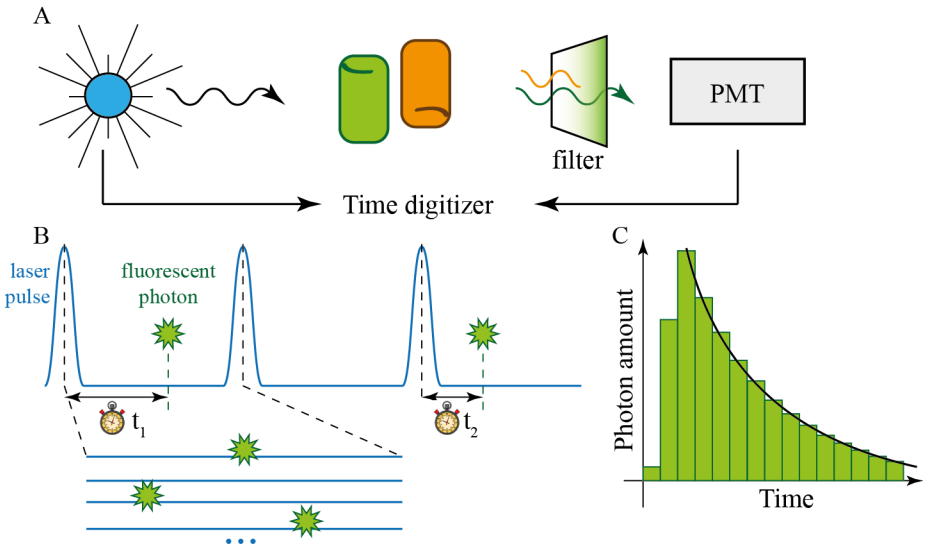

Figure 13. *The principle of TD FLIM. A – Pulsed excitation light source is coupled to the microscope scanning system. Photons from the FRET donor pass the filters and arrive to the fast detector, coupled to the TCSPC device. B – Not more, than one photon should arrive to the detector after the laser pulse. Arrival time of each photon is registered to build a histogram of the photon arrival probability (C) in each pixel of an image. Modified from PicoQuant Technical Note (Wahl 2014).*

In practice, the time resolution of the measuring system is limited. Overall time precision of the system is characterized by the so-called instrument response function (IRF) of the light source, detector and electronics, IRF is measured as a response of the system to the excitation pulse itself in an additional experiment. Measured signal is actually a convolution between the exponential decay of the chromophore's fluorescence and the IRF:

$$d(t) = IRF(t) \otimes F(t) \qquad \text{(Equation 12)}$$

Two-photon pulsed lasers are often used for FLIM systems, as they create discrete and consistent pulses of light. The principle of two-photon excitation is based on the idea, that two photons of low energy (typically infrared) may excite a fluorophore in one quantum event. Since the excitation requires two photons, located spatially and temporarily close to each other, the resolution in *0Z* dimension is improved, and out-of-focus objects are almost not excited; in such case additional elements (such as pinholes) are not needed. Usually the distance between light pulses in two-photon lasers is 12.5 ns, whereas the typical lifetime of the FPs is in the order of a few nanoseconds. Long wavelength excitation of the two-photon lasers leads to low tissue absorbance, deep imaging and low autofluorescence of the tissue – making two-photon microscopy advantageous for *in vivo* studies (Drobizhev et al. 2011).

The signal is detected by a high-sensitive detector, typically by a photon-multiplier tube (PMT). It has such advantages as high sensitivity and speed, low noise and a high dynamic range.

Various analyses approaches have been developed to extract the lifetime information from the measured data. The most widely used of them is the least square iterative re-convolution, which is explained in details in Methods (section 2.4.6). In brief, the theoretical exponential decay curve is convolved with the IRF and compared with the measured curve; this action is repeated until the fitting parameters are optimized. This procedure is repeated for all pixels of the image (O'Connor & Phillips 1984).

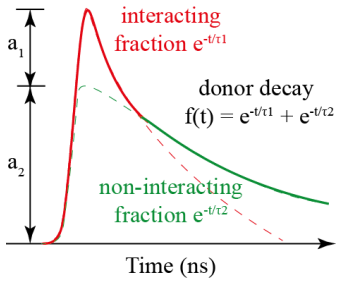

Figure 14. *Double exponential decay of the FRET donor might consist of two fractions: one, which is interacting with the acceptor, and the non-interacting one.*

The simplest model is a single exponential decay function, described by a single lifetime (eq. 11). However, in practice the decay profiles are usually modeled by multi-exponential functions (fig. 14), described by several lifetimes τ_i and amplitudes a_i (eq. 2). There might be different reasons for it, for example a donor fraction with slow lifetime might represent molecules not experiencing FRET. In more details possible reasons for double exponential donor decay will be explored in Results and Discussion.

The final FLIM image is obtained by assigning the brightness in the pixel to the photon number and the color to the selected parameter, for example average lifetime τ_M or interacting fraction a_i.

1.4.5.2 Frequency domain (FD) FLIM

In the other type of approach (Becker 2012) the excitation light is modulated or pulsed at a certain frequency, and this modulation pattern will be reproduced by the fluorophore with a delay in time (phase-shift $\Delta\varphi$) and decrease of the signal amplitude (modulation depth M), caused by the fluorescence decay of the excited fluorophore (fig. 15).

In order to extract information about the phase shift and the modulation depth, one usually uses the heterodyne detection method: the sensitivity of the camera or the detectors is modulated (or gated) by an oscillator frequency f_{osc}, which is slightly (a few hundred to a few thousand Hertz) different from the laser pulse or modulation frequency f_{laser}. The difference in frequencies $f_{\text{laser}} - f_{\text{osc}}$ is then used for the phase shift and the modulation depth estimation. In the homodyne method the detector is modulated at the same frequency as the excitation light. Since both modulation and phase of the emission are related to the characteristic decay time, two independent values for the lifetime may be determined with the frequency domain (FD) method.

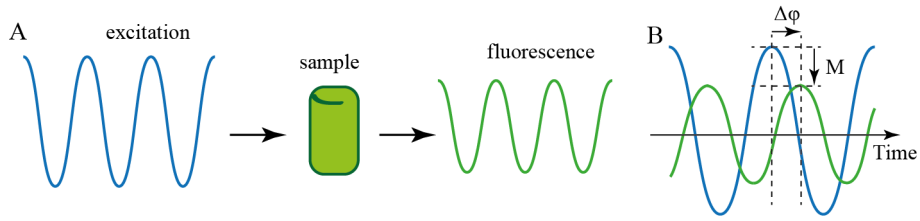

Figure 15. *The principle of FD FLIM. A – The excitation light is modulated at a certain frequency, the fluorescence emission is registered by the detector. B – the phase delay Δφ and the modulation depth M are used to estimate the fluorescence lifetime.*

An effective analysis method, especially useful for multi-exponential decays, is provided by the phasor approach (Digman et al. 2008) In this approach the lifetime is not determined for every pixel. Instead, the phase shift $\Delta\varphi$ and the modulation degree M are used to create a polar plot (fig. 16), where each pixel of the image is transformed to a point of the phasor plot by assigning the phase to the angle of the pointer and the modulation degree to the amplitude. For a modulation frequency ω the coordinates (s; g) of each point are defined as followed:

$$g(\omega) = M\cos(\Delta\varphi) \qquad \text{(Equation 13)}$$

$$s(\omega) = M\sin(\Delta\varphi) \qquad \text{(Equation 14)}$$

Single-exponential lifetime decays land on the semicircle; the exact location depends on the lifetime. Multi-exponential decays fall inside the semicircle. If the process is the result of the convolution of several events, for example of the fluorescence decay and the FRET-induced decay, then the phasor ends inside the semicircle (fig. 16 panel B). Points on the phasor plot can be back-annotated in the FLIM image by color-coding.

The TD and FD methods are related via the Fourier transform, that is why phasor plot can also be applied for data acquired with TD approach by means of the following transform of the decay trace *I(t)*:

$$g(\omega) = \frac{\int_0^\infty I(t)\cos(\omega t)}{\int_0^\infty I(t)} \qquad \text{(Equation 15)}$$

$$s(\omega) = \frac{\int_0^\infty I(t)\sin(\omega t)}{\int_0^\infty I(t)} \qquad \text{(Equation 16)}$$

Where ω represents the laser repetition angular frequency and is estimated by multiplying the laser repetition rate by 2π.

Advantage of the phasor plot is an easy visualization of the raw information (without application of the decay models) about different donor species, for example experiencing and not experiencing FRET.

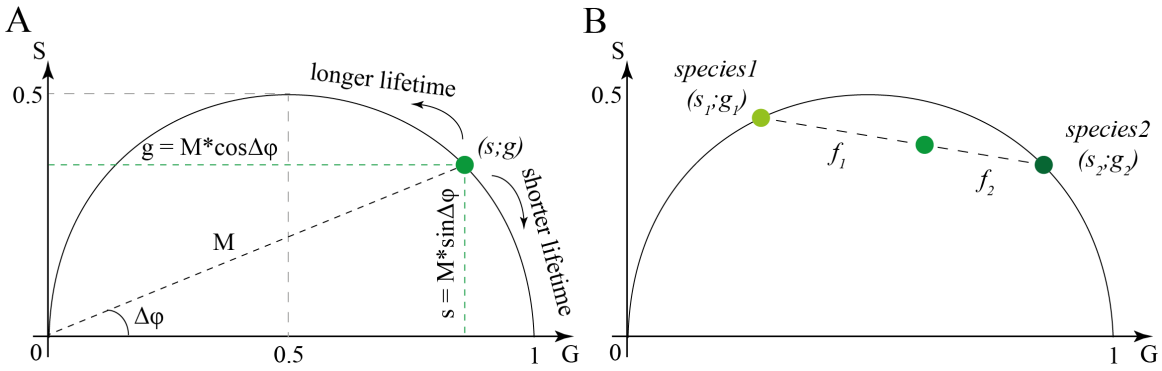

Figure 16. *Scheme of a phasor plot. A – a single decay component is represented by a point (s;g) on a semicircle. B – a mixture of two species falls inside the semicircle; contribution of species1 is $f_1/(f_1+f_2)$. Modified from (Szmacinski et al. 2014).*

An advantage of the FD approach is a faster lifetime acquisition, whereas the TD technique has a higher signal-to-noise ratio for low-concentration samples and therefore is more sensitive, when the count rates are low (Gratton et al. 2003).

1.5 Fluorescent protein pairs for FRET

Typically used pairs for FRET application are cyan/yellow and green/red pairs. Some fluorescent proteins have characteristics, which may limit their application, for example

ECFP has low brightness and photostability, EYFP is relatively poor expressed at 37 °C and is sensitive to the environment, RFPs often have slow maturation and so on (see section 1.2.1).

Large work is being done to discover and/or develop new version of the FPs, which would have improved properties. This work allows, for example, creating palettes of certain biosensors: Camuiα (section 1.3.2) may be used with such pairs as CFP / YFP (Erickson et al. 2011), mEGFP / mCherry, mEGFP / sREACh (Shibata et al. 2015), mClover3 / mRuby3 (Bajar, E. S. Wang, et al. 2016) and others.

Additionally, the specificities of the FRET detection methods set their limits on the choice of the FP pairs (Day & Davidson 2012). For example, for the FRET-FLIM approach a donor with a high quantum yield and single exponential lifetime decay is preferable for a simpler analysis and interpretation of the data. This makes the usage of traditionally popular cyan-yellow pairs with CFP or mCerulean donors problematic, because they have double exponential lifetimes (Tramier et al. 2006). However, the recently developed cyan variants mTurquoise2, mTFP1 and others have single exponential decays and are therefore promising donors for the YFP-derived acceptors (Mastop et al. 2017; Ai et al. 2006).

mEGFP (Tramier et al. 2006) and other GFPs (mClover variants, mNeonGreen etc.) are also very useful for the FRET-FLIM approach in pairs with RFPs, as they are bright and usually have single exponential lifetimes. Moreover, the spectral overlap of GFP / RFP-based pairs is typically slightly smaller, than for CFP / YFP-based pairs. This fact leads to a cleaner donor signal in case of FRET-FLIM and a better separation of the two channels in case of sensitized acceptor emission methods.

At the same time, approaches based on the sensitized acceptor emission measurement require both donor and acceptor fluorophores with a high quantum yield. This makes the cyan-yellow FP pairs the most popular candidates, because RFPs are typically less bright.

Usually acceptor crosstalk into the measured donor channel in FRET-FLIM is minor when appropriate emission filters are used, however it might become noticeable if the acceptor concentration is much higher than the donor concentration. Usage of a dim acceptor might be an advantage to avoid such problem. For this purpose several variants of YFP-deriving acceptors with high absorbance coefficient and extremely low quantum yield were developed, these types of proteins are called resonance energy-accepting chromoproteins, or REACHs (Ganesan et al. 2006; Murakoshi et al. 2008). Low acceptor emission doesn't only decrease the contamination of the donor signal due to the lower

acceptor crosstalk, but also allows using a filter with a wider donor spectral window, increasing the time resolution of the technique.

Additionally, the absence of fluorescence from REACh opens the opportunity of another probe in the yellow spectrum in order to detect the behavior of a different protein. For example, it creates an opportunity to use two biosensors at a time, what was done by (Laviv et al. 2016): dual expression of CamKII sensor Camuiα with a green / dark yellow pair mEGFP / dimVenus and RhoA sensor with red / far-red pair mCyRFP1 / mMaroon1 was used for the demonstration of this approach. Excitability of mCyRFP1 with cyan light allows simultaneous excitation of green mEGFP and red mCyRFP1 proteins, which lifetime signals can be easily separated with emission filters.

1.6 Aim of the study

FRET-based methods for PPI studies are a very useful for investigations in living cells on subcellular level. Despite a huge variety of fluorescent proteins developed so far, it is still challenging to find a suitable donor/acceptor pair. One has to balance between the limitations and advantages of certain characteristics of the FPs and the FRET estimation methods. This is not always an easy task, because the FPs and their pairs may perform with different success, depending on the techniques and analysis procedures applied, which makes their comparison across various papers especially difficult.

Two-photon-FLIM-FRET is a very useful approach with such advantages as high temporal and spatial resolution, independence from protein concentration and unintended photobleaching. A good FRET pair for this technique must have a high FRET efficiency, a bright donor well excitable by a two-photon laser and with a long monoexponential lifetime.

The first aim of this thesis is to express 9 cyan / yellow and 10 green / red FRET pairs of traditionally used and recently developed FPs under the same conditions in HEK293T cells and in primary neuronal cultures and to examine their FRET properties using the 2-photon TD FLIM technique. To achieve same conditions across pairs we will fuse donors with acceptors via a flexible relatively short linker. Comparison of a large number of proteins at a time with the same approach will more reliably allow choosing the pair with the best FRET properties for the FRET-FLIM application.

The second goal is to investigate the nature of high FRET performance for the best pairs in detail. For this purpose different model-based and model-independent analysis approaches will be applied. Additionally, experiments with the purified proteins will be

performed in order to deeper investigate concentration- and ratio-dependent characteristics of the FRET pairs.

Finally, we aim to verify the best FRET pair identified for *in vivo* application. We will fuse the FPs with a pair of presynaptic proteins Synaptophysin1 (Syph1) and Synaptobrevin2 (Syb2). Syph1 and Syb2 are presynaptic vesicular proteins, which take part in synaptic transmission. They are known to interact (Gordon & Cousin 2013), but still little is known about the role of their interaction, which makes them a potentially interesting object of research.

Taken together, this study will provide the first detailed comparison and analysis of multiple pairs of FPs with excellent individual properties, performed in primary neuronal cultures and as purified protein solutions using 2-photon FLIM approach.

2 Methods

2.1 Molecular biology

2.1.1 Design of molecular cloning strategy

Fluorescent protein pairs for testing the FRET performance were constructed following standard molecular biology techniques, including polymerase chain reaction (PCR) of the inserts, restriction of the backbone and the PCR fragment and their ligation.

Single donors were designed as FP-linker and pairs as FP_1-linker-FP_2, where FP_1 was usually a donor and FP_2 – an acceptor, except for mNeon-linker-mNeon and TagRFP-linker-mNeon. First, a flexible and relatively short linker SRG_4SG_4S, was cloned into the pAAV-CMV-MCS plasmid via XbaI/HindIII restriction sites. SR amino acids at the beginning of the linker were introduced due to cloning reasons, as they encode XbaI restriction site; in the end the linker had a STOP codon, flanked by BamHI and HindIII. The donor FPs were inserted 5' of the linker using EcoRI/XbaI restriction sites; afterwards, the acceptors were inserted 3' after the linker via BamHI/HindIII (excising the STOP codon). The exception to this strategy was AAV-TagRFP-linker-mNeon, where TagRFP was inserted via EcoRI/XbaI and mNeon via BamHI/HindIII. Plasmids, expressing single acceptors, were obtained by cloning of the donors via BamHI/HindIII into pAAV-CMV-MCS plasmid.

Fusion constructs for presynaptic studies were designed using in-fusion cloning strategy, based on the annealing and reconstitution of the complementary ends of the linearized backbone and PCR-amplified FP and protein of interest.

SnapGene Software was used to design the cloning strategies. The resulting constructs were verified by control restriction and subsequent sequencing in Eurofins Genomics (Ebersberg, Germany).

Sequences of linker oligonucleotides, cloning and sequencing primers are in Appendix section 6.8. Generated plasmids are listed in section 6.8.4. Plasmids used as the template for PCR of the genes of interest are in section 6.8.5, Synaptobrevin2 was amplified from mouse cDNA.

2.1.2 Polymerase chain reaction (PCR)

PCR was used to amplify genes of interest and use them further for cloning. The PCR mixture (Table 3) contained double-stranded DNA template, single stranded forward and

reverse primers (listed in section 6.8.1), desoxyribonucleotides (dNTPs), an appropriate buffer and a polymerase with proofreading activity (*Pfu* or *Phusion*).

Table 3. *PCR protocol*

Final concentration
1x *Pfu* Buffer with $MgSO_4$ or 1x HF Buffer
200 µM dNTP
0.5 µM forward primer
0.5 µM reverse primer
2 U *Pfu* or 1.6 U *Phusion* DNA polymerase
50-150 ng DNA
5% DMSO (optional)
dH_2O to a final volume of 50 µl

PCR was performed in a thermocycler with the following protocol (Table 4). Elongation time was adjusted for fragments individually depending on their length. If needed, annealing temperature was also adjusted according to the melting temperature T_m of the primers, in order to minimize amplification of unspecific fragments.

Amplified fragments were purified from agarose gels using Gel DNA recovery kit or NucleoSpin Gel and PCR Clean-up kit.

Table 4. *PCR programs for pfu and phusion DNA polymerases*

Step	Temperature	Time	Cycle
1. Denaturation	95 / 98 °C	5 / 1 min	1x
2. Denaturation	95 / 98 °C	30 / 10 s	35x
3. Annealing	55 °C	40 / 30 s	
4. Elongation	72 °C	1 kb per 2 min / 30 s	
5. Final elongation	72 °C	10 min	1x
6.	4 °C	∞	

2.1.3 DNA restriction

Purified PCR fragments (in case of standard cloning approach) and the backbone were digested (Table 5) with specific restriction enzymes (section 6.5) in an appropriate buffer for 3 h at 37 °C.

Table 5. *Restriction protocol*

Final concentration
1x Buffer
5 U restriction $enzyme_1$
5 U restriction $enzyme_2$
1-2 µg DNA
dH_2O to a final volume of 20 µl

The backbone was dephosphorylated by adding a shrimp alkaline phosphatase to the restriction reaction mixture for 15 min at 37 °C. The restricted DNA was purified either directly with DNA Clean and Concentration kit or NucleoSpin Gel and PCR Clean-up kit or it was purified from an agarose gel with Gel DNA recovery kit or NucleoSpin Gel and PCR Clean-up kit.

2.1.4 Ligation

In case of standard cloning restricted PCR fragment and restricted backbone were ligated in 3:1 molar ratio using T4 DNA ligase at room temperature overnight. Otherwise, amplified insert(s) and restricted backbone were ligated in 1:1 or 3:1 molar ratio with in-fusion enzyme at 50 °C for 20 min. The complete list of generated constructs is in section 6.8.4.

2.1.5 Chemical transformation of bacteria

The whole volume of the ligation reaction was used to transform 50-80 µl of competent bacteria (Stellar cells, in case of in-fusion cloning or *Escherichia coli* DH5α otherwise). Incubation on ice for 30-60 min was followed by a heat shock at 42 °C for 45-60 s and 2-3 min recovery on ice. Afterwards 200 µl of SOC Medium (for in-fusion cloning) or LB-medium (otherwise) was added to the mixture and incubated for 1 h at 37 °C on a thermoshaker. Finally, the bacteria were plated on agar plates containing 100 µg/ml ampicillin for selection of cells carrying the plasmid.

About 50-150 ng of plasmid was used for retransformation and subsequent amplification.

2.1.6 Plasmid amplification

After transformation of the ligated plasmids into bacteria, 6-8 colonies were picked from an agar plate and incubated in 5 ml LB-medium with 100 µg/ml ampicillin overnight. Next day, DNA was extracted with a Plasmid Miniprep kit.

For amplification of the plasmids in large amounts one colony of bacteria with retransformed DNA was incubated in 200-300 ml LB-medium with ampicillin. Purification was performed either using an EndoFree Plasmid Maxi kit in case of purified virus production or PureLink HiPure Plasmid Filter Maxiprep kit for plasmid amplification.

2.1.7 Oligonucleotide cloning

Oligonucleotides (section 6.8.3) were phosphorylated using T4 polynucleotide kinase and annealed by slow cooling from 95 °C to room temperature for ~ 1 h. Next, they were

purified using phenol-chloroform and precipitated in the presence of 3 M sodium acetate and 99% ethanol at -80 °C overnight. DNA was pelleted by centrifugation at 14000 rpm and 4 °C for 1 h, washed once with 70% ethanol and eluted in 10 µl of water. 1 µl of annealed oligonucleotides were used for ligation with restricted backbone.

2.1.8 Protein purification

Purified fluorescent proteins were provided by Dr. Sebastian Schmitt from the group of Prof. Dr. Matthias Geyer (Institute of Structural Biology, Biomedical Centre, University Clinic Bonn, University of Bonn). Proteins were cloned into a pET30a plasmid, expressed in *E. coli* Rosetta-2 (DE3) pLysS in 6 l of LB-medium overnight and purified using size exclusion chromatography on S200 columns in GE micro fast protein liquid chromatography (FPLC). All experiments were performed in Gefi buffer (20 mM HEPES, 150 mM NaCl, 1 mM TCEP, pH = 7.6).

2.1.9 Protein crystallization

Purified proteins (section 2.1.8) were crystallized by Dr. Kanchan Anand from the group of Prof. Dr. Matthias Geyer (Institute of Structural Biology, Biomedical Centre, University Clinic Bonn, University of Bonn). Crystals were grown on coverslips in drops of a buffer, containing 0.1 M HEPES, 18-20% Peg10K and 0.1-0.3 M NDSB, pH = 7.0-8.0 at 15 °C.

2.2 Cell culture

All cultures were maintained in humidified incubators supplied with 5% CO_2 at 37 °C.

2.2.1 HEK293T cells culture and transfection

Human embryonic kidney cells (HEK293T) were cultured in Dulbecco's modified Eagles medium (DMEM) with sodium pyruvate and supplemented with 10% fetal calf serum (FCS) and 1% antibiotics (100 units/ml penicillin and 100 µg/ml streptomycin); they were split every 2-3 days.

Coverslips were heated at 200 °C overnight; then they were coated with poly-D-lysine (0.1 mg/ml in borate solution) for at least 3 h at 37 °C and washed three times with dH_2O. For the experiments, HEK293T cells were plated on the coated coverslips in 24-well plates or on 35 mm µ-dishes. Next day, when HEK293T cells reached ~ 60% confluency, they were transfected with polyethylenimine (PEI). DNA was added to an appropriate volume (Table 6) of 150 mM NaCl, PEI was added to another volume of NaCl. Both solutions

were combined and mixed; the mixture was incubated for 20-30 min and added to the cells. The medium of the cells was replaced by a fresh one just before the transfection.

Table 6. Transfection mixture per 1 well or dish

	Coverslip in 24-well plate	35 mm µ-dish
Cell density at plating	50000 cells	80000 cells
DNA amount	0.3 µg	0.5 µg
1 µg/µl PEI	1.5 µl	1.8 µl
150 mM NaCl	30 µl x2	55 µl x2

2.2.2 rAAV production

Crude and purified viral extracts were prepared as described previously (Woitecki et al. 2016). HEK293T cells were plated in 100 x 20 mm dishes at a density 1.5 * 10^6 cells per dish. After 1-2 days, the cells reached an ideal confluency of around 60% and were transfected by calcium phosphate method. DMEM was changed to IMDM medium, supplemented with 5% FCS. A transfection mixture was prepared 4-6 h later (Table 7): DNA (AAV plasmid and helper plasmids) was added to the $CaCl_2$ solution in water, finally 2x HEBS (50 mM HEPES, 280 mM NaCl, 1.5 mM Na_2HPO_4, pH = 7.1) was added dropwise under vortexing. The mixture was incubated for 2 min and added to the cells in a circular motion. Next day, the medium was replaced with fresh DMEM (with FCS and Pen/Strep).

Cells were harvested 48-60 h after transfection using 1 ml medium, frozen and thawed 3 times and centrifuged. The supernatant was used as a crude viral extract, functional titers were determined by transduction of primary neuronal cultures.

Alternatively, harvested cells were lysed in the presence of 0.5% sodium deoxycholate and 50 U/ml benzonase endonuclease. The virus was purified with HiTrap heparin column and concentrated with Amicon Ultra Centrifugal filters.

Table 7. Transfection mixture per 100x20 mm dish

Component	Amount
dH_2O	1 ml
2.5 M $CaCl_2$	145 µl
Plasmid	5.5 µg
PFΔ6	11 µg
pNLrep	2.64 µg
pH21	2.64 µg
2x HEBS	1.2 ml

2.2.3 Primary neuronal cell culture and transduction

Primary mouse cortex neurons were prepared from E16-E19 wild type mice as described previously (Woitecki et al. 2016) and cultured in Eagle's Basal Medium (BME) or in Neurobasal Medium (NB+) on poly-D-lysine coated coverslips (section 2.2.1) in a 24-well plate or on 35 mm µ-dishes at a density of 50000 cells per well/dish.

Neurons were transduced with crude rAAV extracts on day *in vitro* (DIV) 3-7; experiments were performed on DIV 12-17.

2.2.4 Protein synthesis inhibition

To block protein synthesis HEK293T cells and primary neurons were treated with the protein synthesis inhibitor emetine at a final concentration 50 µM or with water of the same volume (as a control) and imaged on a confocal or 2-photon microscope 0, 1, 2, 3, 4.5 and 6 h after the treatment.

2.2.5 Immunocytochemistry (IC)

Primary neuronal cultures on coverslips were fixed in 4% paraformaldehyde (PFA) for 15 min on DIV 12-17 and washed 3 times with PBS. Next, they were incubated with 0.3% Triton-X100 (in PBS) for 10 min and in a blocking solution (1% BSA, 10% NGS, 1% Triton-X100 in PBS) for 1-2 h. Primary antibody in blocking solution was applied overnight at 4 °C and next day washed away with PBS 3 times. Afterwards, cells were incubated with a secondary antibody in blocking solution for 1-3 h at room temperature in darkness and washed 3 times in PBS. Finally, coverslips were mounted in Mowiol and imaged.

2.3 Viral injections and slice preparation

2.3.1 AAV injections into the brains of adult mice

All animal experiments were performed in accordance with the guidelines of the European Union and the University of Bonn Medical Centre Animal Care Committee. Male wt C57/BL6 mice were injected at the age of 7 weeks (> 20 g) into the CA1 hippocampal region as previously described (Woitecki et al. 2016). Animals were anesthetized with a mixture of 6 mg/kg xylazine and 90 – 120 mg/kg ketamine intraperitoneally. When mice were deep asleep, the heads were stabilized in a stereotactic frame and the skull was opened. At the coordinates 2 mm posterior and 1.5 mm lateral to bregma point a hole was drilled at each hemisphere with a small dental drill. A Hamilton syringe attached to a microinjection pump was slowly inserted into the brain through the

open skull at a depth of 1.5 mm. 1 µl of a purified rAAV virus was injected at 200 nl/min speed. The needle was kept for additional 5 min and slowly removed. The skin was closed by silk suture and the mice were warmed on a heating plate at 37 °C until they woke up.

2.3.2 Slice preparation

Animals were anesthetized with isoflurane 9-17 days after intracerebral injections. Mice were decapitated, the brain was rapidly removed and submerged into an ice-cold Ringer's solution (87 mM NaCl, 2.5 mM KCl, 1.25 mM NaH_2PO_4, 7 mM $MgCl_2$, 0.5 mM $CaCl_2$, 25 mM $NaHCO_3$, 25 mM Glucose, 75 mM Sucrose). Coronal 300-µm thick slices were prepared with a vibratome and placed into a fresh Ringer's solution at 35 °C for 30 min. Finally, they were transferred into ACSF (124 mM NaCl, 3 mM KCl, 1.25 mM NaH_2PO_4, 2 mM $MgCl_2$, 2 mM $CaCl_2$, 26 mM $NaHCO_3$, 10 mM Glucose) at room temperature and stored there for at least 30 min before the FLIM experiments. All solutions were gassed with 95% O_2 and 5%CO_2.

2.4 Fluorescence spectroscopy and microscopy

2.4.1 Emission and excitation spectra measurements

HEK293T cells were plated in 100 x 20 mm dishes at a density of 1.5 * 10^6 cells per dish. Upon reaching 60% confluency, they were transfected using PEI method (described in section 2.2.1, amounts of components are listed in table 8). Two days after transfection cells were washed with PBS and detached by application of trypsin for 2 min. Trypsinization was stopped by application of DMEM, containing 10% FBS. Then cells were centrifuged for 2 min at 1000 rpm and 4 °C and resuspended in 3 ml PBS.

Table 8. *Transfection mixture per one dish*

	100x20 mm dish
Cell density at plating	1.5*10^6 cells/dish
DNA amount	10 µg
1 µg/µl PEI	20 µl
150 mM NaCl	250 µl x2

Emission and excitation spectra were obtained using QuantaMaster400 spectrofluorometer with a xenon lamp as an excitation source. The excitation and emission parameters are listed in the table 9, light source parameters were chosen individually for each sample to avoid oversaturation. Final spectra were peak-normalized.

Table 9. *Ranges of wavelengths used for acquisition of excitation and emission spectra*

FP	Excitation spectra, nm		Emission spectra, nm	
	ExScan range	Emission	Excitation	EmScan range
mCerulean	310-480	505	430	450-610
mTurquoise2	320-480	505	430	450-610
mTFP1	340-500	520	440	460-620
mEGFP	350-530	550	450	470-640
mClover	370-530	540	460	480-640
mClover3	400-530	550	470	480-640
mNeon	370-530	550	450	470-640
mVenus	370-530	550	470	480-640
Venus(L68V)	370-530	550	460	480-640
YPet	370-530	550	470	490-640
mOrange2	440-580	590	520	540-700
TagRFP	440-590	600	530	550-700
mRuby3	440-600	620	520	540-700
mRuby2	440-600	620	520	540-700
mRFP	440-600	620	570	580-740
mCherry2	460-630	640	535	560-750

2.4.2 Confocal imaging and analysis

HEK293T cells and primary neurons were imaged using a laser scanning Nikon Eclipse A1/Ti confocal microscope. Fluorescence was collected with either CFI Plan APO 20x (NA 0.75) or CFI Plan APO IR 60x WI (NA 1.27) objectives. Cyan, green and red fluorescence was excited by imaging lasers with wavelengths 405 nm, 488 nm and 561 nm and collected using corresponding emission filters 482/35 nm, 525/50 nm and 595/50 nm.

Fiji (Schindelin et al. 2012) was used for the image analysis. Circular ROIs were used to manually mark the cell bodies or synapses, a mean grey value was evaluated and background intensity was subtracted. The resulting value was treated as mean fluorescence intensity (a.u.) and used to calculate acceptor-to-donor intensity ratio.

2.4.3 Acceptor photobleaching

HEK293T cells, expressing either mTurquoise2-linker-YPet or mNeon-linker-TagRFP for 24 h, were fixed with 4% PFA for 15 min, washed 3 times with PBS and mounted with TBS (138 mM NaCl, 2.8 mM KCl, 25 mM Tris, 0.1% Na Azide, pH = 7.4). The cells were imaged before and after bleaching using the Nikon Eclipse A1/Ti confocal microscope under CFI Plan APO IR 60x WI objective (NA 1.27). In order to bleach the acceptor in an area within a cell, the field of view was zoomed in 20-30 times and scanned in an acceptor channel until the intensity dropped by 80-95%. Afterwards, the cells were re-located at the

2-photon microscope system and FLIM was performed. Donor lifetime was compared between bleached and non-bleached areas of the same cell.

2.4.4 Fluorescence lifetime imaging microscopy (FLIM)

2-photon fluorescence lifetime imaging was performed using time-correlated single photon counting (TCSPC) at a Scientifica SliceScope 2-photon microscope system using a Ti:sapphire laser. Living HEK293T cells and primary neuronal cultures on coverslips were imaged in DMEM without Phenol Red, whereas fixed HEK293T cells in TBS, acute brain slices in ACSF gassed with 95% O_2 and 5% CO_2, purified proteins in Gefi buffer, protein crystals in mother liquor. Fluorescent proteins were excited with a laser set at 820 nm wavelength and 80 MHz frequency, 20x objective (NA 1.0) was used to collect the signal. At the specimen surface the laser intensity was ~5 mW.

Donor and acceptor steady-state fluorescence was collected using the emission filters listed in table 10, acceptor-to-donor intensity ratio was estimated using Fiji as described in section 2.4.2.

Green and cyan donor fluorescence for time-resolved lifetime measurements was filtered via appropriate filters listed in table 10. Photons were collected and correlated with the laser pulses using Simple-Tau SPC-150 TCSPC module and Spcm64 software. Images 512 x 512 pixel were acquired with a frame rate 1.48 Hz, photons were distributed in 256 time channels.

Table 10. *Parameters of emission filters in filter cubes used for two-photon imaging*

Filters within filter cubes	Steady-state fluorescence		Time-resolved fluorescence	
	green/red pair	cyan/yellow pair	green/red pair	cyan/yellow pair
$Filter_1$	525/50	472/30	525/50	470/22
Beamsplitter	565	514	560	488
$Filter_2$	620/60	550/49	605/70	

2.4.5 Instrument Response Function (IRF) acquisition

Instrument response function (IRF) was acquired by imaging urea crystals without filters in the single mode regime. The two-photon laser was set to 1080 nm. Measured IRF curves were superimposed to the lifetime curves.

2.4.6 Analysis of FLIM data: re-convolution

The raw FLIM images were imported into the SPCImage software. ROIs were drawn manually around cell bodies, synapses or other areas of interest. Decay curves with at least 10^4 photons were analyzed.

Standard analysis was performed in SPCImage Software by the least square iterative re-convolution. In this approach the theoretical exponential decay curve d_{0i} is convolved with the IRF and fitted to the measured curve d_i accompanied by the calculation of the reduced weighted sum of the residuals χ^2 (eq. 17) – this procedure is repeated multiple times, optimizing the fitting parameters, until χ^2 closest to 1 (corresponding to the best fit of the theoretical data with the measured one) is achieved; this procedure is repeated for all pixels of the image (O'Connor & Phillips 1984). SPCImage used an automatic IRF, which was almost identical to the measured one (section 2.4.5). The 12.5-ns inter-pulse interval was not long enough for the fluorescence intensity decay to return to the background level, that is why a built-in correction for an incomplete exponential fitting model was applied. A bin between 1 (3 x 3 pixels) and 3 (7 x 7 pixels) and a threshold between 10 and 20 (max bin height) were used to generate the FLIM images, depending on the signal strength. Scatter and shift were fixed, as well as the first and last time channels (*T1* and *T2*) used for re-convolution; offset was fit automatically, other parameters were left default.

$$\chi^2 = \frac{1}{n-p}\sum_{i=1}^{N}\frac{(d_i-d_{0i})^2}{d_i} \qquad \text{(Equation 17)}$$

Where $n - p$ is the number of degrees of freedom, $n = T_2 - T_1$ is the number of channels used in re-convolution, p is amount of fitting parameters (table 11).

Single and double exponential fitting models were applied by using 1 and 2 decay components respectively (eq. 2, $i = 1$ and 2).

$$F(t) = \sum_i a_i e^{-t/\tau_i} \qquad \text{(Equation 2)}$$

Final choice between fitting models was based on several parameters, such as: a good fitting model should fit the measured data nicely in all parts of the curve (rising phase, peak, decay); χ^2 (eq. 17) should be close to 1. When both models describe the measured curve equally good, then the simpler model (single exponential fit) was applied. When testing FPs and the FRET pairs we additionally applied an F-test, which aims to compare the significant difference between the χ^2 acquired from the two models. For this purpose the F-value was calculated according to the eq. 18.

$$F = \frac{(\chi_1^2-\chi_2^2)}{(p_2-p_1)} * \frac{(n-p_2)}{\chi_2^2} \qquad \text{(Equation 18)}$$

Here p_i is the number of fitting parameters in the respective models (table 11), n is the number of channels used in re-convolution, (p_2-p_1, n-p_2) are degrees of freedom.

The resulting F-value was compared to a critical value of the F-distribution (in this case it is ~3.00 for false-rejection probability 0.05): the simper (single exponential) model was accepted, when the F-value was not larger, than the critical value.

Table 11. *Fitting parameters for F-test*

Fitting model	# of fitting parameters	Fitting parameters
Single exponential	$p_1 = 3$	a, τ, c
Double exponential	$p_2 = 5$	a_1, τ_1, a_2, τ_2, c

In the experiments aiming the detection of presynaptic protein interactions, we applied the double exponential fitting model, as we expected the presence of the interacting and non-interacting fractions of molecules.

FRET efficiency was calculated from the equation 6; in case of a double exponential fitting model the amplitude-weighted averaged lifetime (eq. 19) was applied for FRET efficiency estimation.

$$E = 1 - \frac{\tau_{DA}}{\tau_D} \quad \text{(Equation 6)}$$

$$\tau_M = \frac{\sum_i \tau_i a_i}{\sum_i a_i} \quad \text{(Equation 19)}$$

2.4.7 Estimation of the acceptor crosstalk during the donor lifetime measurement

In order to estimate the impact of acceptor fluorescence in the donor signal, collected during FLIM, an acceptor crosstalk evaluation was performed.

Acceptors alone and donor-acceptor fusion pairs were expressed in HEK293T cells for one day, they were imaged using the 2-photon FLIM system: both FLIM and steady-state images were acquired simultaneously (filters used are listed in the table 10).

For each cell expressing acceptor alone we quantified the following parameter:

$$factor_A = \frac{photons_A^A}{I_A^A} \quad \text{(Equation 20)}$$

Where $photons^A{}_A$ is the number of detected photons in the FLIM image corrected to the pixel amount, $I^A{}_A$ is the background corrected acceptor fluorescence intensity estimated from the steady-state image. A mean value for the $factor_A$ was further used to quantify number of photons coming from the acceptor in a donor-acceptor fusion construct in individual cells:

$$photons_A^{DA} = factor_A I_A^{DA} \quad \text{(Equation 21)}$$

Where $I^{DA}{}_A$ is the acceptor fluorescence intensity in the fusion D-A construct estimated from the steady-state image. Finally, the acceptor crosstalk was evaluated as the contribution of the photons coming from the acceptor $photons^{DA}{}_A$ in a fusion construct to the total amount of photons detected in the FLIM image $photons^{DA}{}_{total}$:

$$crosstalk = \frac{photons_A^{DA}}{photons_{total}^{DA}} \quad \text{(Equation 22)}$$

All the acceptors expressed alone in HEK293T cells were checked under the 2-photon system and the highest crosstalk detected by the visual observation was in case of TagRFP. Acceptor crosstalk was estimated for mNeon-TagRFP and on average was 7.06 ± 0.55%. Acceptor crosstalk was also evaluated for mTurquoise2-YPet and was found to be in a range of 5.97 ± 0.19%. But the value obtained for mTurquoise2-YPet is overestimated, because it doesn't take into account the donor crosstalk into the acceptor steady-state image.

2.4.8 Correction for the acceptor crosstalk

When the purified proteins mNeon and mRFP were mixed and measured under the 2-photon FLIM system, the acceptor crosstalk into the donor channel became prominent at high acceptor concentrations. Acceptor crosstalk correction was applied in this experiment.

The fluorescence decay f_A of 300 µM mRFP solution was measured in a 2-photon FLIM system and used to quantify the mRFP crosstalk as described in section 2.4.7. Then the predicted mRFP crosstalk $f_{A,predicted}$ was calculated for every acceptor concentration used:

$$f_{A,predicted} = \frac{f_A photons_A^{DA}}{photons_A^A} \quad \text{(Equation 23)}$$

Finally the donor fluorescence decay traces of the D + A mixtures of purified proteins were corrected by the following procedure:

$$f_{corrected}^{D+A} = f_{measured}^{D+A} - f_{A,predicted} \quad \text{(Equation 24)}$$

Acceptor crosstalk corrected curves were used for the further analysis.

2.4.9 Analysis of FLIM data using a Phasor Plot

Phasor plots (Digman et al. 2008) are useful for quick, model-free visualization of lifetime data. Phase shift and modulation degree used in frequency domain FLIM can be directly applied to picture lifetimes in a polar plot. In case of data obtained by time domain FLIM a Fourier transform of the decay trace *I(t)* is needed first:

$$g(\omega) = \frac{\int_0^\infty I(t)\cos(\omega t)}{\int_0^\infty I(t)} \quad \text{(Equation 15)}$$

$$s(\omega) = \frac{\int_0^\infty I(t)\sin(\omega t)}{\int_0^\infty I(t)} \quad \text{(Equation 16)}$$

Where the laser repetition angular frequency ω is calculated as a product of the laser repetition rate and 2π.

Single-exponential lifetime decays land on the semicircle; the exact location depends on the lifetime. Multi-exponential decays fall inside the semicircle.

Phasor plots were built using SPCImage Software.

2.4.10 Imaging of crystals with a polarized light of changing electric field orientation

Steady-state imaging of crystals in mother liquor was performed using a Prairie Technologies Ultima Multiphoton System. The 2-photon Ti:Sapphire laser was set to 80 MHz repetition rate, the wavelength was tuned to 820 nm or 980 nm to collect mTurquoise2 or YPet signal respectively. Fluorescence was filtered with the 525/30 filter and collected by a 60x objective (NA 1.0). The Prairie View Version 5.4 was used to control the laser settings. A half-waveplate was used to modify the electric field orientation of the excitation light. At the initial time point the half-waveplate was set to 0° of the electric field polarization plane. Next, it was manually turned by 20° within 10 s until 180° range of orientation of the excitation light electric field was covered. The first and the last measurement points were repeated twice to make sure that the measurements stay stable. 0° of the electric filed orientation corresponds to polarization plane parallel to Y-axis of the steady-state image, 90° corresponds to X-axis of the image.

Crystal angle was calculated as the angle between Y-axis of the image and the crystal long axis using FIJI. Polarization angle φ was estimated as the angle between the electric field of the polarization light and the crystal long axis.

Fluorescence intensity of each crystal was measured in FIJI in a ROI within the crystal and background subtracted. The same ROI was used for one crystal across all polarization planes and laser wavelengths.

Since, according to the structure analysis, the proteins of the same type in mTurquoise2-YPet construct are present as two species with different orientations, the curves representing fluorescence intensity *f* dependence on the polarization angle φ are fitted using the following equation:

$$f(\varphi) = a * cos^4\big(0.01745 * (\varphi - \varphi_0)\big) + a * cos^4(0.01745 * (\varphi - \varphi_0 - \varphi_1))$$

(Equation 25)

Where *a* is amplitude, π/180 = 0.01745 is a degree-to-radian converter, φ_0 represents the projection angle between crystal long axis and one of the dipole orientation species, φ_1 is the projection angle between two dipole orientation species. Angles φ, φ_0 and φ_1 are given in degrees, these angles are on the projection of the crystal structure to the imaging plane.

2.5 Alternative methods of FRET efficiency estimation

2.5.1 "Simple" analysis

To check the influence of IRF, we applied a simplified analysis. After performing 2-photon FLIM fluorescence decay curves were obtained in SPCImage software by drawing ROIs around regions of interest and exporting them in asc format. Next, they were opened in Igor Pro software and an appropriate time scaling was applied. Cursors were placed in the beginning and the end of the decay part of the histogram (peak should be avoided, as it is convolved with the IRF), and the single or double exponential fitting model was applied to the curve between the cursors. In case of double exponential fitting an average lifetime τ_M was estimated from equation 19. Decision between single and double exponential fitting was made as described in section 2.4.6. FRET efficiency estimation was performed from the resulting lifetimes according to the formula 6.

2.5.2 Normalized total photon count (NTPC)-based analysis

For the decay curves with a photon count too low for a reliable fitting the following approach might be applied. Fluorescent decay curves were opened and scaled in Igor Pro (see section 2.5.1). Next, the normalized total photon count (NTPC) was estimated as the area under the peak normalized curve. FRET efficiency of the D-A FRET pair was evaluated as the ratio between the acceptor NTPC and the averaged donor NTPC:

$$E = 1 - \frac{NTPC_A}{NTPC_{D,av.}} \qquad \text{(Equation 26)}$$

2.5.3 Spectral fitting analysis

To provide a method for a quick FRET efficiency estimation we calculated theoretical emission spectra (modified from (Bajar, E. S. Wang, et al. 2016)):

$$f_{DA}(\lambda) = scale[Q_D(1-E)f_D(\lambda) + Q_A E f_A(\lambda)] + \frac{\varepsilon_A(\lambda_{ex})}{\varepsilon_D(\lambda_{ex})} f_A(\lambda) \qquad \text{(Equation 27)}$$

Where f_{DA} is the area normalized fluorescence of the tandem construct at wavelength λ, *scale* corrects for normalization, Q_D is the quantum yield of the donor, E is FRET efficiency, $f_D(\lambda)$ is the area normalized donor emission, Q_A is the quantum yield of the acceptor, $f_A(\lambda)$ is the area normalized acceptor emission, ε_A is the extinction coefficient of the acceptor at the excitation wavelength λ_{ex}, $\varepsilon_D(\lambda_{ex})$ is the extinction coefficient of the donor. FRET efficiency was determined as the value E, which gave the best fit between theoretical and measured emission spectra of the tandem constructs. Values for the quantum yields and extinction coefficients used for the fitting of mNeon-mRFP and mTurquoise2-YPet fusion constructs are listed in the table 12.

Table 12. *Parameters of FPs used for the spectral fitting of mNeon-mRFP and mTurquoise2-YPet*

Parameter	mNeon-mRFP	mTurq2-YPet
Q_D	0.80	0.93
Q_A	0.25	0.77
λ_{ex}, nm	480	435
$\varepsilon_D(\lambda_{ex})$, $M^{-1}cm^{-1}$	55 600	30 082
$\varepsilon_A(\lambda_{ex})$, $M^{-1}cm^{-1}$	3 200	2 137
$\varepsilon_D(\lambda_{ex}) / \varepsilon_A(\lambda_{ex})$	0.058	0.071

2.5.4 Model-free graphical analysis

Fluorescence decay curves, exported from SPCImage, were opened and scaled in Igor Pro (see section 2.5.1). Next, all the traces for a given construct were summed up and peak-normalized. Graphical analysis for the resulting curves was performed as described previously (Peulen et al. 2017). First, the FRET-induced fluorescence decay curve of the donor was divided by the decay curve of the donor in absence of the acceptor. Next, the decay phase of the resulting curve was fitted with a double exponential function (eq. 28), using a constraint for some fitting parameters (eq. 29).

$$F = y_0 + a_A e^{-(x-x_0)/\tau_A} + a_B e^{-(x-x_0)/\tau_B} \quad \text{(Equation 28)}$$

$$a_A + a_B + y_0 = 1 \quad \text{(Equation 29)}$$

Where y_0 is the fraction of the donor, which doesn't undergo FRET, a_A and a_B are the fractions (amplitudes) of two populations of the donor molecules, experiencing FRET with efficiencies E_A and E_B, calculated from lifetimes τ_A and τ_B, using equation 30.

$$E_{A/B} = \frac{\tau_D}{\tau_D + \tau_{A/B}} \quad \text{(Equation 30)}$$

2.6 Evaluation of dissociation constant K_D

To estimate the strength of measured and predicted interaction between the purified fluorescent proteins we quantified the dissociation constant K_D. FRET-induced donor decay curves were obtained for donor + acceptor mixtures with different acceptor concentrations; the subsequent graphical analysis was performed. Non-interacting y_0 donor fraction was plotted against acceptor concentration and fitted with the Hill function:

$$F = min + \frac{\max - min}{1 + (\frac{K_D}{y_0})^n} \quad \text{(Equation 31)}$$

Where max and min – are maximal and minimal values, which y_0 might potentially have – they are set at 1 and 0 respectively, which corresponds to 100% and 0% of non-FRET population. Parameter *n* reflects the stoichiometry of the D + A interaction, it resulted in values close to -1, therefore it was fixed at -1.

2.7 Prediction of the donor fluorescence decay curves for D + A mixtures

To predict donor fluorescence decay in mixture with acceptor for the case, when FRET happens as a result of occasional close localization of the FPs, we followed a previously described procedure (Lakowicz 2006). Characteristic acceptor concentration C_0 (molecules/cm^3) is the acceptor concentration, at which acceptor is statistically placed within R_0 (cm) from the donor:

$$C_0 = (\frac{4}{3}\pi R_0^3)^{-1} \quad \text{(Equation 32)}$$

Calculated C_0 for mTurquoise2 + YPet and mNeon + mRFP are given in the table 13.

Table 13. *Förster Radii R_0 and characteristic acceptor concentrations calculated for mTurquoise2 / YPet and mNeon / mRFP FRET pairs*

D + A pair	R_0, Å	C_0, molecules/cm^3	C_0, M
mTurq2 + YPet	59.36	$1.14*10^{18}$	$1.90*10^{21}$
mNeon + mRFP	55.01	$1.43*10^{18}$	$2.38*10^{21}$

Next, parameter γ was quantified by the following equation:

$$\gamma = \frac{\Gamma_{1/2}}{2}\frac{C}{C_0} \quad \text{(Equation 33)}$$

Where $\Gamma_{1/2} = \pi^{1/2} = 1.77$, C is the acceptor concentration.

Finally, the donor intensity decay for D + A mixtures can be predicted:

$$I_{DA}(t) = I_D^0 \exp\left[-\frac{t}{\tau_D} - 2\gamma(\frac{t}{\tau_D})^{1/2}\right] \quad \text{(Equation 34)}$$

Where I_D^0 is the normalized donor intensity at time point t = 0, I_D^0 equals 1 for peak normalized curves; τ_D is the lifetime of the donor-only, it equals 4.39 ns in case of mTurquoise2 and 3.41 ns for mNeon.

2.8 Statistics

Data is shown as mean ± SEM. Single factor ANOVA was applied to compare the mean of donor lifetime between the donor alone condition and a potentially interacting donor. Besides, single factor ANOVA was used to compare different analysis approaches with the standard one. Two-factor ANOVA was applied for the mNeon-TagRFP fusion pair to compare the red-to-green fluorescence intensity ratio, as well as the donor lifetime changes over time between the emetine treatment and the control in HEK293T cells and in primary neurons. All tests were carried out in StatPlus with a significance level set at α = 0.05.

3 Results

3.1 Fluorescent proteins and FRET pairs used in this work

Monitoring the Förster Resonance Energy Transfer (FRET) between the fluorescent proteins (FPs) genetically fused to the proteins of interest is a useful technique to study dynamic interactions between the latter in living cells. Choosing an appropriate FRET pair for the experiment is an important initial step in this technique.

So, the first aim of this work was to compare 20 pairs of traditionally used and recently developed FPs under the same conditions to identify the one with the best FRET properties. We tested both green (mNeon, mEGFP, mClover and mClover3) and cyan (mCerulean, mTurquoise2, mTFP1) donors. The first ones we combined with red acceptors, the latter – with yellow or orange acceptors. Physical and spectral characteristics of individual proteins (taken from literature) are listed in the introduction (table 2).

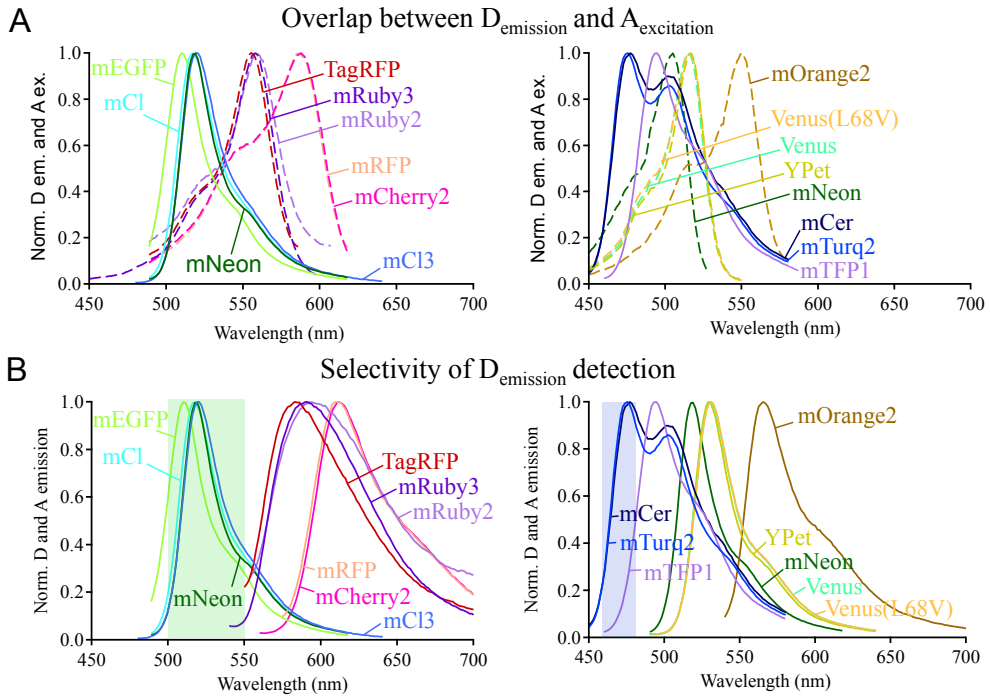

Figure 17. *Spectra of the fluorescent proteins used in this study to compose green-red (left) and cyan-yellow (right) FRET pairs. A – overlap between donor emission and acceptor excitation spectra makes FRET possible. B – donor emission is selectively collected by the two-photon system. Boxes mark the wavelength ranges of the emission filters used for FLIM: 500-550 nm for green donors and 459-481 nm for cyan donors. All spectra were acquired using a spectrofluorometer from suspensions of HEK293T cells, which had been expressing proteins for 24-48 h.*

We measured excitation and emission spectra of individual proteins in the suspension of HEK293T cells using QuantaMaster400 fluorometer in order to confirm the possibility of FRET between donors and acceptors (fig. 17).

Measured spectra may also be used to quantify Förster radius R_0, which is the distance between donor and acceptor, where 50% of the excited donor molecules are deactivated due to FRET (eq. 7). Estimated Förster Radii are listed in the introduction (table 1). All tested FP pairs had R_0 in the range between 50.3 Å (mEGFP / mRFP) and 64.6 Å (mNeon / mRuby3). The largest R_0 among cyan-yellow pairs was found to be around 61.3 Å for mTurquoise2 / mNeon) (table 1). Since FRET efficiency strongly depends on the proximity between the FPs (Introduction, eq. 5), mNeon / mRuby3 and mTurquoise2 / mNeon were expected to have the highest FRET efficiencies in their color groups.

3.2 HEK293T cells are not suitable for FRET estimation

To assess and compare different FRET efficiencies we followed previously applied strategies and fused pairs of FPs with the same short and flexible linker: donor-SR$(G_4S)_2$-acceptor.

Immortalized cell lines, for example HEK293 cells, are often used to investigate performance of FPs, as they grow fast and are easy to handle (Padilla-Parra et al. 2009; Koushik et al. 2006; Bajar, E. S. Wang, et al. 2016). We have also started with using HEK293T cells to express donor-acceptor fusion constructs.

First, we tested the expression of the fusion protein mNeon-TagRFP using the confocal laser scanning microscope (fig. 18, panels A-C). Proteins were homogeneously distributed in the whole cell body of HEK293T cells 24 h after transfection. Brightness varied between cells, due to different expression levels across the cultured cells. Moreover, the red-to-green intensity ratio between cells within the same culture varied as well (fig. 18, panel D), which was unexpected, because mNeon and TagRFP were produced as a fusion construct, hence their expression ratio was always 1:1.

In order to test, whether this variability might be a problem for FRET-based studies, we expressed mNeon-TagRFP in HEK293T cells for 24 h and imaged them using a 2-photon TCSPC system, which allowed us to quantify both red-to-green fluorescence intensity ratio and mNeon lifetime in each cell.

When expressed alone, mNeon had a single lifetime component of approximately 3.05 ± 0.01 ns. In presence of a FRET acceptor, the donor lifetime got reduced and became double exponential (with the lifetime components τ_1 and τ_2, ns), contributing with

amplitudes a_1 and a_2 (%) respectively. Next, an amplitude weighted average lifetime τ_M (ns) was evaluated according to the equation 19.

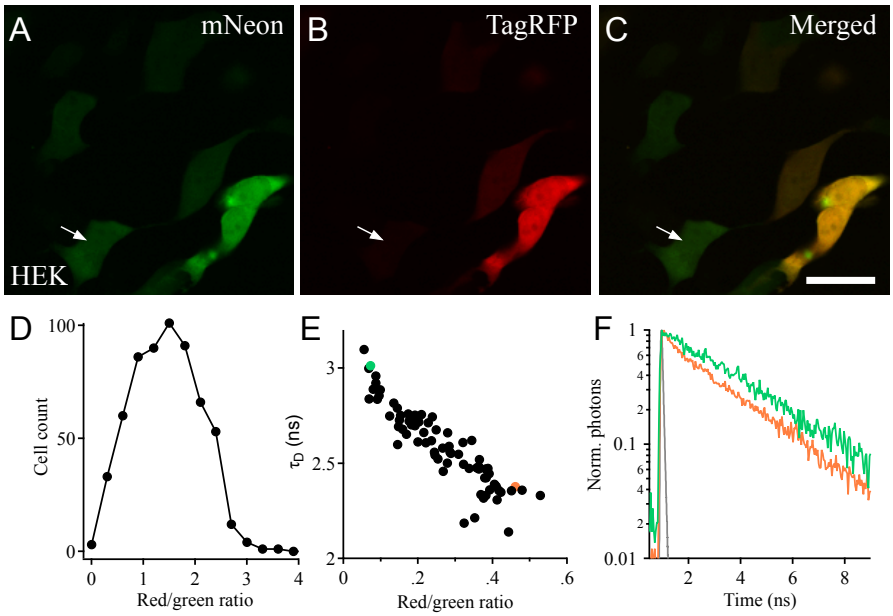

Figure 18. *Variability of a red-to-green fluorescence intensity ratio in a population of HEK293T cells after 24 h expression of the fusion mNeon-TagRFP protein, demonstrated by confocal images of the cells (A-C) and their quantification (D), scale bar 30 µm. E, F – correlation of the R/G ratio with the lifetime of mNeon, points represent individual cells, imaged with a 2-photon TCSPC system. Cells with a small R/G ratio and slow donor lifetime (example given in green) have a slower decay, than cells with a large R/G ratio and a fast donor lifetime (red curve). Here and on all the following figures measured Instrument Response Function is represented on histograms.*

Finally, the calculated average lifetime was plotted against the red-to-green intensity ratio (fig. 18, panel E). This experiment showed a correlation between the color of the cell and the lifetime of the donor molecules: "greenish" cells with a lower red-to-green fluorescence intensity ratio had a longer average lifetime due to less FRET, for some cells it was almost indistinguishable from the lifetime values of mNeon expressed alone. In contrast, cells with high red-to-green ratio exhibited faster donor lifetime. This effect was also seen as a difference in decay curves of two exemplar HEK293T cells with low and high red-to-green ratio (fig. 18, panel F).

A possible explanation for such variability between the cells could be a difference in maturation times between the proteins. Namely, red FPs always need much more time to mature, than green proteins. This might lead to the presence of a population of molecules, consisting of a mature, hence fluorescing, donor and not mature acceptor, which therefore cannot accept energy. Such situation may result in a weaker apparent FRET efficiency, when averaging the cell population.

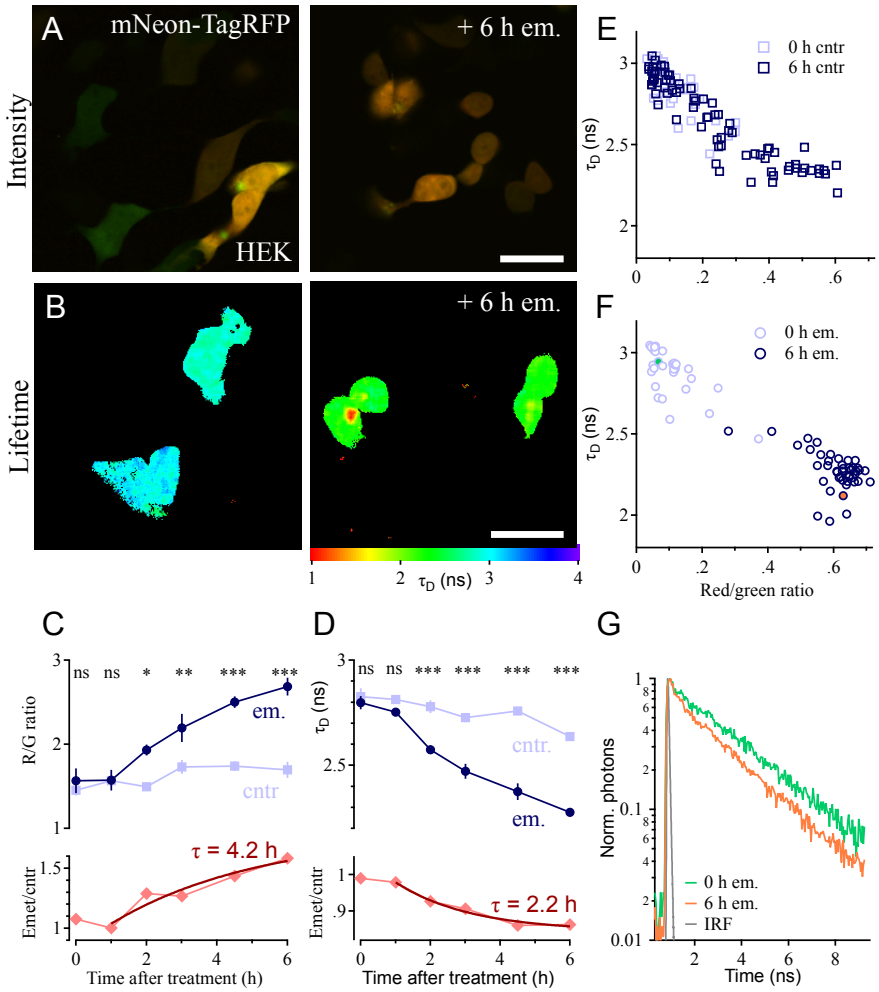

Figure 19. *Monitoring fluorescent protein maturation upon protein synthesis inhibition. Representative merged red-green (A) and lifetime (B) images of the HEK293T cells expressing mNeon-TagRFP fusion construct for 24 h (A) or 12 h (B) before (left) and after (right) treatment with 50 µM protein and RNA synthesis inhibitor emetine. Red-green images were acquired using a confocal microscope, scale bar 30 µm; lifetime images were acquired using a 2-photon microscope, scale bar 30 µm, color-coded scale bar represents the average donor lifetime: 1.0 – 4.0 ns. Evaluation of the experimental results showed increase of the red-to-green intensity ratio (C) and decrease of the average donor lifetime (D) in individual cells in comparison to the control (treatment with water of the same volume). Data is presented as mean ± SEM. Two factor ANOVA was performed to verify the differences between the treated and control cells per time point: statistical significance is shown by (*) at 5% level of significance, (**) at 1%, (***) at 0.1%. Division of the emetine-treated curve by the control gives an estimate of the exponential maturation with the lifetime in the range between 2.2 h (calculated from the donor lifetime decrease) and 4.2 h (calculated from the red-to-green ratio increase). E, F – individual cells demonstrate decrease of the lifetime and red-to-green ratio variability upon the emetine treatment after 12 h of transfection. G – representative donor lifetime decay traces of individual cells (marked in panel F) before (green) and after (red) the treatment.*

In order to test this hypothesis, we treated HEK293T cells, expressing mNeon-TagRFP for 24 h, with 50 µM emetine (or with water of the same volume as a control) for 6 h

(fig. 19). This chemical inhibited RNA and protein synthesis; therefore, we could monitor the maturation of the previously synthesized FPs and explore the influence of the maturation on FRET. Confocal imaging of the cultured cells and its quantification demonstrated the gradual increase of the red-to-green fluorescence intensity ratio over the 6 h time period, indicating the maturation of the FP molecules, which were already generated before emetine application (fig. 19, panels A, C). We also monitored the cells with the 2-photon TCSPC system 12 h after the transfection to investigate the changes in the donor lifetime. So, along with the protein maturation, the average lifetime of mNeon was decreasing over the observed time (fig. 19, panels B, D), proving, that not mature acceptor cannot perform FRET. Two-factor ANOVA statistical test showed, that over time changes in both red-to-green ratio ($p < 0.01$) and donor lifetime ($p < 0.001$) upon the emetine treatment were statistically significant.

Emetine treatment reduced the cell-to-cell variability within the population and shifted the average donor lifetimes to shorter values and red-to-green fluorescence intensity ratios to larger numbers for the whole population (fig. 19, panels E-G).

Our data suggests, that fast growing and reproducing cells like HEK293T have a mixed population of fully and not fully mature FPs due to a strong protein overexpression, hence FRET would be systematically underestimated in such conditions – and to different extent for different acceptor proteins (depending on their maturation time), making such cells not very suitable for FRET-based applications, including comparison between different FRET pairs.

3.3 Comparison of FRET pairs in neurons

3.3.1 Primary neuronal cultures are suitable for FRET efficiency estimation

Other cell types, which do not overproduce proteins to the same extent as HEK293T cells, should be more reliable for experiments, involving FRET. A good candidate might be cultured primary neurons, as they are already differentiated, therefore they do not divide and produce fewer proteins.

To test this, we prepared rAAV1/2 crude viral extract to transduce primary cortical neurons at day *in vitro* (DIV) 4. We investigated the expression of mNeon-TagRFP 11-13 days after transduction by applying 50 µM emetine for 6 h and monitoring the fluorescence using the confocal microscope (fig. 20, panels A-C). Proteins were homogeneously expressed throughout the cells, and there was no significant change (two-way ANOVA, $p > 0.05$) in red-to-green intensity ratio upon emetine treatment in

comparison to the control condition, indicating, that after such a long expression time the majority of the protein molecules in cultured neurons were already fully mature, and the fraction of not matured proteins should not affect the FRET quantification. Indeed, two-photon FLIM of the neuronal cultures expressing mNeon-TagRFP (fig. 20, panels D-E) showed, that donor lifetimes didn't vary between the cells, and were in the same range as for the HEK293T cells, treated with emetine for 6 h.

So, we decided to use primary cortical neurons for the further experiments in cultures.

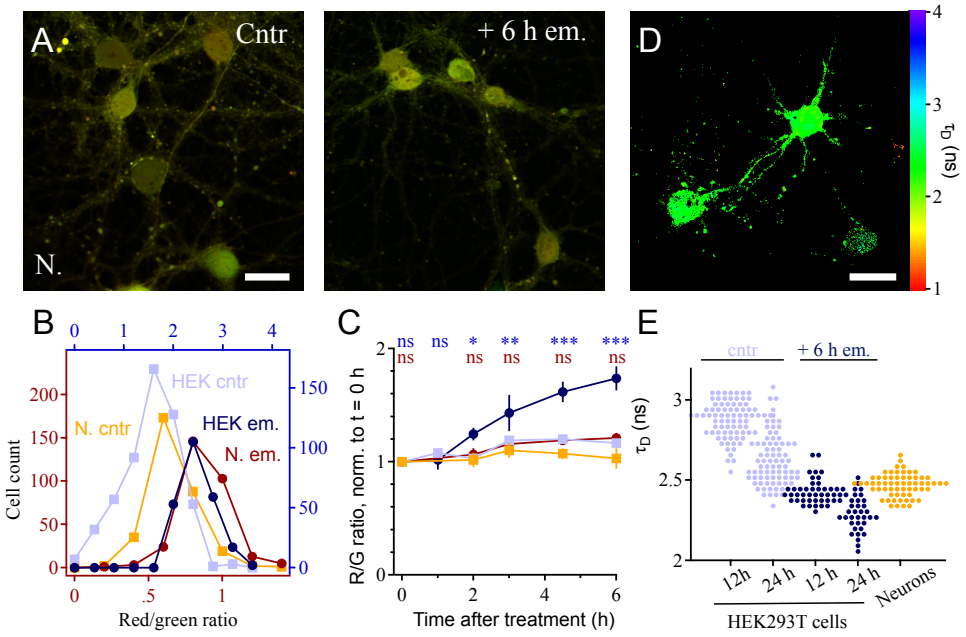

Figure 20. *Neurons, transduced on DIV 4 with crude rAAV1/2 extracts have most of the FPs fully mature by DIV 11-13. A – representative merged red-green confocal images of the primary mouse cortex neurons expressing mNeon-TagRFP don't show a difference between treatment with 50 µM emetine (right) and the water control (left). Scale bar: 30 µm. B – variability of the red-to-green fluorescence intensity ratio in individual neurons is less, than in HEK293T cells 24 h post-transfection. Absolute values are different for the two cell types due to different laser settings applied; they were aligned in the peak of the emetine-treated curves. C – average red-to-green ratio in neurons stays stable over 6 h of emetine treatment, unlike HEK293T cells. Curves were normalized to the values at 0 h time point and shown as mean ± SEM; two factor ANOVA was applied to compare treatment and control conditions per time point for HEK293T cells (blue) and primary neurons (red). D – representative 2-photon-FLIM image of primary mouse cortex neurons, expressing mNeon-TagRFP. Scale bar 30 µm, color-coded scale bar: 1.0 – 4.0 ns. E – lifetimes and their variability in individual HEK293T cells (for both 12 and 24 h post-transfection) decreases after 6 h of emetine treatment. Untreated neurons demonstrate properties similar to emetine-treated HEK293T cells.*

3.3.2 Two-photon-FLIM of FRET pairs expressed in primary neurons

Donors alone and 20 donor-acceptor pairs with a short and flexible linker SRG_4SG_4S in-between were expressed in primary mouse cortex cultures. Neurons were transduced with rAAV1/2 crude viral extracts on DIV 0-7 and imaged at least 7 days later on

DIV 13-17 using a two-photon TSCPC setup. Donor lifetimes were estimated in presence and absence of the fused acceptors to find the pair with the best FRET properties.

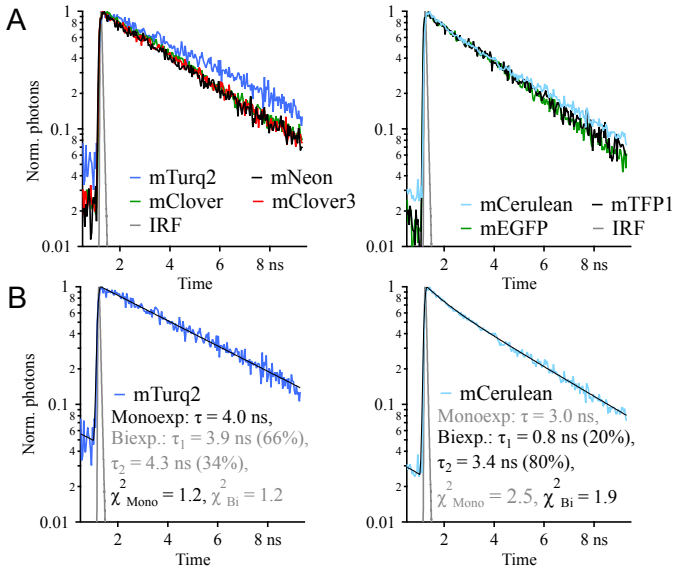

Figure 21. *Representative peak-normalized fluorescence decay curves used for lifetime estimation. A – lifetime curves of FRET donors used in this work acquired by two-photon-FLIM from individual cells in primary neuronal cultures. B – examples of the fitting (black curves): single exponential fitting for mTurquoise2 and double exponential fitting for mCerulean.*

When expressed alone, the fluorescence lifetime of most donors was well described by single exponential re-convolution fitting (more details in Methods section 2.4.6) with no significant improvement by addition of a second lifetime component (table 14, fig. 21). mTurquoise2 displayed the longest lifetime among tested donors. mCerulean had a double exponential lifetime, which made it the least preferable donor. Amplitude weighted average lifetime τ_M was calculated for mCerulean according to the equation 19.

Table 14. *Lifetimes of the donors expressed alone. Most of the proteins had monoexponential lifetimes, except for mCerulean with a double exponential lifetime.*

Donor protein	τ or τ_M (ns)	τ_1, ns (a_1, %)	τ_2, ns (a_2, %)	# cells
mNeon	3.04 ± 0.01			141
mEGFP	2.76 ± 0.02			87
mClover	3.17 ± 0.02			81
mClover3	3.17 ± 0.01			127
mCerulean	2.90 ± 0.02	1.38 ± 0.06 (31.3 ± 1.5)	3.57 ± 0.05 (68.7 ± 1.5)	124
mTurquoise2	4.16 ± 0.01			61
mTFP1	2.88 ± 0.01			57

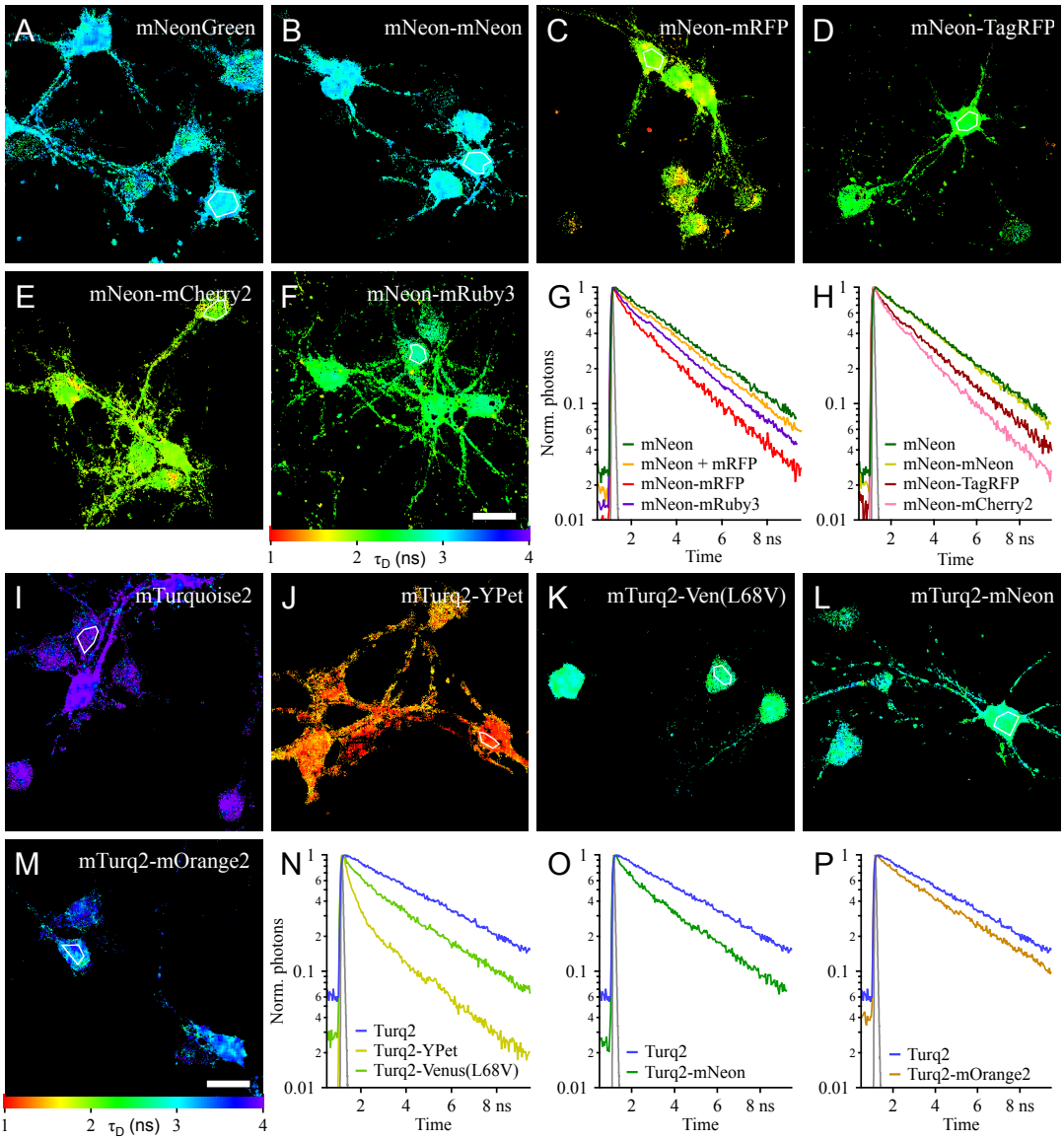

Figure 22. *Representative FLIM images (A-F, I-M) and fluorescent decay curves (G-H, N-P) for mNeon (A-H) and mTurq2 (I-P) donors acquired using a two-photon-FLIM system. Fusion constructs and the controls were expressed for at least 7 days in primary mouse cortex neurons and imaged on DIV 13-17. Amplitude weighted donor lifetime is color-coded in the FLIM images: scale bar 1.0-4.0 ns; distance scale bar 30 µm. ROIs mark approximate area used to obtain the fluorescence decay curves used for lifetime evaluation. Decay curves on the graphs demonstrate averaged curves from all the cells on the corresponding FLIM images. In presence of the fused acceptor donor lifetime decreases: it is seen by the change of the color in the FLIM images and by a faster decay on the graphs. Co-expression of the FPs doesn't result in FRET (G: mNeon+mRFP). Fusion of a different protein by itself doesn't affect the lifetime curve (B, H: mNeon-mNeon).*

Green donors were fused to mRFP, TagRFP, mCherry2, mRuby2 or mRuby3, cyan donors were fused to YPet, Venus, Venus(L68V), mNeon or mOrange2. Lifetime reduction of the donor upon fusion to the acceptor was clearly seen both on FLIM images

and by comparison of the decay curves in presence and absence of the acceptor. Representative images and lifetime curves for the green donor mNeon and the cyan donor mTurquoise2 are illustrated in fig. 22. Measurement of the mNeon-mNeon construct didn't show any lifetime reduction, indicating that the fusion itself of a different protein didn't affect the fluorescence decay (fig. 22, panel H).

As an additional control, we estimated the crosstalk of the acceptors to avoid unspecificity of the lifetime imaging filters (section 2.4.7). The largest crosstalk was for TagRFP – on average less than 7% of photons in the donor channel potentially derived from the acceptor.

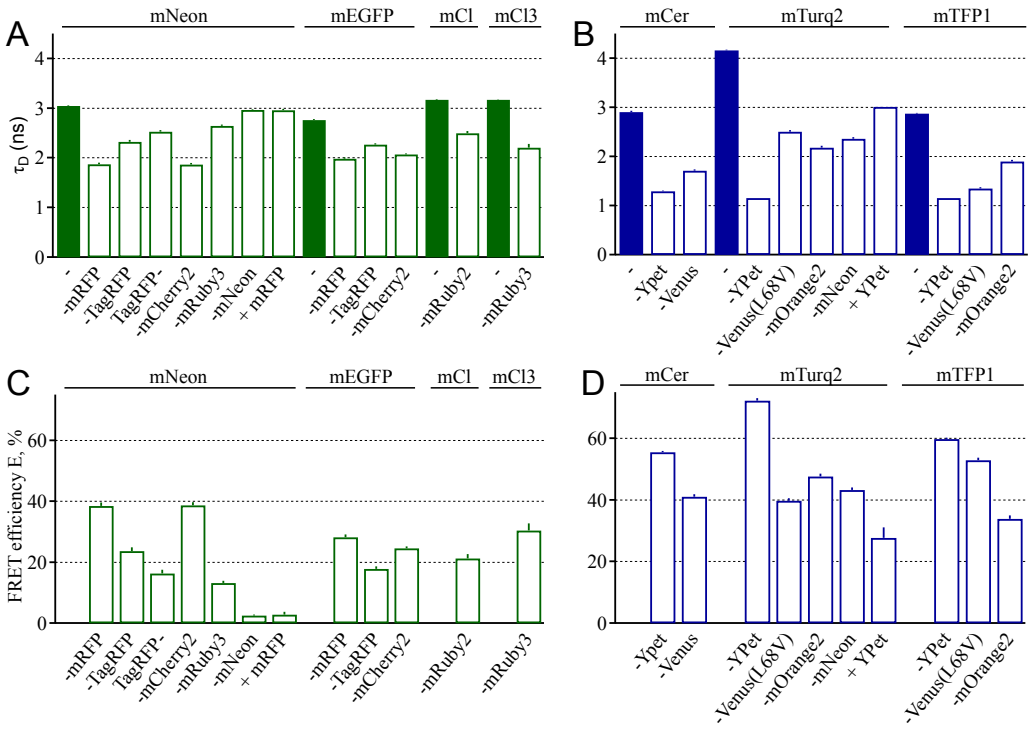

Figure 23. *Average donor lifetimes (A, B) and FRET efficiencies (C, D) for all the tested green / red (A, C) and cyan / yellow (B, D) pairs of fluorescent proteins. Highest FRET efficiency was demonstrated by mNeon-mRFP and mNeon-mCherry2 green / red pairs and mTurq2-YPet cyan / yellow pair. Control mNeon-mNeon showed, that the fusion of a different protein itself has a minimal effect on the lifetime. Order of the proteins doesn't play a big role, as seen in case of mNeon / TagRFP pair. Co-expression of mNeon and mRFP doesn't lead to FRET due to large distance between the unbound FPs, which is not the case for mTurq2 and YPet co-expression. Single factor ANOVA was performed to compare donor lifetimes in presence and absence of the acceptor and showed a high significance value (1% or less) for all the conditions.*

In presence of the acceptor the shortened donor lifetime decay curves were best described by a double exponential fitting function. In order to compare the FRET pairs between each other, we evaluated the amplitude weighted average donor lifetimes of the

fusion constructs (eq. 19 and fig. 23, panels A-B) and used obtained values to calculate the FRET efficiencies of the pairs (eq. 6).

The resulted estimations fell into three groups: low (~ 20%), medium (~ 30-40%) and high (~ 50-60%) FRET efficiencies (fig. 23, panels C-D). First group included mNeon / TagRFP, mNeon / mRuby3, mEGFP / TagRFP, mEGFP / mCherry2 and mClover / mRuby2 pairs. Constructs mEGFP-mRFP, mClover3-mRuby3, mNeon-mRFP, mNeon-mCherry2 were in the second group, as well as cyan-yellow pairs with Venus, mOrange2 and mNeon acceptors and mTurq2-Venus(L68V). The third group with high FRET-E included only cyan-yellow FRET pairs with YPet acceptor and mTFP1-Venus(L68V). The highest FRET efficiency among all the tested tandem constructs was demonstrated by mTurq2-YPet pair and equaled 72.3%.

Comparison of mNeon-TagRFP and TagRFP-mNeon showed that the order of fusion didn't affect FRET-E much (fig. 23, panels A, C).

Co-expression of mNeon and mRFP resulted only in a minor lifetime change of the donor (fig. 23, panels A, C), because freely floating FP molecules were too far away from each other to perform FRET. However, mTurq2 and YPet, when expressed together, showed certain level of the donor lifetime reduction (fig. 23, panels B, D). The reason might be a slight interaction between the FPs due to "sticky" amino acids of YPet, as previously described (Bajar, E. Wang, et al. 2016).

If the slow lifetime component of the double constructs almost equals the donor-alone lifetime, then it can be interpreted as a non-FRET fraction of the donor. For the following constructs the difference between the slow component τ_2 and the donor-only lifetime τ_D was less than 15%: (green-red) mNeon-mRFP, mNeon-TagRFP, mNeon-mRuby3, mEGFP-mRFP, mEGFP-TagRFP, mEGFP-mCherry2, mClover-mRuby2, mClover3-mRuby3, (cyan-yellow) mTurquoise2-mOrange2, mTFP1-mOrange2. In this situation the slow, unquenched lifetime component τ_2 could be fixed at the τ_D value. The fast component τ_1 illustrated the fraction of the interacting donor (marked with "X" in the fig. 24) and was used for the FRET efficiency estimation (eq. 6). Amplitude a_1 (eq. 2) could be then directly interpreted as a fraction of interacting donor molecules.

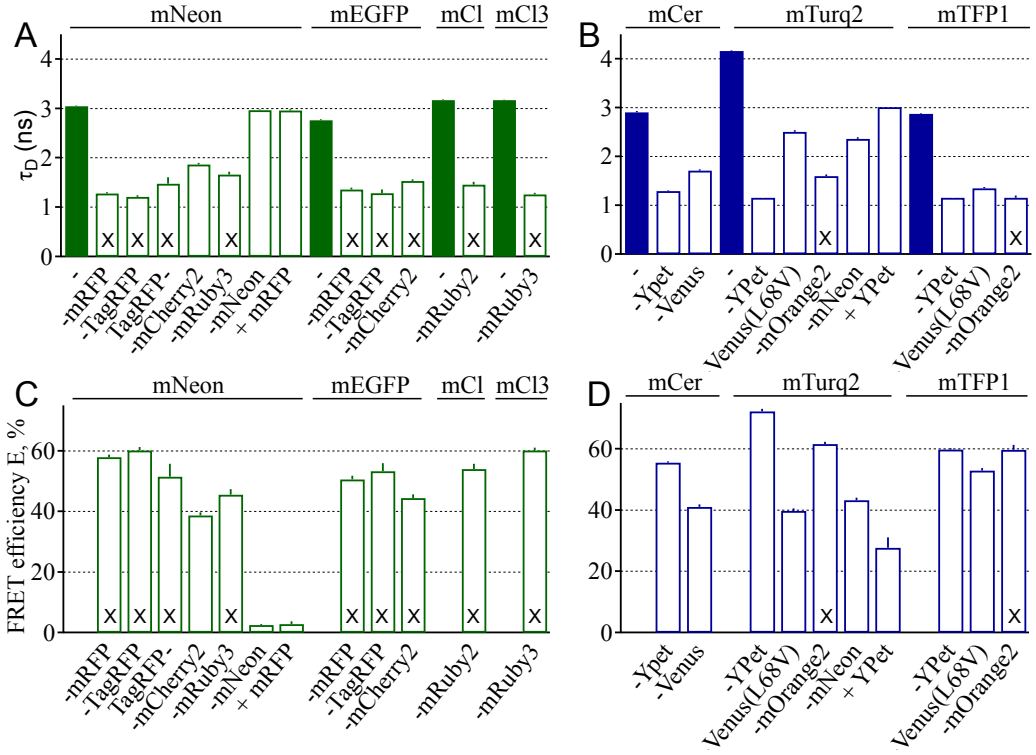

Figure 24. *Donor lifetimes (A, B) and the FRET efficiencies (C, D) for all the tested green/red (A, C) and cyan/yellow (B, D) pairs of fluorescent proteins. Highest FRET efficiency was demonstrated by mNeon-mRFP and mNeon-TagRFP green/red pair and mTurq2-YPet cyan/yellow pair. In case of the fusion constructs marked with "X" fast lifetime component $\tau_1 \pm$ SEM was used for the FRET efficiency calculation and is shown in panels A-B, for the rest of the donor-acceptor fused pairs the average $\tau_M \pm$ SEM was applied.*

3.3.3 Acceptor photobleaching recovers the donor-alone lifetime

To further prove that the donor lifetime reduction upon fusion to the acceptor occured due to FRET we performed acceptor photobleaching. Photobleaching achieved by application of a strong laser illumination physically damages the FP and irreversibly inactivates its ability to accept and emit photons, thereby the bleached acceptor would stay bound to the donor, but FRET would become impossible.

Table 15. *The influence of mounting medium on the fluorescence lifetime. *This study, FPs are expressed in HEK293T cells (mNeon) or in primary neurons (mTurq2), their lifetimes are measured using a 2-photon FLIM system; **Lifetime of FPs expressed in HeLa cells from (Joosen et al. 2014).*

Protein	Media	τ ± SD (ns)*	τ ± SD (ns)**
mNeon	Living cells	2.96 ± 0.01	
	TBS	2.65 ± 0.01	
mTurquoise2	Living cells	4.16 ± 0.04	4.08 ± 0.03
	TBS	4.13 ± 0.34	4.12 ± 0.03

For the sake of speed and simplicity of the experiment we expressed mNeon-TagRFP and mTurq2-YPet in HEK293T cells for 24 h and fixed them with 4% PFA to immobilize

the proteins and avoid their transport and diffusion. We mounted the samples in TBS, because it displayed minimal effect on the lifetime (table 15), as reported previously (Joosen et al. 2014). Indeed, mTurq2 mounted in TBS showed no significant changes (single factor ANOVA, $p > 0.05$) in comparison to mTurq2 in live cells. However, mNeon displayed a shorter double exponential lifetime when fixed, significantly different (single factor ANOVA, $p < 0.001$) from mNeon in live HEK293T cells.

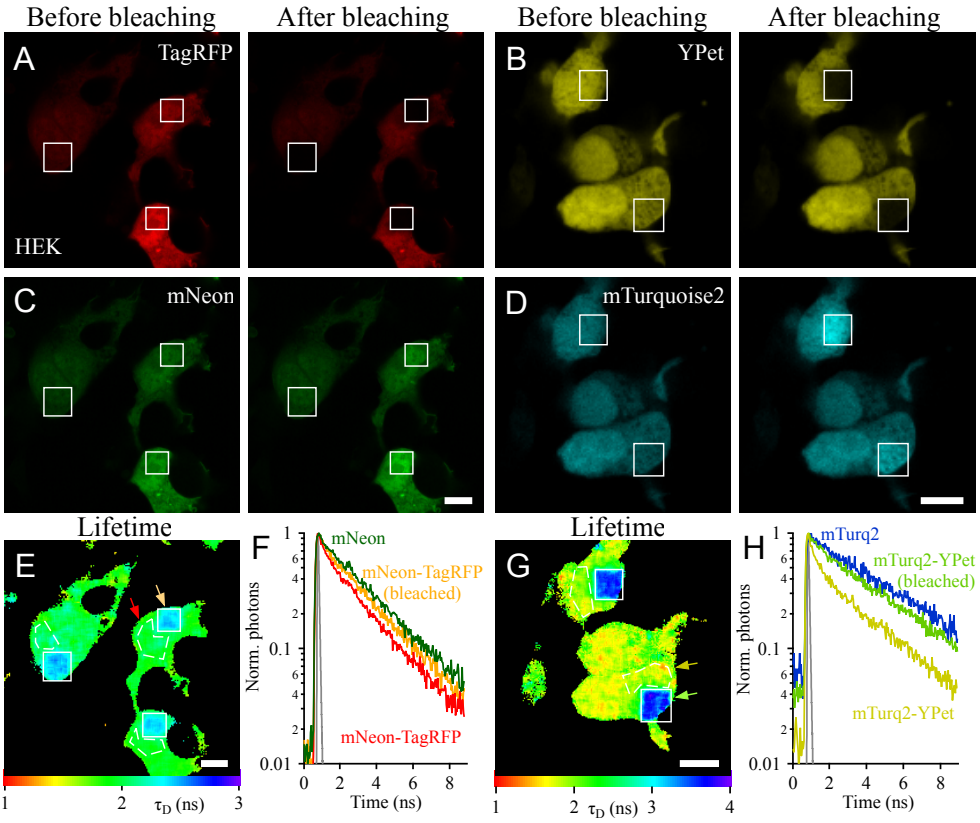

Figure 25. *Acceptor photobleaching recovers the donor lifetime and increases the donor fluorescence. HEK293T cell expressing mNeon-TagRFP (A, C, E-F) or mTurq2-YPet (B, D, G-H) for 24 h, were fixed and mounted in TBS. Acceptor was bleached in a square area within a cell using a confocal microscope (A-D), donor's fluorescence intensity got increased in this area upon bleaching. Same cells were relocated under a two-photon FLIM system and imaged (E, G). Scale bar: 10 µm. F, H – representative lifetime traces of donor expressed alone, unbleached and bleached areas of the same cell (marked with respective colors in E, G) expressing donor-acceptor construct. After bleaching the curves approach the donor alone condition.*

We used a confocal microscope in order to achieve selective photobleaching of the acceptor, which is not possible with a two-photon set up. We performed the bleaching of an area inside a fixed HEK293T cell (fig. 25, panels A-D) in order to compare the FP pair in identical conditions. The donor's fluorescence increased drastically in the bleached area, namely 1.28 ± 0.02 times in case of mNeon-TagRFP and 2.04 ± 0.04 times in case of

mTurq2-YPet. This was an indication, that the donor could not transfer its energy by FRET anymore, so its fluorescence emission got increased.

Next, we relocated the bleached cells under the two-photon-FLIM system and imaged them (fig. 25, panels E, G). Fluorescence decay curves were clearly different for bleached and unbleached areas (fig. 25, panels F, H): when bleached they approached the curves obtained from donors expressed alone. Quantification confirmed this trend (fig. 26): lifetimes of mNeon-TagRFP and mTurq2-YPet in the bleached areas almost reached the lifetimes of mNeon and mTurq2 respectively. Moreover, bleached mTurq2-YPet demonstrated single exponential decay, which was observed for mTurq2. Although mNeon-TagRFP didn't become monoexponential when bleached, it actually followed the trend of donor-alone as well, because fixed mNeon (unlike in living cells) was fitted better using a double exponential model and had a shorter lifetime. Taken together, these data strongly suggests that the donor lifetime reduction observed in the pairs of fused FPs (chapter 3.3.2) is due to FRET.

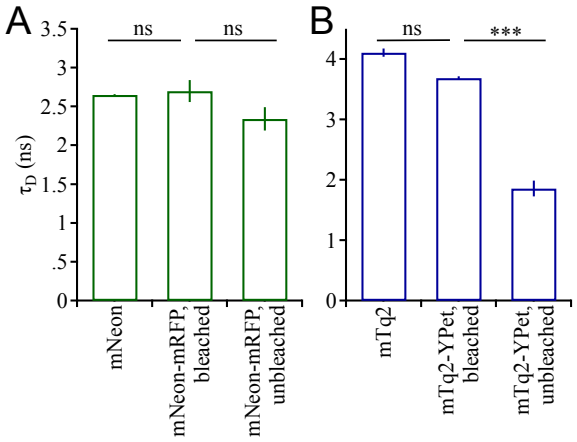

Figure 26. *Donor lifetime in acceptor photobleached regions approached the values of donors alone. Lifetime decays of mTq2 and mTq2-YPet in the bleached region were fit with the single exponential function; lifetime curves of mNeon, mNeon-mRFP in bleached and unbleached regions and mTq2-YPet in the unbleached region were best fit with a double exponential model, and the average lifetime τ_M was estimated. Single factor ANOVA was applied to test for statistical significance (*** corresponds to p-value < 0.1%). Data derives from 19-46 cells from 3-5 experiments.*

3.4 Other FRET estimation methods: simplified and/or model-free

All fluorescence decay traces in this work were analyzed by re-convolution in SPCImage software, which had been developed together with the FLIM setup by Becker&Hickl. This approach involved application of a decay model – single and double exponential models were compared for each measurement (Methods section 2.4.6). In

addition, incomplete decay model was used in the analysis, as the 12.5 ns-long inter-pulse interval typical for two-photon lasers didn't allow the fluorescence to reach the background level before the new laser pulse starts. Finally, the software corrected for the Instrument Response Function, which was convolved with the actual fluorescence decay.

Although there are softwares (including SPCImage), which automatize these calculations, it is not always possible or desirable to use them. That is why we wanted to test if there are other methods to analyze decay traces, which would give reasonable results; or even if there are methods, which would provide additional information about FRET.

3.4.1 "Simple" analysis

One such approach allowing a fast estimation of the donor lifetime could be a "simple" fitting – single or double exponential fitting of the decay part of the fluorescence decay curve (fig. 27).

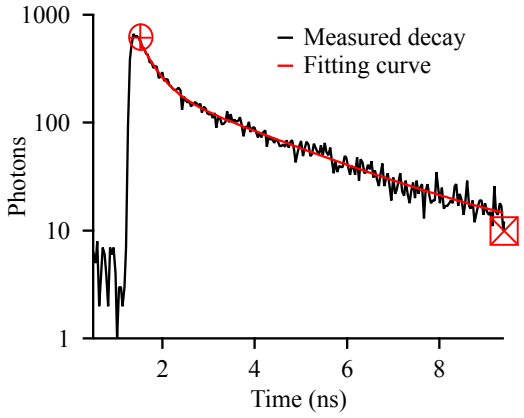

Figure 27. *Example measured (black) and fitted (red) fluorescence decay curves of mTurquoise2-YPet. Circle and square cursors flank the fitted region of the measured curve.*

In case of single exponential fitting the resulting lifetime was interpreted directly as the donor lifetime τ_D, in case of double exponential fitting the lifetime components and amplitudes were used to quantify amplitude weighted average lifetimes (eq. 19). FRET efficiencies were estimated by equation 6. The results showed no difference (single factor ANOVA, $p > 0.05$) to the ones, obtained by standard analysis in SPCImage Software (fig. 28).

Identical results obtained by these two methods showed a low effect of the IRF on the form of the fluorescence decay curve, which was possible, because IRF of the 2-photon system was very short in comparison to the FP decay.

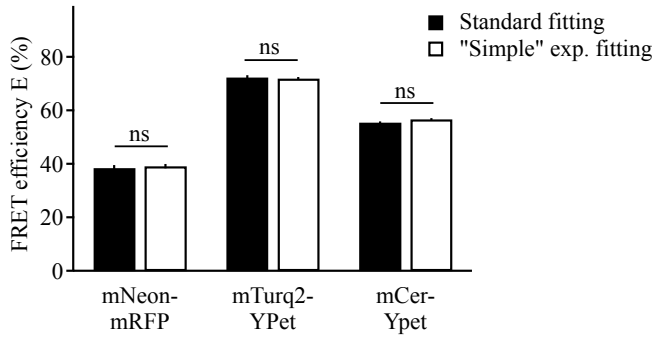

Figure 28. *"Simple" analysis demonstrates results similar to the standard re-convolution fitting for mNeon-mRFP, mTurquoise2-YPet and mCerulean-YPet FRET pairs. Single factor ANOVA was performed to compare the FRET efficiencies, not significant difference corresponds to p-values > 0.05.*

3.4.2 Normalized total photon count (NTPC)-based analysis

Another method we tried was based on the quantification of the total normalized photon count TNPC, which is an area under the peak-normalized fluorescence decay curve (fig. 29). The ratio of TNPC values of donor and donor-acceptor lifetime traces was applied for the FRET efficiency estimation (Methods, eq. 26).

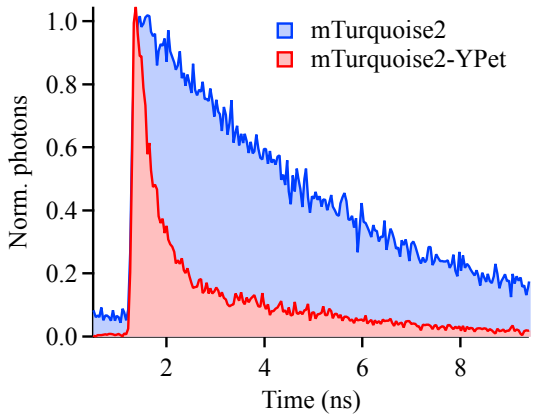

Figure 29. *Example of fluorescence decay traces of mTurq2 and mTurq2-YPet.*

Calculated FRET efficiency values were close to the ones, reached by the standard approach, although significantly smaller (fig. 30). This slight difference was caused by FRET efficiency underestimation by the TNPC method, which happened because the fluorescence decay curves didn't reach the background level before the next excitation pulse, as seen on fig. 29.

The disadvantage of this approach is that one looses the information about the decay: its complexity (number of components) and other parameters (like fractions of the lifetime components, defined by amplitudes a_i). On the other hand, this method allows estimation of the FRET efficiencies even when not enough photons were collected for a reliable fitting with a multi exponential function.

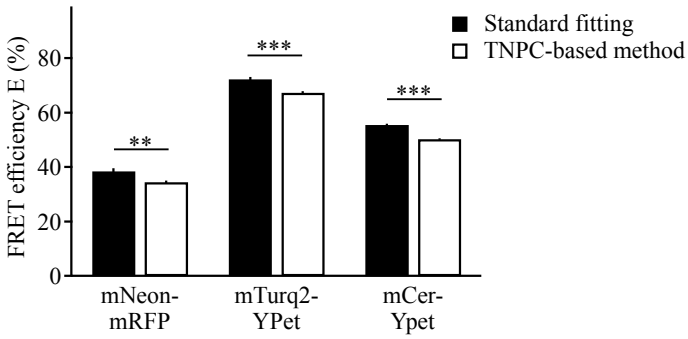

Figure 30. *TNPC-based analysis of mNeon-mRFP, mTurquoise2-YPet and mCerulean-YPet FRET pairs demonstrates significantly smaller FRET efficiencies in comparison to the standard re-convolution fitting. Single factor ANOVA was performed to compare the data, (**) corresponds to p-values < 0.005, (***) reflects p-values < 0.001.*

3.4.3 Spectral fitting analysis

Another method of FRET efficiency estimation was based on the fitting of the emission spectrum of the FPs experiencing FRET to the emission spectra of donor and acceptor alone (Bajar, E. S. Wang, et al. 2016). When the donor in the fusion pair was excited (at 480 nm wavelength in case of mNeon-mRFP and 435 nm in case of mTurquoise2-YPet), then the emission spectrum of the tandem demonstrated a two-hump shape (fig. 31): the first peak corresponded to donor emission, and the second one reflected emission of the acceptor, which was excited from the donor via FRET. Fitting to the donor-only and acceptor-only emission spectra, taking into account spectral properties of the FPs (such as quantum yields and the extinction coefficients) using the equation 27, provided the information about the FRET efficiency.

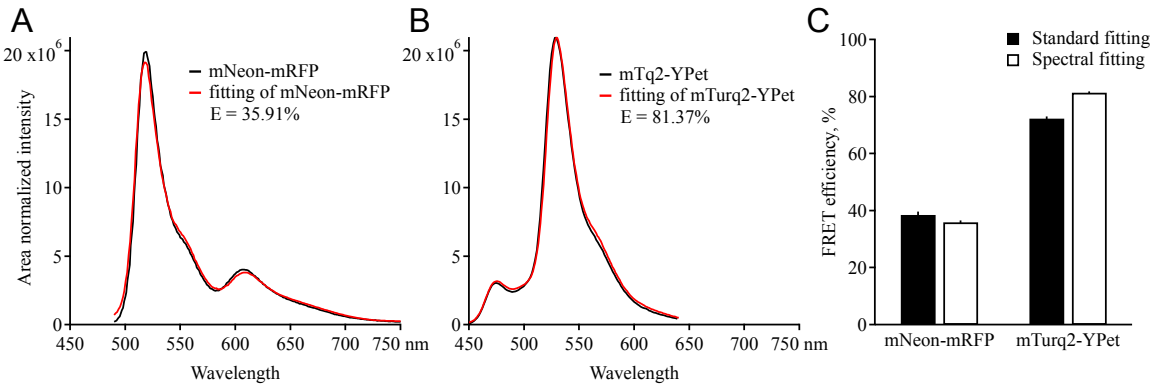

Figure 31. *Spectral fitting of mNeon-mRFP (A) and mTurquoise2-YPet (B) FRET pairs shows similar results to the standard analysis (C). Emission spectra were acquired from purified proteins (in case of fusion proteins) or from cellular suspensions (in case of donor-only and acceptor-only proteins) using a spectrofluorometer.*

This method didsn't provide any information about the details of FRET process such as fraction of molecules undergoing and not undergoing FRET. However, this approach was relatively fast and easy and therefore might be very useful for a preliminary screening of multiple FP pairs in regard to their FRET efficiencies.

3.4.4 Model-free graphical analysis

3.4.4.1 FPs and FRET pairs expressed in primary neurons

For the FRET efficiency estimation in previously described sections we used amplitude weighted average lifetime τ_M (eq. 19). It took into consideration both fast and slow lifetime components, which appeared after the double exponential fitting. Such approach suggested, that both components were involved in FRET, which might not always be the case for several reasons.

Firstly, there is a portion of freshly synthesized and therefore not yet mature (hence non-fluorescent) proteins; as described previously immature acceptors don't accept the energy. Secondly, flexible linker between the FPs allows their various orientations, part of which would not be favorable for an efficient FRET. Thirdly, some mature FPs may reversibly go into dark states and appear dark; if the acceptor is in the dark state, it cannot be excited.

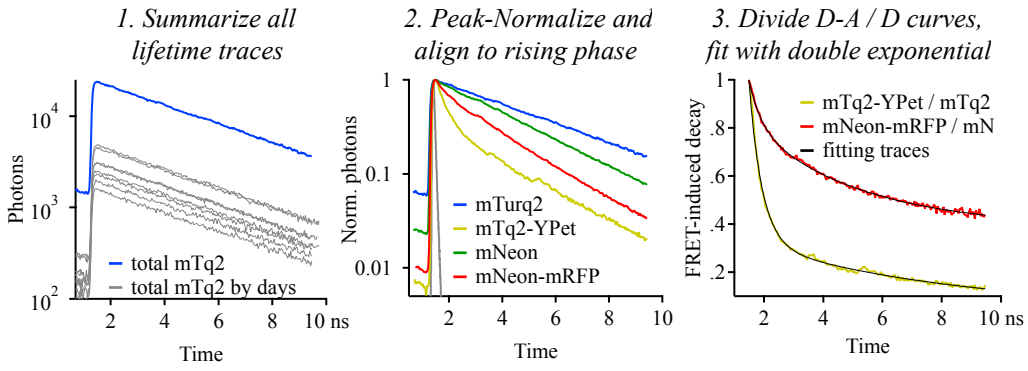

Figure 32. *Procedure of obtaining FRET-induced donor decay curves. Lifetime traces for each construct were summed over all acquisition days and peak-normalized. The traces for fusion proteins were divided by the corresponding donor lifetime trace, and the decay part of the resulting curves was fitted with a double exponential function.*

In all these situations donor doesn't transfer its energy and its lifetime stays unaffected, which leads to an underestimation of FRET efficiencies. An attempt to overcome this issue can be made if the slow lifetime component is assumed to represent non-FRET donor fraction and is therefore fixed at the value of the donor alone (as shown in fig. 24). However, it may lead to a problem of deciding, whether the slow lifetime describes the

non-FRET donor or a weak FRET process. Besides, it is inapplicable for the fusion pairs, when both lifetime components are much faster, than the donor-only lifetime.

An optimal approach would be a model-free one, which would allow independent quantification and description of different processes happening to the donor upon excitation. Such a method is described in (Peulen et al. 2017) and is based on calculating and analyzing the so called FRET-induced donor decay. The procedure of obtaining such decays is briefly explained in Methods (section 2.5.4) and on figure 32. First, an average donor fluorescence decay trace was obtained by means of summarizing all the individual traces measured for a certain construct. Next, the resulting curves were peak-normalized. Finally, the curve representing the fusion D-A pair was divided by the D-only curve; the resulting trace was the FRET-induced donor decay curve. It contained the information about species both undergoing and not undergoing FRET. In order to extract this information one had to fit the FRET-induced donor decay curve with the conventional double exponential function:

$$f(t) = y_0 + a_A e^{-(x-x_0)/\tau_A} + a_B e^{-(x-x_0)/\tau_B} \qquad \text{(Equation 28)}$$

In theory fluorescent protein alone or when experiencing FRET may have a mixture of species with different decay constants. For all the fusion pairs we tested (fig. 33) donors showed two species with decay constants τ_A and τ_B, corresponding to hi-FRET and low-FRET populations of molecules with the FRET efficiencies, estimated from equation 30 (see Methods).

Fractions of the hi-FRET rate and low-FRET rate populations were determined by parameters a_A and a_B respectively (eq. 28).

If the lifetime curve of the donor in presence of an acceptor had a non-interacting population, then after the division by donor-only curve, this population would turn into a constant equal to its fraction – this component was y_0 in the equation 28.

Since all the donor molecules either interacted with the acceptor or did not interact, the fractions of the hi-FRET, low-FRET and non-FRET populations followed the rule:

$$a_A + a_B + y_0 = 1 \qquad \text{(Equation 29)}$$

Where a_A was the fraction of the donor molecules interacting with the acceptor with the FRET efficiency E_A; a_B was the fraction of the donors interacting with the FRET efficiency E_B; y_0 was the fraction of non-interacting donors.

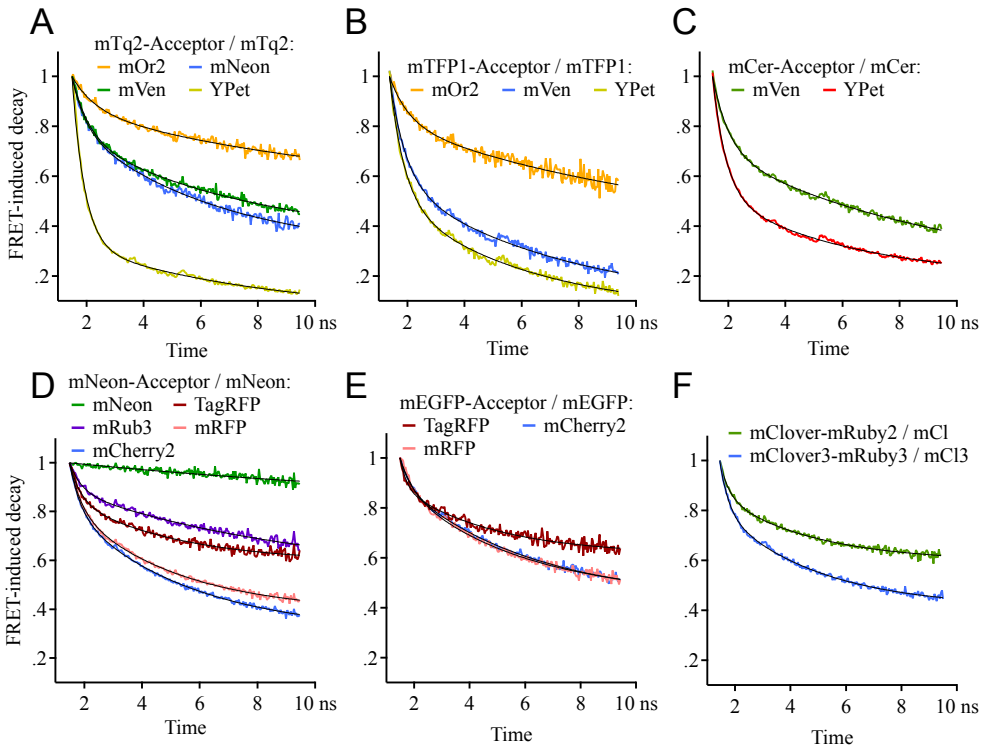

Figure 33. *FRET-induced decay traces (colored) and double exponential fitted curves (black) for all FRET pairs, expressed in primary neurons, namely for the cyan donors mTurquoise2 (A), mTFP1 (B) and mCerulean (C), green donors mNeon (D), mEGFP (E), mClover and mClover3 (F).*

Results of this model-free graphical analysis are presented on the fig. 34 panel A, where each tested construct is plotted twice: firstly (as empty markers) the FRET efficiency of hi-FRET rate population E_A against the corresponding fraction a_A and secondly (as filled markers) as the FRET efficiency of low-FRET rate population E_B against a_B. Non-interacting fraction y_0 is encoded as a marker size in the range from 3% (the largest marker) to 80%.

Hi-FRET population typically had the FRET efficiency above 80%. Pairs with the red and orange acceptors had a small fraction of hi-FRET rate population – usually not larger than 20%, whereas pairs with green acceptors mVenus and YPet had much larger hi-FRET rate fractions – up to 67.4% in case of mTurq2-YPet. At the same time the non-interacting fraction y_0 was large for pairs with red and orange acceptors (above 30%) and small for the pairs with yellow acceptors (less than 33%). Both these facts could be explained by the higher fraction of red proteins being in dark states. Green proteins had a lesser fraction in the dark states, hence a bigger protein fraction could accept the energy through FRET.

In this approach mTurquoise2-YPet FRET pair showed the best properties: among all the tested pairs it had the largest (67.4%) fraction of hi-FRET rate population with the FRET efficiency 90.5% and the lowest (4.5%) fraction of non-interacting donor.

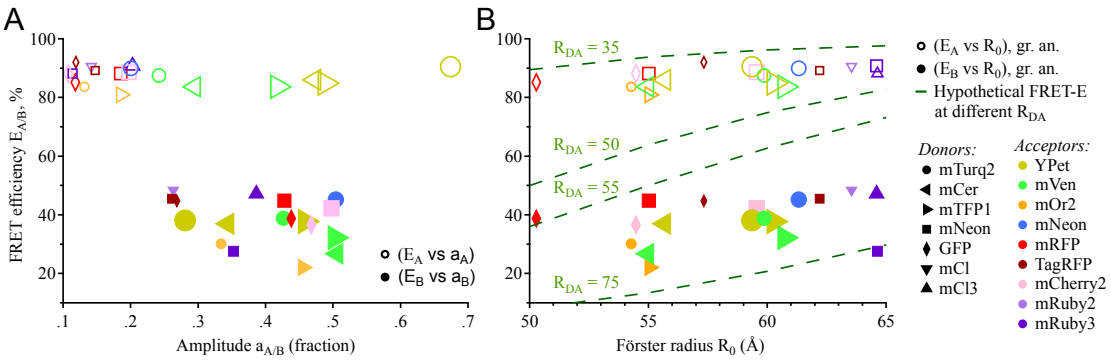

Figure 34. *Graphical analysis of the FRET-induced donor decay curves for the Donor-Acceptor fusion proteins, expressed in primary neurons. A – Fitting parameters of the graphical analysis are plotted as the FRET efficiency E_A / E_B against the corresponding fraction a_A / a_B. Marker shape encodes the donors, marker color encodes the acceptors (see the legend in B), marker size encodes non-interacting y_0 fraction in the range 3-80% (larger marker corresponds to a smaller y_0 fraction). B – FRET efficiencies E_A / E_B of the hi-FRET and low-FRET are plotted against the Förster Radii (values from table 1 in introduction): large Förster radius doesn't guarantee high FRET efficiency. Marker size encodes non-interacting y_0 fraction in the range 3-80% (larger marker corresponds to a smaller y_0 fraction). Dashed lines mark hypothetical FRET efficiencies calculated for various distances between donor and acceptor R_{DA} (Å): hi-FRET populations may reflect configurations of the fusion constructs, where donor and acceptor are located closer to each other.*

As mentioned before, FRET efficiency depends on the distance between the FPs and drops fast with the increase of the distance (Introduction, eq. 5). That is why pairs with a larger Förster Radius R_0 (distance between the FPs, at which the FRET efficiency is 50%) were predicted to have a higher FRET efficiency. A strong performance of mTurquoise2 / YPet pair would not be expected from the R_0 data (fig. 34, panel B), because it was not the largest among tested pairs: for comparison R_0 is 5.9 nm for mTurquoise2 / YPet, 6.1 nm for mTurquoise2 / mNeon, 6.5 nm for mNeon / mRuby3 (table 1). It indicated, that there might be other factors influencing the FRET performance of the pairs being tested, for example preferred configurations with better or worse conditions for FRET performance. In conclusion, R_0 is a good, but not an absolute predictor of FRET efficiency, thus one should not rely exclusively on R_0 comparison.

Fused FRET pairs had two populations with different FRET rates. This situation might reflect different configurations of the constructs: comparison with the theoretically estimated FRET efficiencies for different distances between the FPs R_{DA} suggested, that the hi-FRET rate molecules might have such an orientation, that the FPs were located in a close proximity to each other (apparently the distance between the proteins was in a range 3.5 – 5.0 nm), whereas low FRET-rate population reflected the proteins with the larger distance between donor and acceptor (fig. 34, panel B).

Taken together with the previous analysis approach, mTurquoise2 / YPet was the best FRET pair tested, as it had the largest FRET efficiency and the lowest non-interacting fraction of molecules.

3.4.4.2 Performance of mNeon-TagRFP in emetine treated HEK293T cells

As mentioned before, FRET between FPs expressed in HEK293T cells was underestimated in comparison to the expression in primary neurons due to slower maturation of the acceptor. We performed model-free graphical analysis (fig. 35) of the lifetime traces of mNeon-TagRFP acquired in emetine treated and control HEK293T and compared them to the ones obtained in cultured neurons, in order to investigate the influence of the acceptor maturation on the fitting parameters during graphical analysis.

In case of HEK293T cells expressing mNeon-TagRFP for 24 h (fig. 35, panel A), at time point 0 h after the treatment there were present two populations of donors experiencing FRET with the same FRET efficiencies, as observed in primary neurons: E_A was 90.24% (89.18% in neurons) and E_B was 46.60% (45.44% in neurons). As expected, amount of interacting proteins was less in HEK293T cells: a_A is 13.9% vs 14.7% and a_B was 19.2% vs 26.1%; at the same time the non-FRET fraction y_0 in HEK293T cells was larger: 66.9% vs 59.2%.

24 h after transfection HEK293T cells had already produced a lot of FPs, which keep maturing, therefore the fractions of interacting proteins grew with time in the control cells reaching the level obtained in primary neurons approximately 6 h later. Treatment of the cells with the RNA and protein synthesis inhibitor emetine speeded up this process, so that the fractions of interacting proteins a_A and a_B became the same as the ones in case of neurons 3 h after the treatment. These interacting fractions kept growing, until they reached 19.5% and 33.6% respectively 6 h after emetine treatment. By this time all produced FPs should already be mature, hence these numbers corresponded to the maximal possible interacting fractions for the fusion mNeon-TagRFP pair.

If HEK293T cells expressed mNeon-TagRFP for 12 h (fig. 35, panel B), the fraction of immature acceptor was extremely high (> 90%) within the first hour of observation of the control cells. The fractions of interacting donors increased with time in control cells, but they stayed much less, than the ones in HEK293T cells 24 h after transfection, because the portion of newly produced immature proteins was very large 12 h after transfection.

Emetine treatment increased the interacting fractions a_A and a_B drastically, until they reached 17.4% and 25.5% respectively, which was similar to the values observed in primary neurons.

FRET efficiencies of hi- and low-FRET fractions E_A and E_B were similar across primary neurons and HEK293T cells.

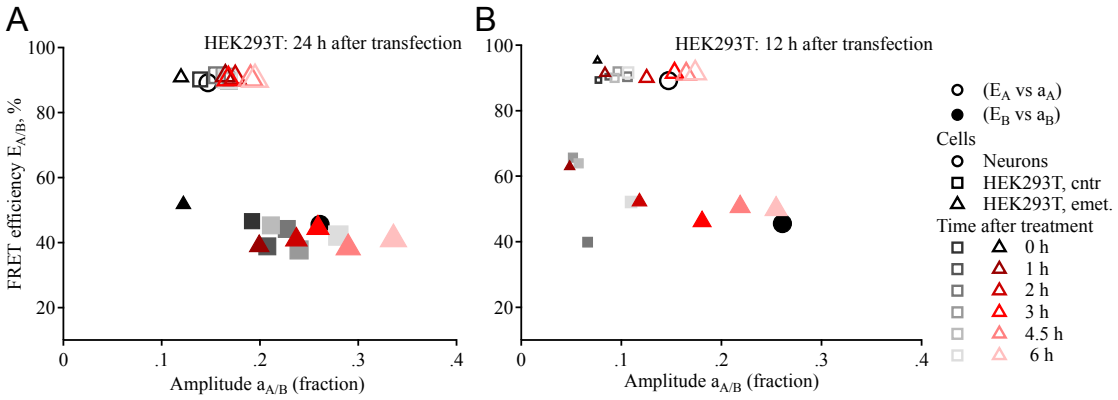

Figure 35. *Graphical analysis of mNeon-TagRFP expressed in primary neurons (circles) as well as in HEK293T cells treated with protein and RNA synthesis inhibitor emetine (triangles) or with water (control, squares) 24 h (A) or 12 h (B) after transfection. Shade of color shows time after treatment between 0 h (dark) and 6 h (light) for emetine treated (red) and control (gray) HEK293T cells. Marker size encodes the non-interacting fraction y_0 in a range 45-100% (larger marker corresponds to a smaller y_0 fraction).*

3.5 Deciphering FRET phenomenon in mTurq2 / YPet and mNeon / mRFP pairs

As mentioned previously mTurquoise2 / YPet had a highly efficient FRET performance, which apparently resulted from a close proximity between the donor and the acceptor in a fusion pair, as shown in the section 3.4.4.1 (fig. 34, panel B). This is possible, if the fusion pairs form heterodimers, leading to a close approach of donors and acceptors from two tandems. Another explanation might be interaction between the donor and acceptor within the same fusion construct, resulting in a preferred conformation with high FRET efficiency.

To research this closer we decided to investigate the performance of the best FRET pairs of this study mTurq2 / YPet and mNeon / mRFP in a purified condition, as it is then easier to control protein concentrations.

3.5.1 Most of the purified FPs are monomers

Purification and fast protein liquid chromatography (FPLC) of the mNeon / mRFP and mTurquoise2 / YPet fluorescent proteins (both alone and as fusion pairs) was performed in the working group of Prof. Dr. Matthias Geyer (Institute of Structural Biology, Biomedical Centre, University Clinic Bonn, University of Bonn) as described in the Methods section 2.1.8.

Almost all the FPs and both fusion pairs ran as expected according to their masses (fig. 36), which indicated, that these proteins did not dimerize. The only exception was YPet, which ran higher, than expected – almost at the same level as the fusion proteins. Apparently, YPet was not a monomeric protein.

Since mTurquoise2-YPet didn't dimerize, the nature of the outstanding FRET performance must be in the conformation, which the fusion protein took.

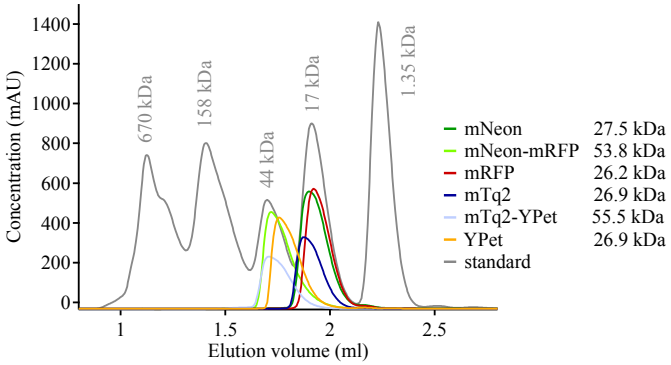

Figure 36. *FPLC of the purified fluorescent proteins and of a standard probe shows, that mNeon, mNeon-mRFP, mRFP, mTurquoise2 and mTurquoise2-YPet are monomers, whereas YPet is not.*

3.5.2 Interaction between individually expressed donor and acceptor is very weak

To test to which extent individual FPs interact with each other, we prepared several D + A mixtures of purified FPs varying in acceptor amount. The donor was used in a concentration of 1 µM; acceptor concentration varied in a range between 1 µM and 300 µM. Low protein amounts prevented strong interaction and accidental close proximity between the proteins – this reflected the non-FRET situation. With the increase of the acceptor concentration increased the probability of two freely floating proteins to meet and to perform FRET.

We carried out experiments with mTurq2 + YPet and mNeon + mRFP mixtures (fig. 37).

As expected, when acceptor was applied in a low concentration, the fluorescence decay curve behaved the same way as in case of donor only. With the increase of YPet concentration the fluorescence decay of mTurquoise2 became slightly faster, however it never reached the level of the fusion mTurquoise2-YPet protein (fig. 37, panel A).

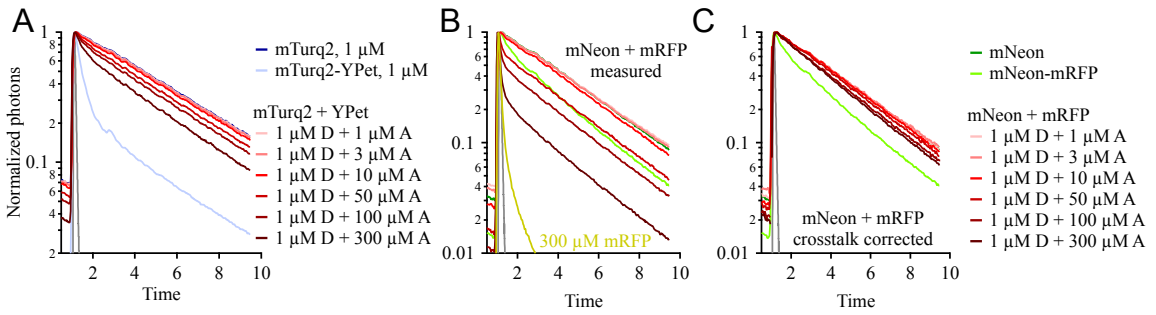

Figure 37. *Peak normalized donor fluorescence decay histograms of mTurq2 + YPet (A), mNeon + mRFP (B) and mNeon + mRFP after crosstalk correction (C) in comparison to the curves acquired from donor alone and fusion donor-acceptor constructs. Donor + Acceptor mixtures were prepared in the following concentrations: 1 µM D + 1 µM A, 1 µM D + 3 µM A, 1 µM D + 10 µM A, 1 µM D + 50 µM A, 1 µM D + 100 µM A, 1 µM D + 300 µM A. All curves were acquired using 2-photon FLIM. Crosstalk signal from 300 µM mRFP solution measured with mNeon emission filters is shown in panel B.*

When the same experiment was performed for mNeon and mRFP, we saw a very strong effect in the beginning of the decay part of the curves upon increase of the acceptor concentration (fig. 37, panel B). This phenomenon appeared as a result of the mRFP crosstalk: such a fast decay could not derive from an interaction – otherwise we would have seen it in a fusion construct. It rather reminded the signal, acquired from mRFP-only solution with all the settings (laser wavelength and power, filters) used for mNeon signal acquisition at the 2-photon FLIM (fig. 37, panel B). Observed mRFP-only signal was best fit with a triple exponential function with the following lifetimes (and corresponding amplitudes): 0.09 ns (92%), 0.47 ns (7%), 1.60 ns (1%). Solutions with mNeon and mRFP mixtures, when fit with a triple exponential function, clearly had the fast 0.09 ns-component; its fraction was between 38% (for 50 µM mRFP) and 81% (in case of 300 µM mRFP). Although the mRFP crosstalk was not too high by itself: as mentioned earlier, the maximal crosstalk was detected for TagRFP at the level of 7% on average when coexpressed at comparable levels with mNeon. However, it started to play a role when the amount of mRFP drastically exceeds the amount of mNeon molecules. The lifetime decay curves for mNeon + mRFP mixtures were corrected for the crosstalk as described in Methods section 2.4.8, resulting curves are demonstrated on the fig. 37, panel C. Acceptor crosstalk was not such a problem for the mTurq2 / YPet pair.

Next, the FRET-induced donor decay curves were obtained (fig. 38 panels A, B) for mTurq2 + YPet and for acceptor crosstalk corrected mNeon + mRFP mixtures. They were fitted with single or double exponential fitting functions and the model-free graphical analysis was applied (fig. 38, panels C, D). F-test was used to decide between the fitting models as described in Methods section 2.4.6.

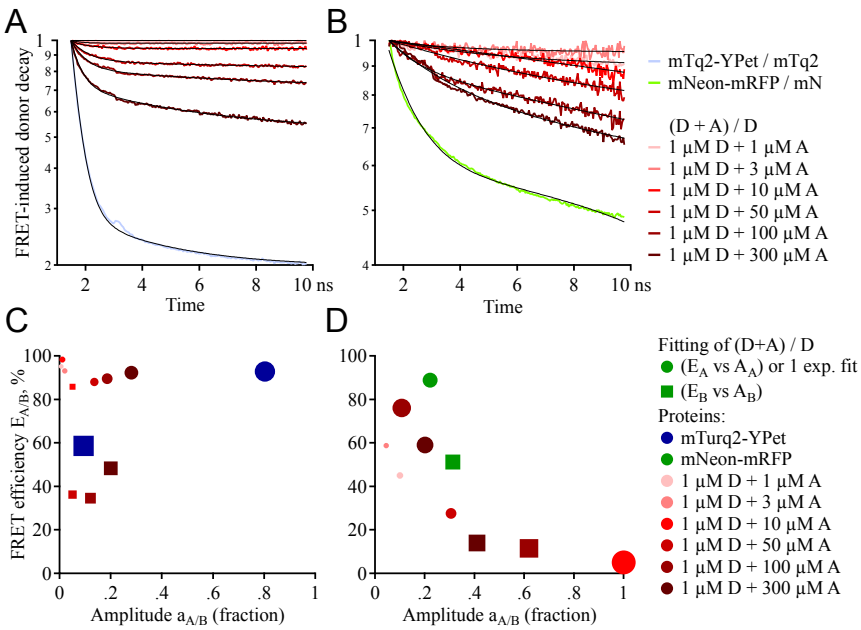

Figure 38. *Model-free graphical analysis for Donor + Acceptor mixtures, given for the following concentrations: 1 µM D + 1 µM A, 1 µM D + 3 µM A, 1 µM D + 10 µM A, 1 µM D + 50 µM A, 1 µM D + 100 µM A, 1 µM D + 300 µM A. A, B – FRET-induced donor decays for mTurq2 / YPet (A) and mNeon / mRFP (B) FRET pairs. C, D – results of the graphical analysis for mTurq2 + YPet (C) and mNeon + mRFP (D) mixtures obtained by fitting of the FRET-induced donor decay curves shown in panels A, B. Marker size encodes non-interacting y_0 fraction in the range 0-100% (larger marker corresponds to a smaller y_0 fraction).*

When the acceptor was present in small concentrations, then the donor lifetime decay curves were best fit with a single exponential function and the non-interacting y_0 fraction was very large (typically > 90%), which meant, that there was no interaction detected. With the increase of YPet concentration the y_0 fraction decreased (which is seen as the increase of the marker size in fig. 38, panel C), along with the increase of both a_1 and a_2 fraction representing the amount of hi-FRET and low-FRET rate populations. In other words mTurq2 and YPet performed FRET more often with the increase of YPet concentration. The same tendency was also seen for mNeon + mRFP mixtures (fig. 38, panel D), although to a less extent – probably due to a higher noise level in the curves after crosstalk correction (fig. 38, panel B).

In case of 1 µM mNeon + 10 µM mRFP mixture the fitting result showed a high interaction fraction (99%), however the FRET efficiency of the interaction was only 5%, which indicated that the detected interaction was negligible. This point was excluded from the further analysis.

To sum up, a weak interaction between the donor and the acceptor was detected at higher acceptor amounts. To estimate the strength of this interaction we plotted the level of

the non-FRET fraction y_0 against the acceptor concentration (fig. 39) and fitted it with the Hill function (Methods, eq. 31) to calculate the dissociation constant K_D as described in Methods section 2.6. During the fitting with a free parameter n, which reflected stoichiometry of the D + A interaction, n resulted in values close to -1 (around -0.7 for mNeon + mRFP and -0.8 for mTurq2 + YPet). Therefore, this parameter was fixed at the value -1 for the fitting (eq. 31).

Resulting K_D values were 269.0 ± 23.9 µM for mTurq2 + YPet and 82.9 ± 29.6 µM for mNeon + mRFP. This value indicated the acceptor concentration at which half of all donor molecules (with a donor concentration of 1 µM) would be interacting with the acceptor.

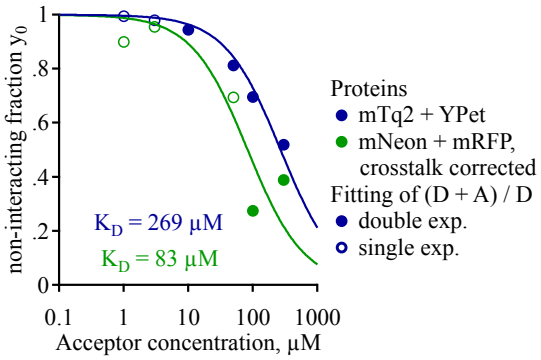

Figure 39. *Estimation of K_D between donor and acceptor. Non-interacting y_0 fraction for D + A mixtures is plotted for different acceptor concentrations. Fitting with the Hill function gives K_D values 269.0 ± 23.9 µM for mTq2 + YPet and 82.9 ± 29.6 µM for mNeon + mRFP.*

These dissociation constants were pretty large, indicating a presence of a very weak interaction between the proteins.

With the increase of the acceptor concentration in the solution the probability of an occasional localization of the freely floating proteins close enough for FRET also becomes higher, which might contribute to the observed interaction level. To understand the impact of such a situation, we predicted, how the donor decay traces would look like if the donor and the acceptor would not interact and FRET would happen exclusively due to an occasional close proximity between the proteins in a homogeneous solution. The calculation is described in detail in Methods section 2.7. Resulting donor decays are shown in Fig. 40 panels A and B. Finally, model-free graphical analysis was applied on them and the fitting with a Hill function (eq. 31) was performed to the acceptor concentration vs. y_0 correlation graph (fig. 40 panel C). The resulting K_D values were 18.7 ± 1.1 mM for mTurq2 / YPet pair and 44.6 ± 7.6 mM for mNeon / mRFP. These values were much larger, than the ones obtained for the measured D + A mixtures.

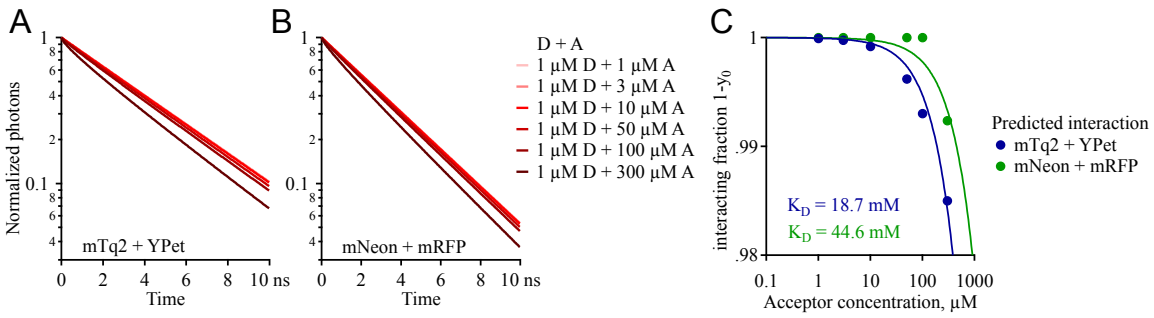

Figure 40. *Donor fluorescence decay curves, predicted for mTurquoise2 + YPet (A) and mNeon + mRFP (B) mixtures, where FRET is happening only due to occasional close proximity between the freely floating proteins. C – interacting fraction for D + A mixtures was calculated from the predicted decays on panels A and B. Fitting with the Hill function gives K_D values 18.7 ± 1.1 mM in case of mTurq2 + YPet and 44.6 ± 7.6 mM in case of mNeon + mRFP.*

This leads to the conclusion, that not bound pairs of mNeon / mRFP and mTurq2 / YPet fluorescent proteins had a certain degree of physical interaction, which resulted in a stronger FRET, than the one predicted from an occasional close localization of free proteins. However, this interaction was very weak and became noticeable only at large acceptor concentrations.

Apparently, this interaction led to such a conformation of a fusion D-A pair, which caused appearance of a hi-FRET fraction of molecules.

3.5.3 Fusion FRET pairs: comparison between cellular expression, purified and crystalized conditions

As shown above, the nature of the high FRET efficiency of the mTurquoise2-YPet construct is explained by the conformation of the fusion pair. The most reliable way to investigate the orientation and the distances in the fusion protein is to crystalize it (McPherson & Gavira 2014). Crystallization of mTurquoise2 and mTurquoise2-YPet proteins (Methods section 2.1.9) was performed by Dr. Kanchan Anand from the group of Prof. Dr. Matthias Geyer (Institute of Structural Biology, Biomedical Centre, University Clinic Bonn, University of Bonn).

The structure of the crystals was researched by Dr. Anand, geometry is described in more detail the Discussion section 4.8.

3.5.3.1 FRET performance in different environments

Crystalized mTurquoise2 proteins usually were larger, than mTurquoise2-YPet crystals. mTurquoise2-YPet crystals were either needle-like or formed groups of needle-like

crystals. mTurquoise2 crystals as well often had a needle-like shape, some crystals had a sheet-like form. Exemplar images are shown in figure 41.

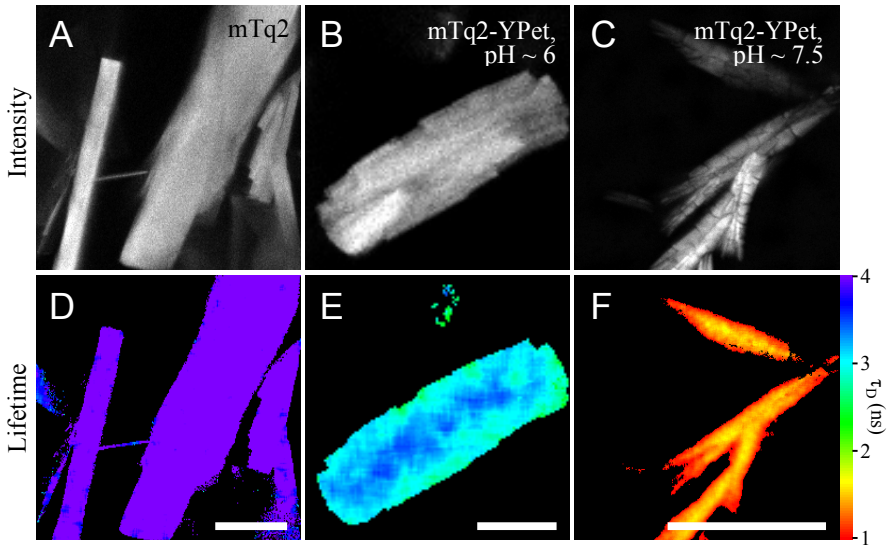

Figure 41. *Representative donor intensity (A-C) and donor lifetime (D-F) images of mTurq2 (A, D) and mTurq2-YPet (B, E) crystals. Mild alkalization of mTurq2-YPet crystals shortens the donor lifetime to the expected values (C, F). Images were acquired with a 2-photon FLIM setup. Scale bar 30 µm, color-coded scale bar 1.0 – 4.0 ns encodes the donor lifetime.*

Donor lifetimes of the crystals were estimated using a 2-photon FLIM system. Lifetime of the mTurquoise2 crystals didn't differ (single factor ANOVA, $p > 0.05$) from the lifetime of mTurquoise2 expressed in primary neurons (fig. 42). However, mTurq2-YPet had an unexpectedly slow lifetime (fig. 41, panel E), which was best fitted with a single exponential function (in contrast to the double construct expressed in neurons). Possible reason could be a lower pH of the surrounding solution (around 6.0), which quenched the pH sensitive acceptor. After mild alkalization with 20 mM NaOH pH rose to around 7.5 and YPet restores its properties, which led to a stronger lifetime reduction of the donor: it became double exponential and approached the values observed in primary neurons, as seen in fig. 42. Change in the pH destroyed the crystals (fig. 41, panel C), which was probably the reason why the lifetime (in crystal 1.32 ± 0.03 ns) didsn't reach exactly the same value as in primary neurons (1.15 ± 0.03 ns) ($p < 0.01$, singe factor ANOVA).

Donor lifetimes were also compared between purified proteins and the ones expressed in cultured neurons (fig. 42). mTurq2-YPet construct didn't show any significant difference between these environments ($p > 0.05$, singe factor ANOVA). Although mTurquoise2, mNeon and mNeon-mRFP showed different donor lifetimes ($p < 0.01$, singe factor ANOVA), the resulting values were pretty similar across different environments.

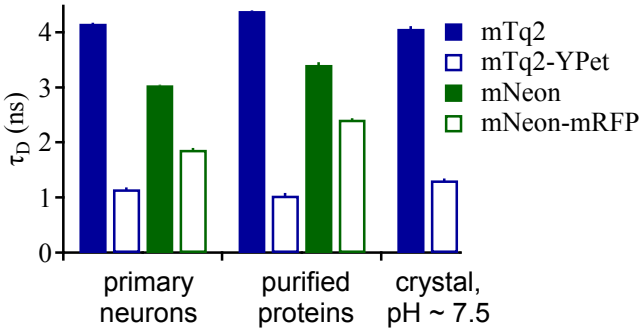

Figure 42. *Comparison of the performance of the fusion proteins mNeon-mRFP and mTurquoise2-YPet, as well as corresponding donor-only constructs between the proteins expressed in primary neurons, purified and crystallized samples; data is obtained using the 2-photon FLIM setup. Proteins perform similar in different environments. Lifetimes of donors-only is shown as monoexponential τ ± SEM, lifetimes of donors in presence of acceptors is given as averaged lifetime τ_M ± SEM.*

Model-free graphical analysis further demonstrated similarities of protein performance in different surroundings (fig. 43). Fusion constructs had similar fractions of hi-FRET rate populations and non-interacting fractions.

Destabilization of the mTurq2-YPet crystals by the increased pH (~ 7.5) might explain lower hi-FRET rate fraction in comparison to the soluble protein.

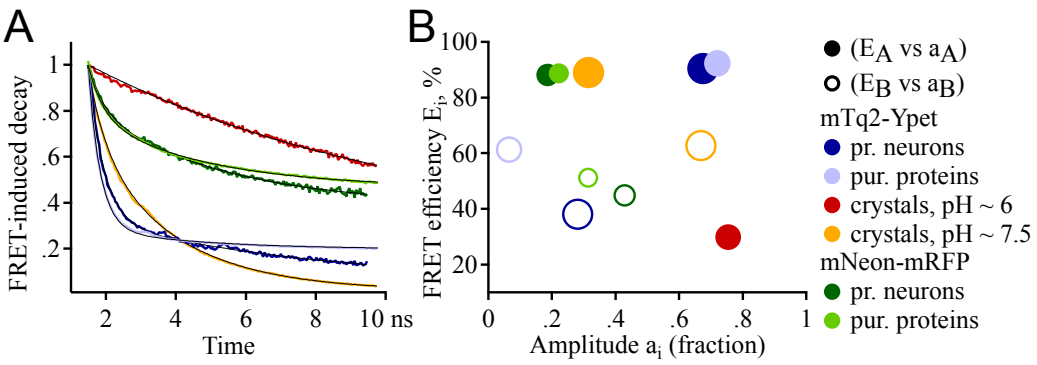

Figure 43. *FRET-induced donor decays (A) and the results of their fittings with a single or double exponential function (B) show, that the mTurquoise2-YPet and mNeon-mRFP proteins behave similar in different environments. Marker size encodes the non-interacting fraction of molecules in a range 0-100% (lower fraction has a larger marker size).*

3.5.3.2 Linear dichroism of the mTurquoise2-YPet crystal reveals its structure

As mentioned before, protein crystals provide structural information about the protein of interest. In case of FP crystals, some structural information may be extracted from the fluorescence properties of the crystal.

When using linearly polarized light (for example, a laser) fluorophores preferably get excited by the light, which electric field is parallel to the absorption dipole of the

fluorophore itself – a characteristic called linear dichroism (fig. 44). The probability of the photon absorption is proportional to $\cos^2\varphi$, where φ is the angle between the direction of the electric field of the excitation light and the dipole of the molecule.

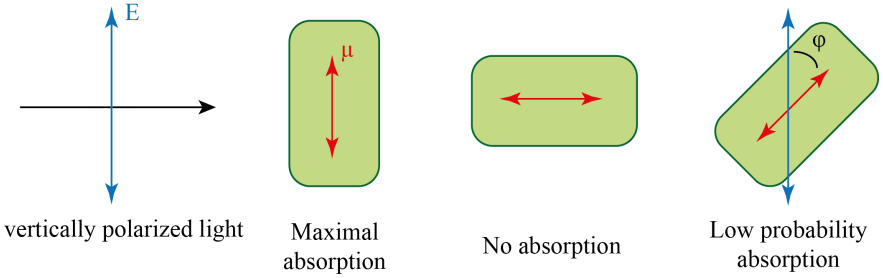

Figure 44. *Efficiency of light absorption by the molecule depends on the polarization angle φ between the electric field E of the incoming light and the electric dipole moment of the molecule μ.*

In isotropic solution single fluorophore molecules rotate much faster (50-100 ps), than stay excited (1-10 ns), therefore emission light is usually weakly polarized or not polarized at all (Lakowicz 2006). However, it was shown, that the crystals grown from native GFP are photoselective: the intensity of the crystal fluorescence depends on the angle between the polarization light and the crystal axis (Inoue et al. 2002).

In order to verify this finding for mTurquoise2-YPet crystals, we performed subsequent rounds of crystals excitation, while changing the angle of the polarized excitation light between 0° and 180° (which correspond to 12 and 6 o'clock on the acquired images respectively) (fig. 45). Laser light beams oriented by 0° and 180° regarding the starting polarization, were parallel to each other and therefore were expected to produce the same emission. These experiments were performed using a 2-photon Prairie Technologies system together with Gunther van Dyk, a PhD student in the laboratory of Dirk Dietrich (Institute of Neurosurgery, University Clinic Bonn, University of Bonn).

When mTurquoise2-YPet crystals were excited with a 2-photon laser, they fluoresced with different intensity. Since the light coming from the laser was polarized, crystals were excited with different efficiencies depending on the mutual orientation of the fluorescent chromophore and the direction of the polarized excitation light. Representative images of crystals upon excitation of mTurquoise2 and YPet proteins achieved at laser wavelengths 820 nm and 980 nm respectively are shown in figure 46 panels A, B.

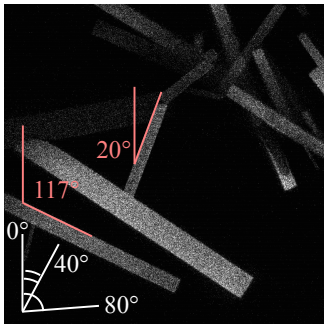

Figure 45. *Representative image of mTurquoise2-YPet crystals, acquired using a 2-photon setup. Angles of polarization light (white) varied between 0° (vertical orientation) and 180° with 20° steps during measurements. Fixed crystal orientation (pink) was measured as the angle between crystal axis and the vertical direction. Angle between crystal and polarized light is the difference between the angle of polarization light (white) and the crystal axis (pink).*

In case of mTurquoise2, the fluorescence intensity of the crystals changed with the change of the polarization angle, reaching maximum, when the crystal long axis and the polarization plane of the excitation light were in parallel. This was the case for all 80 crystals imaged in 4 experiments, representative images and their quantification are shown in fig. 46 panels A, D. Crystals, almost invisible at X° angle of electric field, achieved a peak of fluorescence at (X+90)°. These observations demonstrated that mTurquoise2 proteins within mTurquoise2-YPet were located similarly to the native GFP in crystals: they were aligned with the crystal axis and the crystals were uniaxial.

However, this was not the case for YPet proteins within the mTurq2-YPet crystals. Although the crystal intensity varied with the change of polarization angle, the angle at which maximal fluorescence intensity was measured didn't follow a clear fluorescence pattern across different crystals (fig. 46 panel E).

Linear dichroism of the crystals gave an insight to their structure, which could be further investigated by the X-ray analysis.

A general view on the barrels and chromophores of the fused pair of mTurquoise2 and YPet within the crystal is shown in fig. 47 panels A, B. View of multiple proteins at a time demonstrates presence of two species of each mTurq2 and YPet with different orientations in space (fig. 47 panels C, D). Two species of chromophores had different angles between their dipole and the polarization light. Therefore, the observed crystal fluorescence was actually a combination of emission of two species.

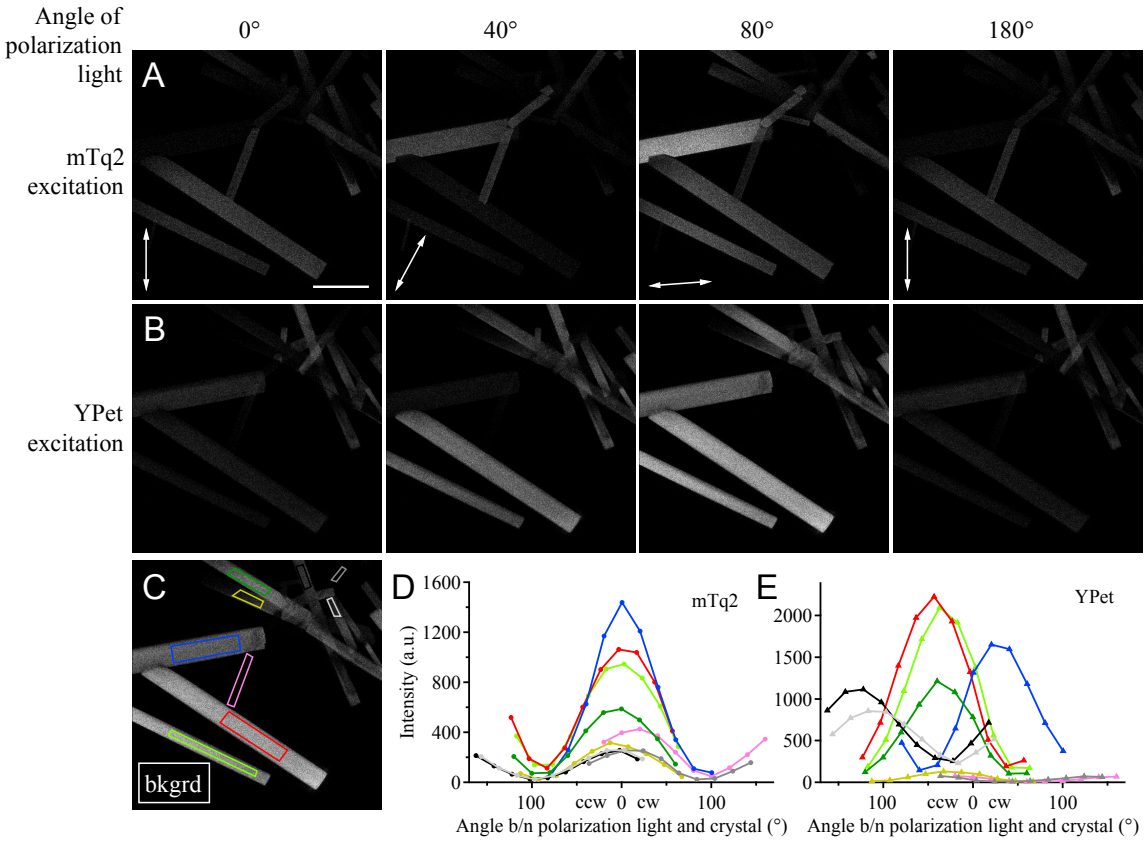

Figure 46. *Fluorescence intensity of FPs depends on the angle between polarization light and the crystal. mTurquoise2 (A) and YPet (B) in the fusion construct were excited with a 2-photon laser at 820 nm or 980 nm wavelength respectively. Initial direction of polarization light 0° is oriented vertically in regard to the image (shown with vertical arrow-headed line in panel A). Then the direction of the excitation light polarization was changed in 20° steps, until a range of 180° was covered. C – E – fluorescence intensity dependence on the angle φ between the crystal axis and polarization light (cw – clockwise, or ccw – counterclockwise) was estimated for both mTurquoise2 (D) and YPet (E) of the crystallized fusion protein. Fluorescence intensity quantified for individual crystals, marked with different colors, was collected from ROIs of corresponding colors (C). Scale bar: 50 µm.*

To excite a fluorophore with a 2-photon laser, two exciting photons must be absorbed simultaneously by the fluorophore. Since the probability of such a situation is the product of their individual probabilities, the probability of absorption of two photons is proportional to $\cos^2\varphi * \cos^2\varphi = \cos^4\varphi$ (Lakowicz 2006). Each fluorescent protein was represented by two species of differently oriented molecules, that's why the intensity curves of crystal emission should be fitted with a sum of two $\cos^4\varphi$ components. Almost all the curves (for 80 crystals) of fluorescence intensity dependence on the angle φ between the polarization light and the crystal axis were nicely fitted (Methods eq. 25, representative curves are shown in fig. 48). Only two curves couldn't be fitted due to a very low signal-to-noise ratio and were therefore excluded.

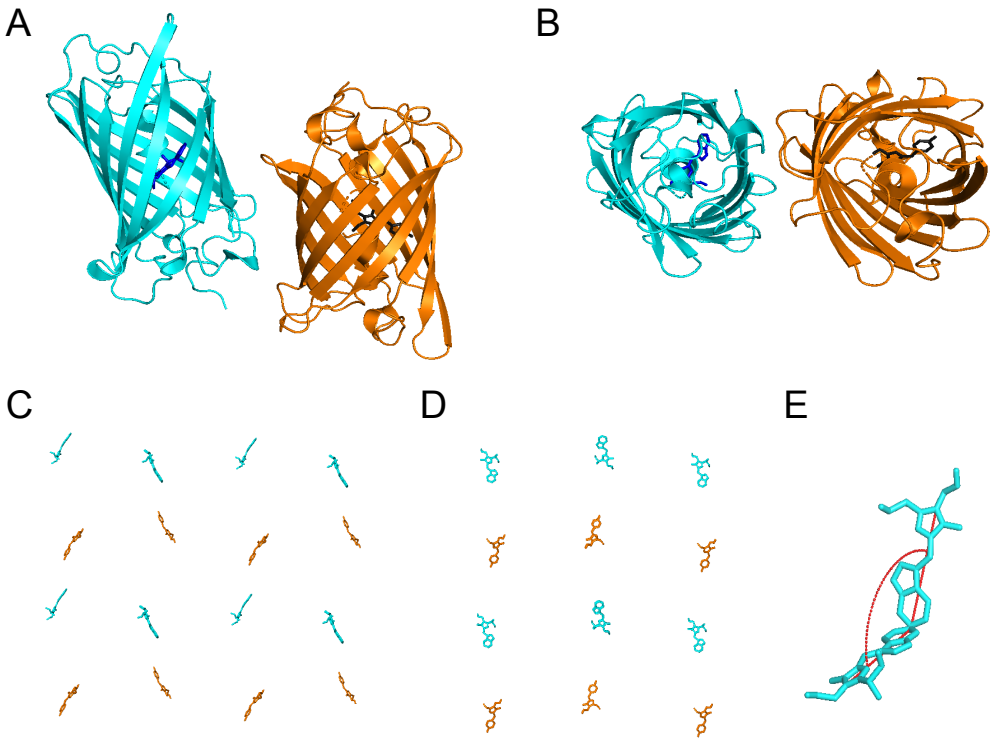

Figure 47. *Structure of mTurquoise2-YPet crystals acquired using X-Ray structure analysis. A, B – side (A) and top (B) views of mTurquoise2 (cyan) and YPet (orange) barrels of the fusion protein with chromophores (dark blue and gray) inside. C, D – different views on the group of mTurquoise2 (cyan) and YPet (orange) chromophores within the crystal. Each type of the chromophores is represented by two differently oriented populations. E – two mTurquoise2 chromophores shifted in such a way, that their atoms on one end overlap. Red lines mark the angle 126.6° between the chromophores. Angles between other chromophores were calculated the same way (table 16).*

We used the PyMol software to calculate the distances and angles between the chromophores in the X-Ray structures. Distance between mTurquoise2 and YPet chromophores of the fusion pair was estimated between the middle atoms of both chromophores using a distance measurement tool and was found to be around 3.7 nm, which was much shorter, than the predicted Förster Radius R_0 of this pair 5.8 nm.

The chromophores were moved using a "3 Button Editing Mode" in PyMol until the atoms on one side of the chromophores overlapped. Since the dipole was close to the line connecting the aromatic rings, we used it to estimate the angles between the chromophores, as shown in fig. 47 panel E. Resulting angles are listed in table 16.

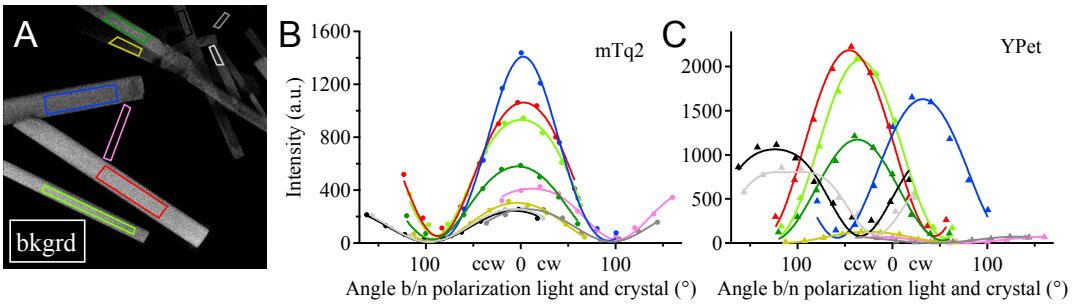

Figure 48. *Representative curves from fig. 46 panels D-E, showing fluorescence intensity change across angles φ between the polarization light and the crystal axis, are proportional to $\cos^4\varphi$ (fitting to eq. 25).*

The angle between the chromophores of the fused mTurquoise2 and YPet was around 60°, which is not optimal for FRET (maximal FRET is achieved at 0°, minimal FRET is at 90°), which was apparently compensated by the close distance between the proteins.

Different species of mTurq2 and YPet were never parallel. Therefore YPet chromophores were not aligned along the long crystal axis as mTurq2 chromophores were. It explained why, unlike mTurq2, maximal YPet excitation was almost never reached when the crystal axis was parallel to the electric field of the polarized light (φ = 0° or 180°), as seen on fig. 46 panel E and fig. 48 panel C. Due to different dipole orientations of mTurq2 and YPet, YPet dipole was also shifted in regard to the long crystal axis. As a result, the degree of crystal rotation along its long axis affected the angle between YPet dipoles and the angle of polarization light, which led to the variability between the crystals regarding the angle of crystal maximal emission intensity.

Table 16. *Anlges between chromophores within mTurquoise2-YPet crystals, as drawn in fig. 47 panel E*

Chromophores	Angle between chromophores	180° - Angle
mTq2 / mTq2	126.6°	53.4°
YPet / YPet	127.2°	52.8°
mTq2 / YPet of fusion pair	120.1°	59.9°
mTq2 / YPet	158.1°	21.9°

3.6 Verification of the FRET pairs in native neurons and in subcellular synaptic compartments

3.6.1 FPs show similar performance when expressed in primary and native neurons

To further test FRET between the most promising FP pairs of our study *in vivo* we prepared rAAV1/2 viruses for mNeon, mNeon-mRFP, mTurq2 and mTurq2-YPet constructs. We injected them into the hippocampi of 7-week old wild type mice and

prepared acute mouse brain slices 9-17 days later. Hippocampi were measured using the two-photon FLIM setup (fig. 49 panels A, B). FPs were strongly expressed and showed bright fluorescence.

Donor fluorescence decay traces acquired in brain slices (fig. 49 panel C) looked almost the same as the ones measured in primary cultures, resulting in similar lifetime values of the constructs (fig. 49 panel D).

Hence, these FPs are applicable for the studies in brain slices and living animals.

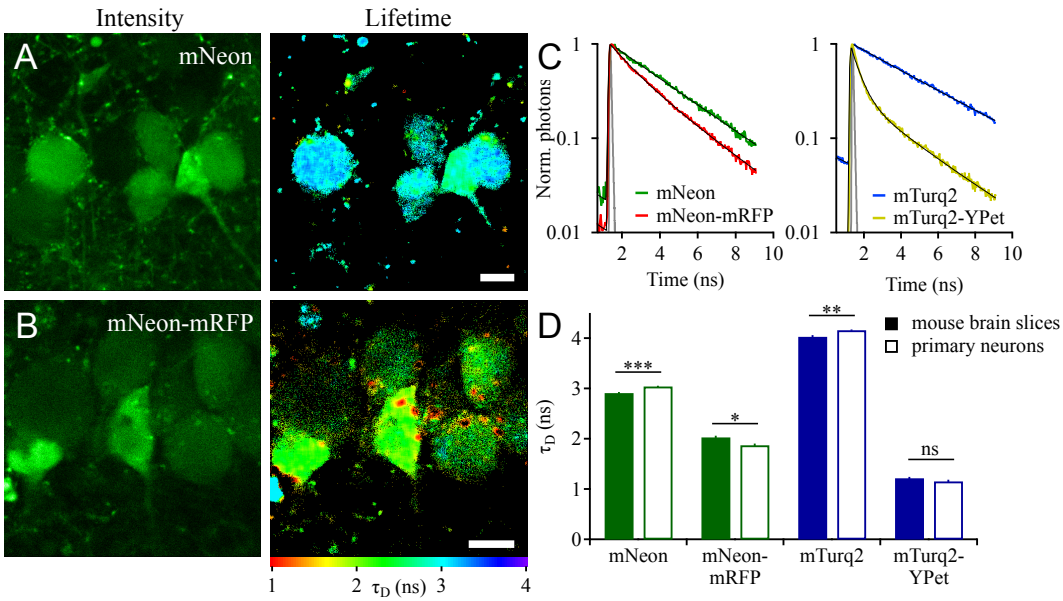

Figure 49. *FPs expressed in native neurons behave the same way as when expressed in primary neurons. A, B – representative donor intensity and donor lifetime images of hippocampal CA1 neurons expressing mNeon (A) and mNeon-mRFP (B) in acute brain slices of wt mice after rAAV injections. Images were made using a 2-photon FLIM system, scale bar 10 µm, color-coded scale bar 1.0 – 4.0 ns. C – representative donor fluorescence decay curves in presence and absence of the acceptor, traces were acquired in native neurons. D – lifetimes of donors-only (monoexponential τ ± SEM) and donors in fusion constructs (τ_M ± SEM) don't differ much between expression in native and primary neurons, n = 6 mice. Single factor ANOVA was applied to statistically compare donor lifetimes in primary and native neurons.*

3.6.2 mTurquoise2 / YPet FRET pair is applicable for PPI studies

Finally, we decided to verify, if the most promising FRET pair of this study may be used for the detection of cellular protein-protein interactions in cultured neurons.

Protein interactions form the basis of all the events happening in living organisms, in particular the presynaptic release machinery of neurons consists of a large amount of proteins, however the role of their individual interactions is not fully understood. FRET-based approaches including the two-photon FRET-FLIM method are useful techniques, which have the advantage of performing experiments in living cells.

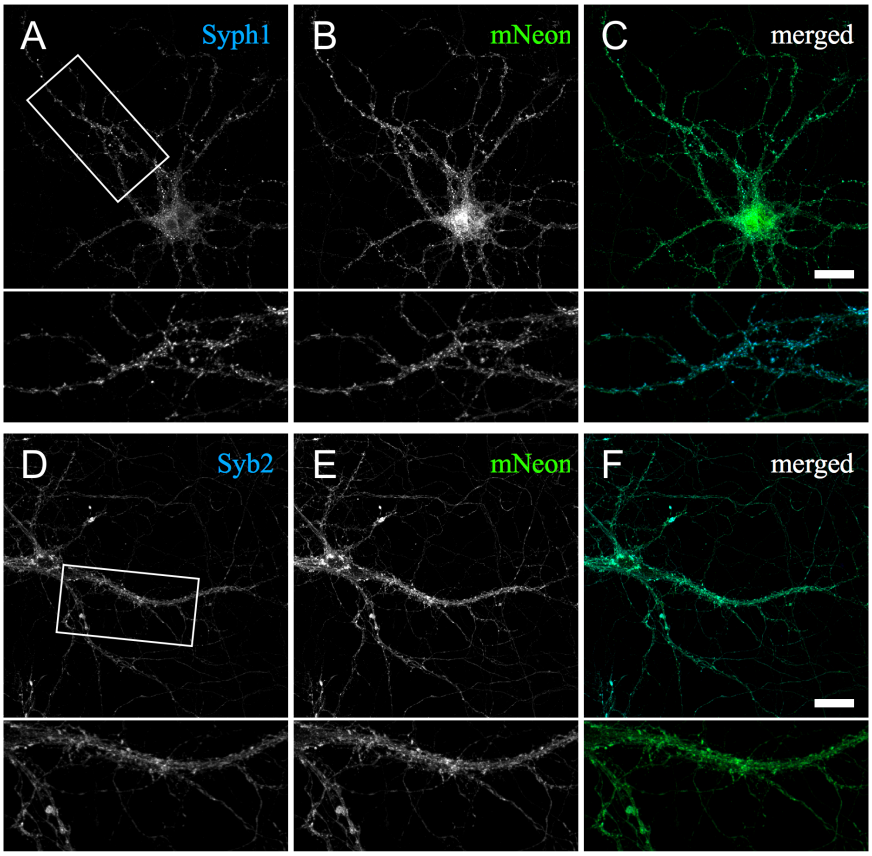

Figure 50. *Synaptophysin1-mNeon and mNeon-Synaptobrevin2 proteins are targeted to the synaptic compartments of primary neurons. A – C – representative confocal images (above) and zoomed areas (below) of neurons expressing Syph1-mNeon and stained against Syph1 using rabbit Alexa405 antibody are shown in blue (A), green (B) and merged (C) channels. D – F – images of neurons expressing mNeon-Syb2 and stained against Syb2 with mouse Alexa405 antibody. Merged images (C, F) demonstrate strong colocalization of mNeon and stained proteins, as well as punctate pattern typical for presynaptic proteins. Images were taken using a confocal microscope, scale bar 30 µm.*

As a proof of principle we chose Synaptophysin1 (Syph1) and Synaptobrevin2 (Syb2), two presynaptic vesicle proteins, which were known to interact with each other. However, the role of this interaction for neurotransmitter release is poorly understood (Gordon & Cousin 2013). We fused FPs to the chosen cellular proteins via the same flexible linker SRG_4SG_4S, as the one used for the comparison studies of FRET pairs. We prepared crude viral rAAV1/2 extracts and used them to transduce primary mouse cortex cultures. Neurons had a sufficient fluorescence 1-2 weeks later, when they were imaged at DIV 14-17. Confocal imaging (fig. 50) showed that the expressed constructs were primarily located in the synapses of primary neurons, but they were also distributed all over the neuronal cytoplasm due to a strong overexpression. Stained presynaptic proteins perfectly colocalized with the FP signal, indicating that there was no destruction of the fusion protein.

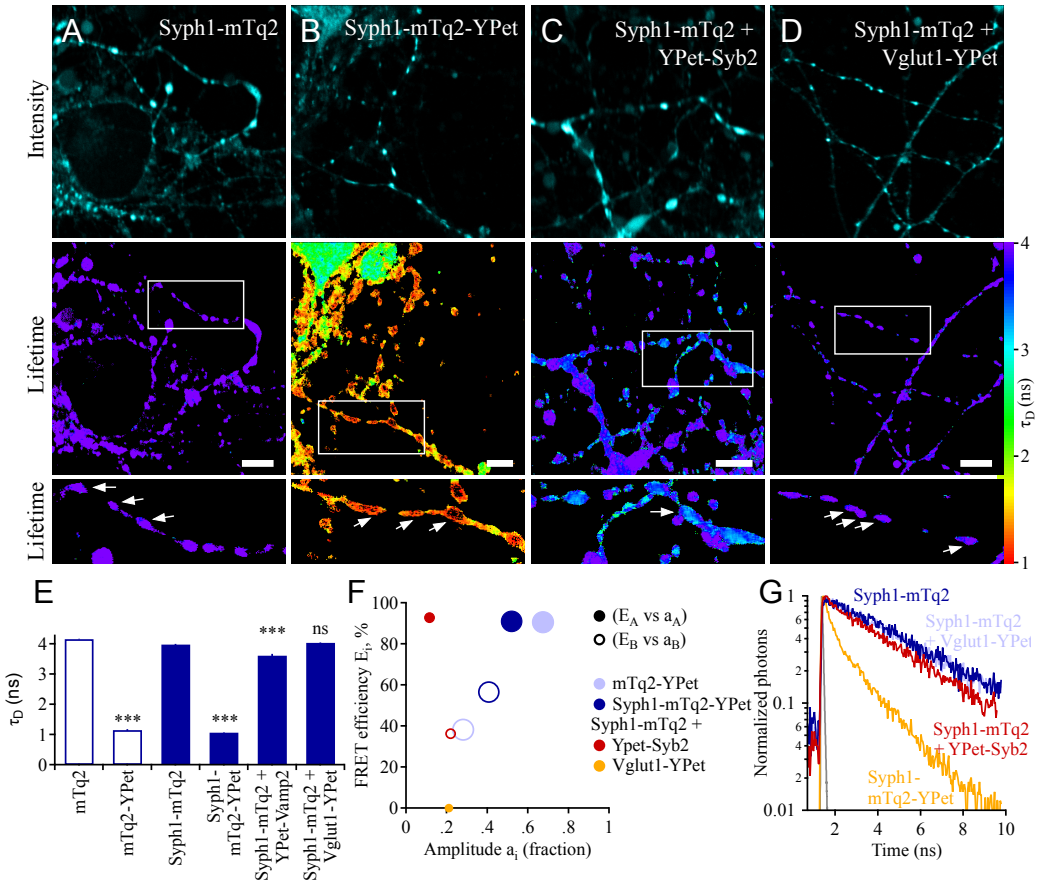

Figure 51. *Verification of the Syph1-Syb2 interaction in primary cortex neurons was performed using 2-photon FLIM. A – D – representative donor intensity (above) and donor lifetime images (middle, zoomed in images below) of the neurons expressing Syph1-mTurq2 (A), Syph1-mTq2-YPet (B), coexpressing Syph1-mTurq2 and YPet-Syb2 (C), Syph1-mTurq2 and Vglut1-YPet (D). Scale bar 10 µm, color-coded scale bar 1.0 – 4.0 ns. When Syph1 and Syb2 are coexpressed, the donor lifetime gets slightly decreased indicating the interaction. Syph1 and Vglut1 don't interact; hence, the donor lifetime stays unaltered. E – fusion to the presynaptic protein does not alter neither the donor lifetime nor its reduction due to FRET. F – model-free graphical analysis further shows similar performance of mTurq2-YPet and Syph1-mTurq2-YPet. When Syph1-mTurq2 and YPet-Syb2 are coexpressed, there appear a hi-FRET and low-FRET rate populations representing interacting proteins, non-interacting population is high, because not all presynaptic proteins interact. Non-interacting fraction of molecules is encoded by the marker size in a range 0-100% (lower fraction has a larger marker size). G – representative donor fluorescence decay curves for the tested constructs were acquired from ROIs marked with arrows on the zoomed images on panels A – D.*

2-photon FLIM of transduced neurons demonstrated, that neither the donor lifetime nor its reduction in presence of the acceptor was affected by the fusion to the presynaptic protein (fig. 51, panel E). When Syph1-mTurq2 and YPet-Syb2 fusion constructs were coexpressed in one neuron, donor proteins experienced FRET (fig. 51). Not all Syph1 molecules interact with Syb2, that is why in comparison to Syph1-mTurq2-YPet the non-interacting fraction was high (66.5%) and the fractions of hi- and low-FRET rate

populations were low (11.5% and 22.0% respectively) (fig. 51, panel F). Negative control was performed by the coexpression of Syph1-mTurq2 and Vglut1-YPet constructs, which don't interact in cells. As expected, the FRET-induced donor decay curve for these cells didn't show any decay.

A phasor plot provided another model-free method of quick estimation of lifetime changes. It allowed representing raw information about the donor lifetime decays in polar coordinates using the equations 15 and 16 listed in Methods.

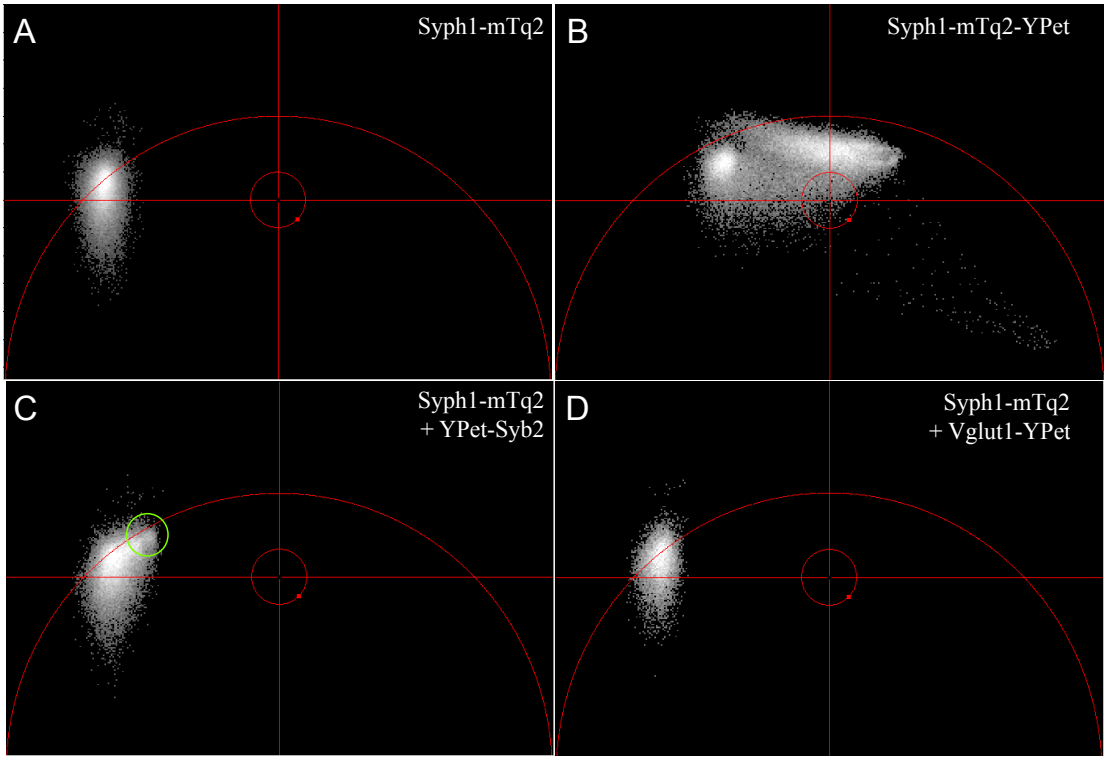

Figure 52. *Phasor plots of FLIM images, shown in fig. 51 panels A-D in the middle. Data on the semicircle reflects monoexponential decay, data inside the semicircle represents double exponential decay. Cells coexpressing Syph1-mTq2 + YPet-Syb2 demonstrate a fraction of interacting donors marked with green circle in panel C.*

In case of Syph1-mTq2 the majority of the lifetime decays fell on a semicircle (fig. 52 panel A), which indicated that the lifetime of mTurquoise2 was monoexponential. A "tail" of points below represented dim pixels from the FLIM image, which appeared in the background of the image.

In case of Syph1-mTq2-YPet (fig. 52 panel B) all the data points were concentrated inside the semicircle, which meant that the lifetime was double exponential. The points were shifted to the right in comparison to the phasor plot for Syph1-mTq2, which indicated, that the donor lifetime of Syph1-mTq2-YPet construct was shorter.

When Syph1-mTq2 was coexpressed with Vglut1-YPet (fig. 52 panel C), the resulting phasor plot looked exactly the same as for Syph1-mTq2, meaning that Syph1-mTq2 didn't interact with Vglut1-YPet.

For Syph1-mTq2 and YPet-Syb2 coexpression (fig. 52 panel D) the main fraction of points also didn't show any interaction. However, there was some fraction of Syph1-mTq2 interacting, which resulted in a slightly shorter donor lifetime, leading to the shift of this species to the right from the main fraction (marked with the green circle).

Overall this experiment demonstrated, that mTurquoise2 / YPet FRET pair could be well applied for the PPI studies.

4 Discussion

Two-photon FRET-FLIM is a useful technique to study protein-protein interactions in live cells, however it is still challenging to choose a suitable FRET pair for such studies. In this work we compared a large number of donor-acceptor pairs under identical conditions to find the best one. The performance of 20 FRET pairs fused via a flexible short linker and expressed under the control of a ubiquitous CMV promoter was tested in primary neuronal cultures. mTurquoise2 / YPet and mNeon / mRFP demonstrated the best results among cyan / yellow and green / red pairs respectively. mTurquoise2 / YPet pair had an outstanding performance among all tested pairs due to the largest fraction of active acceptors and the tendency of the fusion pair to arrange in a way optimal for FRET. Therefore, among FPs used in this study mTurquoise2 / YPet pair is the best one for the 2-photon FRET-FLIM experiments in neurons and neuronal subcompartments.

4.1 FRET-FLIM is a powerful approach for protein interaction studies in living cells

Protein-protein interactions form the basis of all processes in cells, therefore it is important to study them. A lot of importance was given to such research in biology, therefore a big variety of methods has been developed for this purpose, some of which are described in Introduction section 1.3. PPIs vary in strength (strong/weak) and timing (permanent/transient), which makes some interactions easier to detect, than the others. A variety of circumstances, which accompany a certain research, give the preference to a particular technique, as every approach has its advantages and disadvantages.

For example, a high throughput search for potential interaction partners of a particular protein of interest might be performed using phage display or two-hybrid method or their modifications (Phizicky & Fields 1995). This method has a high false positive rate, therefore found interaction partners should be verified by other methods, such as co-immunoprecipitation (Phizicky & Fields 1995). However, it needs application of a good antibody, which is not always possible, in such case a pull-down assay (Lucas 2004) might be performed.

The traditionally used methods for PPIs, including the mentioned ones, have a common disadvantage, namely it is very difficult, time-consuming or even impossible to use them to study the dynamics of transient interactions, which happen only in a certain biological context. Moreover, such studies are pretty hard to perform in subcellular compartments.

The possibility to genetically label a protein of interest with a fluorescent protein in combination with advanced microscopy imaging gives an opportunity to overcome these problems and to conduct the studies in living cells and on subcellular level. Evolution of the FP color palette and in particular its application for FRET further improves the procedure, as not simply colocalized labeled proteins of interest are detected, but the ones in a very close proximity, which is usually possible due to physical interaction. One of the most reliable and direct methods of FRET estimation is the donor lifetime quantification, because it almost doesn't dependent on the instrument being used. Moreover, only a minimal amount of corrections is needed, compared to other approaches such as spectral crosstalk correction, acceptor photobleaching and others (Day & Davidson 2012), because the lifetime is independent of the fluorescence intensity (and hence protein concentration) and the requirement to measure only the donor simplifies the choice of filters.

FRET efficiency depends on a spectral overlap between the FPs, their proximity and orientation. In order to make a comparison across a large list of FP pairs for their FRET properties we connected donors with acceptors via a flexible and relatively short linker: donor-SR$(G_4S)_2$-acceptor. Glycine and serine are widely used in linker design, because glycine has the smallest residual and thereby provides flexibility, whereas serine improves the solubility of the glycine oligopeptide (Miyawaki et al. 2003). Donor lifetimes in such constructs were always reduced. This reduction was caused by FRET, because neither creation of a homo-dimer mNeon-mNeon nor fusion to the cellular protein (namely Syph1-mTurq2) led to a relevant alteration of the donor lifetime. Moreover, acceptor photobleaching returned the donor lifetime value to the donor-alone state, which further proved, that the donor lifetime reduction was the result of FRET.

FLIM allows a high temporal and spatial resolution, which is beneficial for investigations on a subcellular level.

Two-photon excitation laser gives extremely brief light pulses, which ensure good temporal resolution. Additionally, two-photon microscopy is a powerful tool for *in vivo* studies due to low tissue absorbance, deep tissue imaging and low autofluorescence. Disadvantage of this type of light source is a pretty broad excitation spectrum of the FPs, leading to an unintended direct acceptor excitation. This results in an acceptor crosstalk into the donor emission signal, which can be minimized by application of appropriate emission filters.

Lifetimes measured for the donor-only samples are in agreement with the previously reported values (Tramier et al. 2006; Padilla-Parra et al. 2009; Shaner et al. 2013).

4.2 Slow maturation and dark states of red acceptors make them less favorable choice

There are some properties of FPs, which might affect the quantification of the FRET efficiency of the pair. One of such properties is the maturation time. Maturation includes protein folding and the consequent chromophore formation. Red-emitting proteins have an additional oxidation step in comparison to cyan and green fluorescent proteins, and their maturation usually lasts much longer (more details in Introduction section 1.2.2). Maturation times of some FPs used in this study are listed in table 17.

Table 17. *Times it takes for 90% or 50% (half-maturation time) of different fluorescent proteins to mature at 37°C. Data for mRuby2 is from (Lam et al. 2012), for other FPs from (Balleza et al. 2017).*

Fluorescent protein		90% maturation time (min)	50% maturation time (min)
Cyan	mCerulean	24	7
	mTurquoise2	95	34
Green	mNeon	37	11
	mEGFP	42	15
	mClover	62	22
	mClover3	112	44
Yellow	YPet	34	10
Red	mRFP	51	22
	TagRFP	103	42
	mCherry2	51	23
	mRuby2		150
	mRuby3	342	131

An immature FP can neither be excited, nor emit energy. Immature donors would be invisible for the lifetime measurements; this might slightly decrease the signal intensity, but not alter the estimated lifetime. However, much more often happens an opposite situation, namely a mature donor is fused to a still maturing acceptor. An immature acceptor would not accept the energy coming through FRET from the interacting donor protein. In this situation a fraction of donor molecules, located close and correctly oriented to the acceptor protein, will show no lifetime decrease. In the experiments comparing multiple FRET pairs this effect would lead to an underestimation of the FRET efficiencies. In PPI studies this might potentially decrease the detected level of interaction or even make it invisible. This problem plays a big role, when the proteins are expressed in rapidly dividing cells such as HEK293T. These cells constantly produce large amounts of proteins needed for new cells; as a result population of the fusion FRET pairs with immature acceptor becomes striking. It was nicely demonstrated in our study by the presence of

highly diverse cells in regard to their red-green fluorescence ratios and donor lifetimes (fig. 18). This makes HEK293T and other fast dividing cells less preferable for methods involving FRET estimation.

To overcome this obstacle for the FRET efficiencies comparison one could pretreat the cells with RNA and protein synthesis inhibitor (like emetine) and perform the imaging several hours later. The population of immature FPs would then be eliminated (fig. 19). Disadvantages of this approach are a decrease of the health status of the cells and less experimental flexibility. Furthermore, this method is hardly applicable for PPI studies due to toxic influence of the synthesis inhibitors on the cell biochemistry.

A different approach would be the usage of the slowly dividing or not dividing differentiated cells, as they are supposed to produce fewer proteins, hence already synthesized FPs would be mostly fully mature. Neuronal cultures are an appropriate model for this purpose and, indeed, contain a negligible fraction of immature FPs (fig. 20).

Another phenomenon with a similar outcome is that a certain fraction of the fully mature FPs is in a dark state, where they cannot be excited neither directly nor by FRET. For example, around 46 ± 1 % of mRFP molecules transit into the dark state upon 24 kW/cm^2 excitation (Hendrix et al. 2008). FPs go into dark states reversibly for tens of µs (Hendrix et al. 2008) due to photoisomerization and/or changes in hydrogen-bond network. If the acceptor is in the dark state, then the donor will demonstrate an unquenched lifetime.

There are methods allowing estimation and exclusion of the donor fraction, which for some reason cannot transfer its energy to the acceptor.

4.3 Interpretation of the lifetime components

When the donor has an acceptor fused to it, its lifetime gets always reduced. The donor fluorescence decay curves of the tested pairs were fit the best with the double exponential function. Sometimes the slow lifetime component τ_2 was almost undistinguishable from the donor-only lifetime τ_D: (green-red) mNeon-mRFP, mNeon-TagRFP, mNeon-mRuby3, mEGFP-mRFP, mEGFP-TagRFP, mEGFP-mCherry2, mClover-mRuby2, mClover3-mRuby3, (cyan-yellow) mTurquoise2-mOrange2, mTFP1-mOrange2. For these pairs τ_2 apparently represents the non-interacting donor fraction, which appears when the acceptor is immature or in a dark state and doesn't accept the energy (see section 4.2 for more details). The fast component τ_1 represents the interacting donor and can be used for the

FRET efficiency estimation (fig. 24). The corresponding amplitude a_1 reflects a fraction of interacting donor molecules.

Exclusion of the slow donor lifetime greatly increases the calculated FRET efficiencies (fig. 24, panels C, D) up to around 60% in case of mNeon-mRFP, mNeon-TagRFP and mClover3-mRuby3.

Such approach might lead to difficulties, as it is hard to decide whether the slow lifetime component indeed represents the unquenched donor or a weak FRET process.

Moreover, many pairs show two lifetime components, each of which is clearly shorter, than the donor-only lifetime, namely (green-red) mNeon-mCherry2, (cyan-yellow) mTurquoise2-YPet, mTurquoise2-Venus(L68V), mTurquoise2-mNeon, mTFP1-YPet, mTFP1-Venus(L68V). In addition, it is extremely hard to separate the unquenched fraction when the donor alone already decays double exponentially, which is the case of mCerulean for example.

4.4 FRET efficiency variability

FRET between two fluorophores depends on external properties of the environment and internal properties of the fluorophores, namely orientation, distance, spectral properties of the fluorophores (donor emission and acceptor excitation spectra must overlap > 30%). FRET can be characterized by such a parameter as the FRET efficiency E (eq. 5):

$$E\ (\%) = \frac{1}{1+(\frac{R_{DA}}{R_0})^6} \qquad \text{(Equation 5)}$$

Where R_{DA} is the distance between the dipoles of the fluorophores, R_0 (Förster Radius) is the distance where half of the donor energy is transferred to the acceptor (table 1).

$$R_0 = \sqrt[6]{\frac{9ln10}{12\pi^5 N}\frac{\kappa^2 Q_D J}{n^4}} = 0.0211\sqrt[6]{\kappa^2 n^{-4} Q_D J} \qquad \text{(Equation 7)}$$

Where N – Avogadro's number per mmole, n is the refractive index of the medium, κ^2 is the orientation factor for dipole-dipole coupling (can vary between 0 and 4, equation 35), Q_D is the fluorescence quantum yield of the donor in absence of the acceptor, J is the overlap between donor emission and acceptor excitation spectra (in $nm^4M^{-1}cm^{-1}$, table 1).

In order to estimate FRET efficiencies between the chosen FRET pairs we tried to perform experiments under identical conditions. We fused the donors with the acceptors via a flexible and relatively short linker (12 aa, which is ~ 3 nm long). On one hand, the proteins stay close enough to each other and approximately at the same distance among all

the tested constructs. On the other hand, flexibility of the linker potentially allows almost random orientation of the FPs. Orientation factor κ^2 (fig. 53, eq. 35) is assumed to equal 2/3 for freely rotating proteins.

$$\kappa^2 = (cos\theta_\tau - 3cos\theta_D cos\theta_A)^2 = (sin\theta_D sin\theta_A cos\psi - 2cos\theta_D sin\theta_A)^2 \qquad \text{(Equation 35)}$$

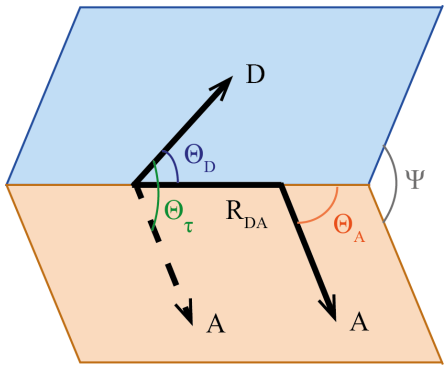

Figure 53. *Scheme of the dipole orientations for Donor D and Acceptor A (Lakowicz 2006).*

This brings to an assumption, that R_0 could be a predictor of the FRET efficiency. However, the measured FRET efficiency doesn't correlate with the calculated R_0 (fig. 34 panel B). For example mTurquoise2-YPet pair, which demonstrated the highest FRET efficiency among the tested pairs, didn't have the largest R_0.

A possible explanation could be that the fusion pairs have preferable orientations, which would lead to a shorter R_{DA} distance and/or to an increase of the κ^2. Such orientations might be caused by the properties of the β-barrel, forming the shape of the FP. For example, it was shown that the mutations S208F and V224L in both YPet and CyPet proteins lead to an enhanced association with each other. It consequently results in a four fold increase of the CyPet / YPet emission ratio in the fusion CyPet-linker-YPet construct and in a 16-fold change in emission ratio after the linker cleavage (Vinkenborg et al. 2007). Pairs of FPs, which have a tendency to heterodimerize, should be tested for their application in PPI studies and improvement of the biosensors. Both high FRET and a large dynamic range (strong difference between interacting and non-interacting states) are desired.

4.5 Comparison of different analysis approaches

Extremely fast laser pulses (around 150 fs) along with a fast hybrid PMT create a very short instrument response function IRF (with half-width of about 89 ps), which is almost negligible in comparison to the long fluorescence decays of the FPs. This is confirmed by

the absence of a significant difference between the results obtained from a standard reconvolution approach used in SPCImage software and from a simple fitting of the donor decay curves performed in Igor Pro (fig. 28).

An accurate fitting of the donor decays requires low noise of the curves. For a fitting with double exponential functions around 10^4 photons in a marked region of interest (ROI) should be collected in a curve for a reliable re-convolution. Taking into account restriction on the photon count rate of the conventional detectors, which is important to avoid its oversaturation, the acquisition might take some time (from ms to min range) before a desired photon amount is reached. A way to avoid it could be a TNPC method, where the FRET efficiency is calculated as a ratio of the peak-normalized photon counts of the donor in presence and absence of the acceptor. This approach has less accuracy (fig. 30) and cannot distinguish between differently interacting donor species. However, it requires much fewer photons in the ROI (around 300-1000), which gives the opportunity to monitor very fast FRET processes in live cells in well-known systems.

Another method, which might be suitable for preliminary screening of FRET events, is the fitting of emission spectra (fig. 31), as it is fast and easy to perform and gives a good estimation of the FRET efficiency.

4.6 Model-free analysis of FRET-induced donor decays: fitting parameters and their physical interpretation

As discussed above, reduction of the donor lifetime in presence of the acceptor indicates FRET process, which might involve multiple components. A new approach introduced by (Peulen et al. 2017) helps to look more detailed at FRET. The fluorescence decay curve of the donor in presence of acceptor is divided by the donor-only curve and the resulting FRET-induced decay curve $\varepsilon_D(t)$ is fit with a double exponential function (fig. 32, 33). Obtained parameters provide information about the donor populations with hi- and low-FRET rates and about non-FRET donor species (fig. 34).

The single exponential fluorescence decay of the donor in absence of the acceptor can be described by the following equation:

$$f_D^{D0}(t) = \kappa_{F,D} e^{-\kappa_D t} \qquad \text{(Equation 36)}$$

Where $\kappa_{F,D}$ is the radiative rate constant of fluorescence of the donor; κ_D is the rate constant of deactivation of the excited donor state, which includes donor fluorescence (with $\kappa_{F,D}$ rate), internal conversion, quenching etc.

In the simplest case in presence of the acceptor the donor fluorescence decay stays monoexponential and involves all the donor molecules, then it can be described by the following equation:

$$f_D^{DA}(t) = \kappa_{F,D} e^{-(\kappa_{RET}+\kappa_D)t} \quad \text{(Equation 37)}$$

Where κ_{RET} is the FRET rate constant.

Next, we obtain the FRET-induced donor decay $\varepsilon_D(t)$ by division of the donor curve in presence of the acceptor by the donor-only curve:

$$\varepsilon_D(t) = \frac{f_D^{DA}}{f_D^{D0}} = \frac{e^{-(\kappa_{RET}+\kappa_D)t}}{e^{-\kappa_D t}} = e^{-\kappa_{RET} t} \quad \text{(Equation 38)}$$

Thus, an advantage of this approach is a direct visualization of the FRET rate constant.

In a more advanced example there are the FRET-inactive species present in the donor population (in case of fusion constructs it can happen due to acceptor being in a dark state), they can be directly seen as a constant offset – fraction a_{noFRET}, which we also call y_0:

$$f_D^{DA}(t) = \kappa_{F,D}[(1 - a_{noFRET})e^{-(\kappa_{RET}+\kappa_D)t} + a_{noFRET} e^{-\kappa_D t}] \quad \text{(Equation 39)}$$

$$\varepsilon_D(t) = (1 - a_{noFRET})e^{-\kappa_{RET} t} + a_{noFRET} \quad \text{(Equation 40)}$$

Finally, it is possible, that the donor molecules at a given time point of measurement represent a mixture of N donor populations interacting with the acceptors with different FRET rates κ^i_{RET} in amount of corresponding fractions a^i_{RET}. In this case the final $\varepsilon_D(t)$ is characterized as a fraction weighted sum of individual FRET-induced donor decays:

$$\varepsilon_D(t) = \sum_{i=1}^{N} a^i_{RET} e^{-\kappa^i_{RET} t} = \sum_{i=1}^{N} a^i_{RET} \varepsilon^i_D(t) \quad \text{(Equation 41)}$$

It can be seen, that this method takes into consideration the donor properties both in presence and absence of the acceptor. The standard fitting approach of the donor fluorescence decay curves with exponential functions might be advanced by application the global fitting approach, when the donor curves in presence and absence of the acceptor are fitted simultaneously. However, it requires choice of an appropriate model beforehand, namely amount of exponential components, which would influence the resulting FRET efficiencies.

4.6.1 Graphical analysis reveals best and worst FRET pairs

For all the fusion pairs we tested we had $N = 2$ donor populations: one with a hi-FRET rate, another with a low-FRET rate (fig. 34). The first population showed the FRET efficiency above 80%, the second one was in a range 20-50%. Such a consistency could be explained by the presence of a preferred orientation of the fusion construct, which showed a higher FRET efficiency. This further demonstrates, that despite the flexibility of the linker the tandem constructs are not oriented randomly (and the actual κ^2 is not 2/3).

The control construct mNeon-mNeon didn't show any FRET-induced donor decay, remaining at almost 1. It proves, that this method reflects processes, happening due to FRET.

Plotting of the FRET efficiencies E_A and E_B against corresponding fractions a_A and a_B demonstrates the importance of the acceptor properties, because the tandem constructs to a large extent group according to the acceptors they have (fig. 34, panel A). YPet acceptor showed the best acceptor properties: when it was present, the hi-FRET population a_A had the highest fraction (above 47%) and the non-interacting donor fraction y_0 was the lowest (less than 18%). These parameters were extreme for the mTurquoise2-YPet construct: a_A reached 67.4% and y_0 was 4.5%, which makes mTurquoise2 / YPet the most promising FRET pair among the tested ones. Venus and its derivative Venus(L68V) are the second best acceptors with slightly less a_A (24-42%) and a slightly larger y_0 (8-33%). They perform the worst in a pair with mTurquoise2, which means that outstanding performance of a donor protein in a pair with one partner doesn't guarantee, that it would be as good in a pair with a different acceptor when comparing to other donors.

The worst acceptor properties were demonstrated by the red and orange fluorescent proteins, namely mRFP, TagRFP, mCherry2, mRuby2, mRuby3 and mOrange2. They had both low fractions of hi-FRET rate populations (11-20%) and high non-FRET fractions (31-61%). This can be explained by a larger portion of red proteins being in a dark state in comparison to the green proteins and their derivatives. The non-FRET fraction is in consistency with the literature data. For example, as mentioned in section 4.1, around 46% of mRFP molecules is in a dark state, which is similar to such y_0 values as 38.7% in case of mNeon-mRFP and 44.4% for mEGFP-mRFP.

4.6.2 Interacting fractions in HEK293T cells change upon emetine treatment

Model-free graphical analysis (fig. 35) helps to understand better the differences seen previously (fig. 20) between proteins expressed in HEK293T cells and in neurons. FRET efficiencies of the hi- and low-FRET fractions don't differ in different cell types. What differs is the fractions of interacting and not interacting donors. Initially HEK293T cells have a lower interacting and higher non-interacting fractions in comparison to primary neurons. Upon emetine treatment of HEK293T cells these fractions change until they reach levels detected in neurons. This observation supports the idea, that the HEK293T cells have a noticeable fraction of immature non-FRET proteins. Therefore, emetine treatment doesn't affect FRET between donors and acceptors itself (as E_A and E_B stay stable); instead it increases the fraction of interacting molecules by RNA and protein synthesis inhibition.

HEK293T cells expressing mNeon-TagRFP for 12 h have a much larger fraction of non-interacting donors y_0 in comparison to cells 24 h post-transfection. It indicates, that the relative fractions of mature and immature proteins differ depending on the expression duration: the shorter this time is, the larger is the immature protein fraction. This observation was already seen, when we compared (fig. 20) HEK293T cells (24 h expression) and primary neurons (at least 7 days of expression).

4.7 Donor and acceptor molecules do weakly interact

To verify the level of interaction between the individual FPs we used purified proteins for a better control of their concentration. Our collaborators in the working group of Prof. Dr. Matthias Geyer performed purification of mNeon, mRFP, mNeon-mRFP, mTurquoise2, YPet and mTurquoise2-YPet proteins. FPLC showed, that all these proteins, except for YPet, were monomers, as they were detected at the expected time according to their molecular masses (fig. 36). YPet appeared to be almost as heavy as mTurquoise2-YPet, indicating that most of its molecules tend to homodimerize.

This suggests, that the hi-FRET conformation of the fusion pairs is not due to dimerization of the constructs, but rather a specific conformation, which is made by the fusion protein itself.

To investigate the presence and strength of the interactions between individual donors and acceptors, we performed 2-photon FLIM experiments on the mixtures of purified FPs. We used donors in a 1 μM concentration: on one hand, it is a low concentration, which allows increasing of the acceptor concentration range being tested. On the other hand, the donor amount is high enough to get a clear signal in a 2-photon FLIM setup. Acceptors concentrations ranged between 1 μM and 300 μM. When both donor and acceptor have a small concentration in a solution, then a probability for the molecules to meet is too low and no interaction could be detected. When the acceptor concentration is raised, there is more chance for the donors to meet acceptors and it would be detected as a donor lifetime reduction.

In general mRFP had a low crosstalk when the donor lifetime is measured: it was on average not higher, than 7% (this value was estimated for mNeon-TagRFP fusion protein, which showed the strongest crosstalk). However, when we applied high mRFP concentration in this experiment, a strong crosstalk became clearly visible. There might be several reasons for that. Firstly, acceptors are slightly excited by the 2-photon laser along with the donor, and despite a nice separation of the emission spectra by the filters, a small

portion of red emission might reach the detector. Secondly, red fluorescent proteins are known to have green intermediate products during the chromophore maturation process, which sometimes get trapped (Wall et al. 2000; Yarbrough et al. 2001) and therefore seen in the green channel (more details about the maturation are in the Introduction, section 1.2.2). We performed the crosstalk correction and further worked with the resulting curves.

Acceptor crosstalk is not such a problem for mTurq2 / YPet pair, because YPet signal is filtered well enough, and the protein doesn't have cyan intermediates during maturation.

We could nicely see the interaction between the donors and the acceptors, which was getting stronger with the increase of the acceptor concentration. This effect was especially noticeable in case of mTurq2 + YPet experiments (fig. 37, 38). Probably it was not as clear for mNeon + mRFP due to the noise introduced by crosstalk correction. When the YPet amount was too low, as expected there was no interaction detected: model-free graphical analysis estimated the non-interacting y_0 fraction above 95%. The interaction becomes detectable when the acceptor concentration reaches around 50 μM, as the FRET-induced donor decay becomes clearly double exponential. This situation was achieved in case of mNeon + mRFP mixtures when the mRFP concentration was 100 μM. With the further increase of the YPet concentration we observed the decrease of y_0 fraction down to 51.9% and a simultaneous increase of the hi- and low-FRET interaction fractions (up to 28.0% and 20.1% respectively). The hi-FRET fraction reaches the same FRET efficiency as the ones observed for the fusion mTurq2-YPet protein, indicating that the linker in the tandem construct is flexible enough to allow the orientation optimal for FRET, which is also performed by the freely floating proteins.

Based on the fitting of non-interacting y_0 fraction values with the Hill function (fig. 39), we have estimated the dissociation constants K_D for the FP pairs. Interestingly, fitting showed, that for both mTurquoise2 + YPet and mNeon + mRFP the interaction stoichiometry was close to 1 indicating, that the heterodimerization involves only one molecule of each kind. This property might help to avoid occasional involvement of closely localized FPs, when two cellular proteins of interest are already interacting during PPI studies.

Resulting K_D was 269.0 ± 23.9 μM for mTurq2 + YPet: half of mTurq2 molecules should be involved in the interaction, when YPet is at the indicated concentration. This value is close to the maximal YPet concentration (300 μM) we used in our experiments. The hi-FRET rate interaction fraction (which apparently reflects optimal orientation of the proteins for FRET) for the 1 μM mTurq2 + 300 μM YPet reached around 39% of that

observed in case of the purified fusion mTurq2-YPet construct (which is representing FRET close to the maximal possible) and around 42% of that seen in case of mTurq2-YPet expressed in neurons (table 18), which is pretty close to the prediction. Presence of the linker, which does not allow mTurq2-YPet construct to separate, might be the reason of the increased hi-FRET rate population in comparison to the freely moving proteins. The low-FRET rate fractions apparently reflect a weak FRET, which takes place as soon as the acceptor concentration is high enough for some interaction, very fast it either gets lost (primarily in case of freely moving proteins) or turns into a stronger hi-FRET interaction (especially if they are fused with each other).

Table 18. *Fraction of different interaction levels between mTurquoise2 and YPet proteins, acquired by graphical analysis*

Fraction	1 μM mTurq2 + 300 μM YPet	1 μM mTurq2-YPet (purified)	mTurq2-YPet (neurons)
y_0 (non-FRET)	51.9%	21.6%	4.5%
a_A (hi-FRET)	28.0%	72.0%	67.4%
a_B (low-FRET)	20.1%	6.4%	28.1%

K_D value for mNeon + mRFP was estimated at the value of around 82.9 ± 29.6 μM, which is much lower, than for mTurq2 + YPet, predicting a stronger interaction. The model-free graphical analysis of 1 μM mNeon + 300 μM mRFP shows similar parameters as mNeon-mRFP tandem (table 19). This data should be treated with more caution, as the crosstalk correction must have introduced some noise in the subsequent calculations.

Table 19. *Fraction of different interaction levels between mNeon and mRFP proteins, acquired by graphical analysis*

Fraction	1 μM mNeon + 300 μM mRFP	1 μM mNeon-mRFP (purified)	mNeon-mRFP (neurons)
y_0 (non-FRET)	38.9%	46.6%	38.7%
a_A (hi-FRET)	20.1%	22.1%	18.5%
a_B (low-FRET)	41.0%	31.3%	42.8%

When the acceptor is present in a very large concentration in mixtures with the donor, FRET might take place as a result of an occasional close localization of the two FPs. We predicted how the interaction would look like, if it was the only situation, when FRET was possible and no physical interaction was happening between the FPs. Characteristic acceptor concentration needed to statistically place the acceptor within the R_0 distance from the donor is in the range of ~ $2*10^{21}$ M for both FRET pairs, which is much larger, than we have ever used. The resulting K_D values are 18.7 ± 1.1 mM for mTurq2 / YPet pair

and 44.6 ± 7.6 mM for mNeon / mRFP. These values are more than 70 times bigger, than the ones obtained from the measured data, which indicates that the observed interaction between freely moving donor and acceptor molecules happens indeed due to their weak physical interaction and is not purely an occasional noise resulting from high acceptor concentration.

Slight differences were observed for the purified FPs and the proteins expressed in neurons. Firstly, this was the case for the tandem pairs (tables 18, 19). The properties of the FPs, including their excitability, lifetime and others, depend on the environment (pH, viscosity, osmolarity and others). Some small differences were already noticeable when comparing maturation times and the distribution of donor lifetimes in HEK293T cells and in primary neurons (fig. 20, panel E). Difference in the environments provided by the laboratory buffer and intracellular cytoplasm might explain the observed differences in the performance of the FPs.

Secondly, there were differences seen for the donor + acceptor mixtures. mNeon and mRFP proteins coexpressed in primary neurons didn't show almost any interaction as expected from the data, obtained from the purified FPs (fig. 23), y_0 fraction was around 87%. However, mTurq2 + YPet, coexpressed in neurons, demonstrated a weak interaction. Along with a pretty low y_0 (40%) and a_A (24%) fractions, it had a relatively high a_B (36%) fraction, reflecting the low-FRET rate interaction happening when the proteins don't have an optimal orientation. There are several factors contributing to these differences observed for the purified and intracellular proteins. One important aspect is again the difference in the environment and its influence on the FP performance. Another factor derives from the fact that it is very difficult to control the expression levels of proteins in primary neurons and make them equal, leading to the situation that in some cells the acceptor amount would be larger, than the donor amount.

4.8 Crystal structure analysis helps to better understand FRET phenomenon of mTurquoise2-YPet pair

4.8.1 Hi-FRET rate of mTurquoise2-YPet is due to close proximity between FPs

As discussed previously (see section 4.4), hi-FRET rate population of tandem constructs reflects those molecules, which have the orientation most optimal for FRET. This favorable positioning might be achieved via a close proximity (in other words, small R_{DA} distance) and/or parallel alignment of the dipoles (increase of κ^2). To investigate the nature of the hi-FRET rate fraction in more detail, our collaborators from the laboratory of Prof.

Dr. Geyer crystallized mTurquoise2 and mTurquoise2-YPet proteins and performed X-Ray structure analysis, whereas we did 2-photon FLIM and 2-photon dichroism experiments. When crystalizing, the proteins are expected to take the most optimal orientation.

mTurq2 crystals have typically a needle-like shape and varied in length between samples, mTurq2-YPet crystals are often sheet-like and usually larger, than mTurq2 crystals.

X-Ray structure analysis of mTurq2-YPet crystals demonstrates, that the donor and the acceptor of the fusion pair are located extremely close to each other – at the distance of around 3.7 nm. However, the angle between the fluorophores θ_T is 59.9°, which is far from optimal (ideal would be parallel orientation 0° or 180°; FRET is absent when the angle is 90°). Together with the θ_A and θ_D angles, which equal 23.4° and 72.1° respectively, it results in a very low κ^2 of 0.12 (eq. 35, fig. 53). Förster Radius R_0, calculated from the equation 7, reaches 4.44 nm, leading to a predicted FRET efficiency in the crystals of 75.0% (eq. 5). This value is similar to the FRET efficiency, measured for mTurquoise2-YPet in primary neurons (72.3%). Hence, hi-FRET rate population of mTurquoise2-YPet molecules derives from the close proximity between the interacting donors and acceptors and contributes the most into the overall FRET efficiency. FRET efficiency is very high, despite not optimal angle between the interacting dipoles.

To verify the predicted FRET efficiency in crystals, we performed the 2-photon FLIM experiments (fig. 42). Lifetime of mTurq2 in the crystal didn't differ from its lifetime measured in primary neurons or in purified state. No lifetime change upon crystallization was also observed for other FPs (Royant et al. 2007). However, in case of mTurq2-YPet the donor lifetime was unexpectedly slow and monoexponential, FRET efficiency was around 22.0%. Possible explanation might be a new environment, affecting the fluorescent properties of the proteins. Indeed, the pH of the solution, in which the crystals were growing was around 6, which is not very critical for mTurquoise2 (as mentioned before, mTurq2 lifetime in crystals was almost not altered), but it might play a big role for YPet. It is known, that the yellow fluorescent protein YFP and (to a lesser extent) its derivatives are sensitive to a lower pH (Olenych et al. 2007). It means, that when the pH is decreased, YPet cannot be excited as effectively, which leads to a reduction of FRET. Mild treatment with NaOH increases the pH value to a more optimal of around 7.5. It leads to instability of the crystals and to their destruction, however the donor lifetime decreases drastically and becomes double exponential. FRET efficiency reaches 67.7% and therefore approaches the levels obtained in primary neurons and predicted for crystals. Model-free

graphical analysis demonstrates an extremely low non-interacting fraction of 1.7%. The hi-FRET rate fraction of 31.5% is pretty low and the low-FRET rate fraction of 66.9% is very high in comparison to the performance in other environments. It can be explained by a combination of different factors. Firstly, a big role might play instability of the crystal under the pH of 7.5. Secondly, low-FRET rate population in crystals might reflect FRET between unfused mTurq2 and YPet of neighboring tandem constructs; contribution of such interaction would be negligible when the fusion pairs are freely moving in the solutions.

4.8.2 mTurquoise2 proteins are aligned along the crystal axis

An indirect way of crystal structure characterization is based on the linear dichroism of FP crystals. It was shown previously, that the native GFP crystals are photoselective: when the crystal is parallel to the electric vector of the polarized excitation light, then it is very bright, whereas when the two are perpendicular, then the crystal is almost invisible. It indicates, that all the chromophores of native GFP are aligned parallel to the crystal long axis. Taking into account the X-ray crystallographic data, which shows, that the angle between the long axis of the FP cylinder and the fluorescent chromophore is around 60°, one can assume a schematic model of the crystals, shown in figure 54 (Inoue et al. 2002).

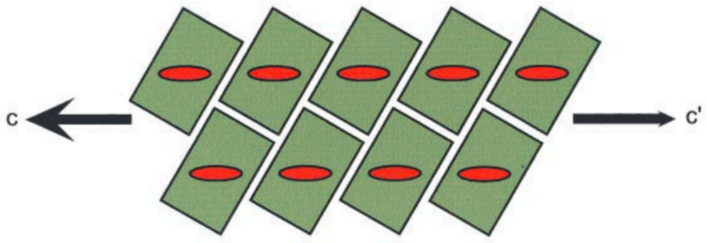

Figure 54. *Scheme of the native GFP crystal composition. Fluorescent chromophores (red ovals) inside the β-barrels (green rectangulars) are oriented parallel to the crystal long axis (shown with arrows). From (Inoue et al. 2002).*

We performed a similar experiment with the mTurq2-YPet crystals and observed photoselectivity as well. Fluorescence emission intensity *f* of both mTurquoise2 and YPet proteins within the fusion pair crystal is a function of an angle φ between the electric filed orientation of the polarized excitation light and the crystal long axis (fig. 46), and it can be fit with a $\cos^4\varphi$ function (Lakowicz 2006).

X-ray structure analysis showed the presence of two species of mTurquoise2 proteins and two species of YPet molecules within the mTurquoise2-YPet crystal. The species differ by orientation in space (table 16). Presence of two dipole species results in two members of sum when fitting the crystal fluorescence emission *f* with $\cos^4\varphi$ function:

$$f(\varphi) = a * cos^4\big(0.01745 * (\varphi - \varphi_0)\big) + a * cos^4(0.01745 * (\varphi - \varphi_0 - \varphi_1))$$

(Equation 25)

Where $\pi/180 = 0.01745$ is degree-to-radian converter, φ_0 is the angle between crystal axis and one of the dipole species, φ_1 is the angle between dipole species, φ_0 and φ_1 are angles on the projection of crystal tertiary structure to the planar imaging plane (fig. 55).

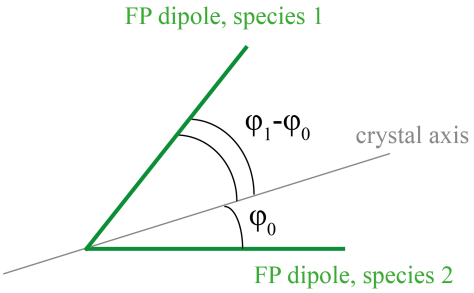

Figure 55. *Scheme representing the projected orientations of two fluorescent protein dipole species and the crystal axis to the field of view. Angle between two projected dipole species is φ_1; angle between the dipole species and the crystal axis are φ_0 and $(\varphi_1 - \varphi_0)$.*

Unfortunately, we don't know from the X-ray analysis how the crystal axis is oriented relative to the dipole species, but crystal dichroism experiments might give a hint to find it out. The strongest mTurquoise2 fluorescence emission of the crystal is observed, when the electric field of the 2-photon laser excitation light is parallel to the crystal axis ($\varphi = 0°$), as seen in fig. 46 panel D. This data suggests, that the crystal axis is aligned with the mTurquoise2 dipoles and cuts the angle between the dipole species in half (when looking at the projections to the imaging plane). Fitting of all measured crystals (eq. 25) allows estimating mean ± SEM projection angle φ_1 around 48.6 ± 1.6°, which is close to the angle between the two dipole species 53.4° calculated from the X-ray structure analysis. Projection angle φ_0 has a small variability across different crystals and lays around 24.1 ± 1.5°, hence crystal axis cuts the projected angle between species φ_1 in halves. A predicted mTurquoise2 intensity curve for equation 25 using the averaged φ_0 and φ_1 values is shown in fig. 56 panel A, its peak is around $\varphi = 0°$, as for the measured data.

In case of YPet fluorescence emission curve, its peak may be located at any φ (fig. 4.5K panel E). This means, that YPet dipoles are not parallel to the crystal axis and therefore are not parallel to mTurquoise2 dipoles, which is an indirect indication, that κ^2 cannot reach maximal value in the crystal.

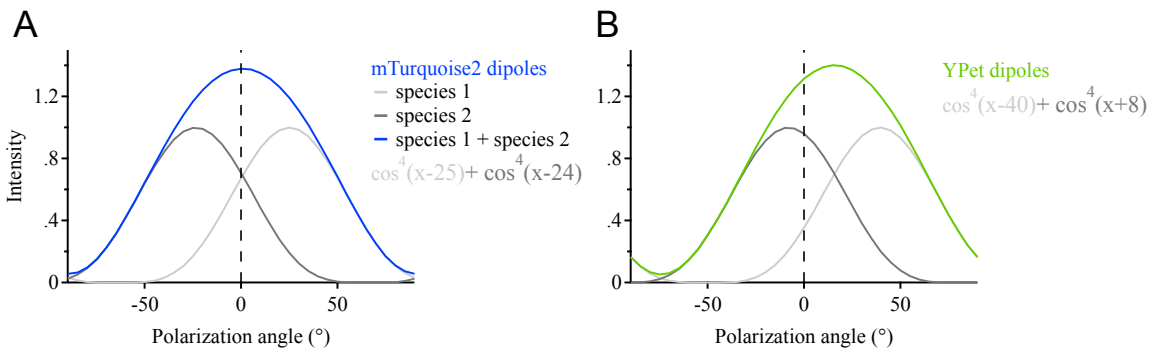

Figure 56. *Predicted fluorescence intensity as a cos^4 function of the angle φ between the electric field orientation of the excitation light and the crystal axis. Predicted curves are estimated using the average φ_0 and φ_1 values, obtained during the fitting (eq. 25) of the measured curves. Fluorescence intensity is shown for the two dipole species independently (gray) and for their sum (blue curve for mTurquoise2 (A) and green curve for YPet (B)) within the mTurquoise2-YPet crystals. Amplitudes are set at 1.*

Fitting of the measured YPet intensity curves using the equation 25 results in the average projection φ_1 of around 47.6 ± 1.4°, which is close to the angle 52.8° estimated from the x-ray data. The projection angle φ_0 varies a lot in the range 39.5 ± 6.2°, indicating, that, unlike mTurquoise2, YPet dipoles projected to the imaging plane are not symmetrically located relatively to the projected crystal axis (fig. 56 panel B). Therefore, the actual YPet chromophores are also not symmetric regarding the crystal axis in the three-dimensional crystal structure. Due to this asymmetry, the YPet dipole direction depends on the rotation of the crystal along its long axis, which leads to a diversity between crystals regarding the angle φ, at which maximal fluorescence intensity is reached.

4.9 mTurquoise2 / YPet FRET pair is applicable for PPI studies

A flexible linker between two proteins helps them to fold correctly and to fulfill their functions independently of each other. When the FP is fused to a different protein via the linker, its fluorescent properties are not affected. It was observed for mNeon-mNeon (fig. 23) and for the fusion with presynaptic protein (fig. 51 panel E). When the presynaptic protein is fused to the FP, its localization stays unaltered (fig. 50), indicating that the function probably is also unaffected.

We chose Synaptophysin1 (Syph1) and Synaptobrevin2 (Syb2) presynaptic proteins to test the applicability of mTurq2 / YPet FRET pair (fig. 51). Syb2 is a SNARE protein crucial for neurotransmitter release and is known to interact with another vesicular protein Syph1. Syb2 and Syph1 are the most abundant proteins on vesicles (Gordon & Cousin

2013). Apparently, Syph1 is important for the clearance of Syb2 from the active zone (Rajappa et al. 2016), however, still little is known about the interaction between these proteins, which makes them a potentially interesting object of research.

We could detect the interaction between Syph1 and Syb2 in 2-photon FLIM experiments in primary cultures. Phasor plot provides a quick overview of this interaction (fig. 52). After performing the graphical analysis (fig. 51) we observed the hi-FRET rate population with a similar FRET efficiency as in case of Syph1-mTurq2-YPet indicating, that during the interaction of Syph1 and Syb2 the FPs attached to them come close enough to each other to interact in an optimal way. The fraction of this interaction (11.5%) is pretty low as expected, because not all presynaptic proteins interact with each other.

A control experiment involving coexpression of Syph1 and Vglut1 fused to the FPs confirms the lack of interaction between these vesicular presynaptic proteins both in high level of y_0 (78.9%) and low FRET efficiency (0%) estimated after the graphical analysis.

This experiment demonstrates, that mTurq2 / YPet pair along with the model-free graphical analysis is nicely applicable in PPI studies.

No observed difference of the FP performance in primary neuronal cultures and in native neurons in acute mouse brain slices proves, that this FRET pair could also be used *in vivo* experiments.

4.10 Outlook

In this study we identified mTurquoise2 / YPet as a pair with outstanding FRET properties. Extremely high FRET efficiency demonstrated is due to an optimal orientation between the donor and the acceptor, which leads to a very close proximity between them. How exactly is this orientation reached? Further structural analysis of the crystalized proteins should show, which amino acids exactly are responsible for the interaction between the FPs. Are these amino acids also present in other fluorescent proteins? Would their introduction improve the performance of other cyan / yellow FRET pairs?

Why does the purified YPet protein dimerize? Which amino acids are involved in this process? Could it lead to a competition between YPet dimerization and mTurq2 / YPet interaction?

Which exactly properties of the environment affect the performance of the FPs and FRET between them?

mTurq2 / YPet FRET pair should be further applied for PPI experiments and in biosensors.

It could be used in a Camuiα sensor, which is a reporter of CamKII activity and is often applied to study long-term potentiation and cardiomyocyte contraction (Bossuyt & Bers 2013; K. Kim & Hayashi 2014). Mostly pairs of green / red or green / dim (not fluorescent) proteins are used in this biosensor nowadays, for example mEGFP / REACh (Lee et al. 2009), mEGFP / dimVenus (Otmakhov et al. 2015; Laviv et al. 2016), mEGFP / mCherry (Shibata et al. 2015). CFP / YFP pairs and their derivatives are rarely used for this sensor (Erickson et al. 2011), therefore mTurq2 / YPet could be a nice candidate for this purpose. A variety of color combinations available is an advantage, if the sensor application has to be combined with other techniques requiring fluorescence imaging.

Sensors of cAMP-dependent protein kinase (PKA) activity (Patel & Gold 2015) (such as AKARs, Epacs) are accessible in green / red variants as well, for example AKAR5 (with EGFP / sREACh (Ma et al. 2018)) or AKAR-CR (with mClover / mRuby2 (Lam et al. 2012)). However, in contrast to Camuiα, PKA sensors usually involve cyan / yellow FRET pairs, namely Cerulean / cpVenus (AKAR4 (Depry et al. 2011)), mTurq / Venus or cpVenus (AKAR3.2 (Chen et al. 2014), $^{T}Epac^{VV}$ (Klarenbeek et al. 2011)) and others. It would be interesting to compare mTurq2 / YPet performance with the established AKAR and Epac sensors.

Finally, mTurq2 / YPet pair could be applied for the interaction studies between cellular proteins or between the domains of cellular proteins. For example, FRET-FLIM approach is nicely suitable for investigation of dynamic interactions of presynaptic proteins in neurons, such as SNARE proteins (Degtyar et al. 2013; Takahashi et al. 1AD), RIM1 with Munc13, Rab3, Syt1, Syt7 and so on.

As the close proximity is crucial for FRET-based methods, it might be sometimes useful to investigate interactions between certain domains, if the full proteins are too long. As an example, this method was used to study PKA activity, when only the RII subunit was used (Efendiev et al. 2010).

5 Summary

Monitoring Förster Resonance Energy Transfer (FRET) between fluorescent proteins (FPs) fused to proteins of interest is a powerful approach to study dynamic interactions of cellular proteins in living cells. The choice of an appropriate FRET pair is still a challenging topic despite a large palette of existing FPs, where fluorescent properties of individual proteins, FRET properties of pairs and conformation of interacting constructs play a role.

Here we compared FRET performance of 19 green / green and cyan / yellow pairs in identical conditions, FPs were fused via a short and flexible linker SRG_4SG_4S and tested using a two-photon FRET-FLIM (fluorescence lifetime imaging microscopy) technique. Fast growing cells like HEK293T were not suitable for experiments involving FRET, because their rapid division and strong protein overproduction led to a significant fraction of immature red acceptors and therefore strong underestimation of FRET efficiency. This effect was not present when performing experiments in transduced primary neurons on DIV 13-17.

Most FRET donors displayed single exponential fluorescence decays in absence of acceptors, except for mCerulean. When fused to the acceptors, donor decays became double exponential. FRET efficiency was estimated as the reduction of the donor lifetime in presence of the acceptor. It ranged between 39% and 72% among the tested pairs, reaching the highest values of 39% in case of mNeon-mRFP and mNeon-mCherry2 and 72% in case of mTurquoise2-YPet among green / red and cyan / yellow pairs, respectively. These strong performances were confirmed in native neurons of hippocampal mouse brain slices after viral injections *in vivo*.

Model-free graphical analysis showed presence of three fractions of molecules: with hi-FRET rate (~2.2 ns^{-1}), with low-FRET rate (~0.2 ns^{-1}) predicted by random orientation and non-FRET state consistent with immature and dark acceptors and unfavourable orientation. Fractions of these populations defined the overall FRET efficiency and were primarily determined by the FRET acceptor. YPet had the largest hi-FRET population and the lowest non-interacting fraction. Red acceptors showed the worst performance due to their slow maturation and high dark state fraction.

Furthermore, structural analysis of purified and crystallized mTurquoise2-YPet fusion protein demonstrated, that the nature of hi-FRET rate derived from close association of donor and acceptor FPs leading to a domination of high FRET efficiency conformation.

Finally, fluorescent properties and FRET efficiencies were proved to be unaffected after targeting of the FPs to the presynaptic compartment by their fusion with vesicular proteins Synaptophysin1 and Synaptobrevin2. Interaction between these presynaptic proteins was detected in primary neurons.

Overall, this work demonstrates and explains an outstanding FRET performance of mTurquoise2 / YPet FPs among the tested pairs and their applicability for the protein-protein interaction (PPI) studies using the two-photon FRET-FLIM approach in neurons. Our findings form the basis for further PPIs researches using the new pair with high FRET efficiency, as well as for the development and evolution of FRET-based sensors and reporters with high FRET efficiencies and large dynamic ranges.

6 Appendix: Materials

6.1 Equipment

Equipment	Model	Company	Country
2-photon Microscope Setup	SliceScope	Scientifica	Uckfield, UK
2-photon Microscope Setup	Ultima Multiphoton	Prairie Technologies	Bruker, USA
2-photon Imaging Laser		Coherent	Santa Clara, USA
Agarose electrophoresis system	Sub-Cell GT	BioRad	Hercules, USA
Analytical Balance		VWR	Radnor, USA
Autoclave	Laboclav	Steriltechnik AK	Hückeswagen Germany
Balance	EG420-3NM	Kern EG	Balinaen, Germany
Cell-culture hood	MSC-Advantage	Thermo Scientific	Waltham, USA
Cell-culture hood	HERA Safe KS	Thermo Scientific	Waltham, USA
Cell-culture incubator	HERA Cell 150i	Thermo Scientific	Waltham, USA
Centrifuge	Rotina 420R	Hettich	Kirchlengern, Germany
Centrifuge	Mikro 200	Hettich	Kirchlengern, Germany
Confocal laser scanning microscope	A1/Ti	Nikon	Tokyo, Japan
Controller	Micro4 Controller, 4-channel	World Precision Instruments	Sarasota, USA
Filters and filter cubes	table 10	AHF	Tübingen, Germany
Incubator		Binder	Tuttlingen, Germany
Inverse microscope	Axio Observer A1	Zeiss	Oberkochen, Germany
Lifetime detector	Simple-Tau SPC-150	Becker and Hickl	Berlin, Germany
MiliQ-Ultra pure water	Advantage A10	Millipore	Burlington, USA
Microsyringe pump controller	Micro4	World precision instruments	Sarasota, USA
PCR machine	MY Cycler	BioRad	Hercules, USA
PCR machine	T300	Biometra	Göttingen, Germany
Peristaltic Pump	P-1	GE Healthcare	Chicago, USA
pH-Meter	SevenCompact	Mettler Toledo	Columbus, USA
Power Supply	Power Pack Basic	Biorad	Hercules, USA
Shaker	Polymax 1040	Heidolph	Schwabach, Germany
Sonicator	Labsonic 2000	B. Braun	Melsungen, Germany
Spectrofluorometer	PTI QuantaMaster400	Horiba Scientific	Kyoto, Japan
Spectrophotometer	Nanodrop 2000	Thermo Scientific	Waltham, USA
Syringe	Nanofil	World Precision Instruments	Sarasota, USA
Thermo Shaker	Compact	Eppendorf	Hamburg, Germany
Thermo Shaker	MB-102	Bioer	Hangzhou, China
Thermo Shaker	MKR13	HLC	Noida, India
Vibratome	VT1200S	Leica	Wetzlar, Germany
Vortexer	Vortex-Genie 2	Scientific Industries	New York, USA

6.2 Chemicals

Chemical	Company	Country
5x HF Buffer	Thermo Scientific	Waltham, USA
6x loading buffer	Thermo Scientific	Waltham, USA
10x ligation buffer	Thermo Scientific	Waltham, USA
10x *pfu* Buffer with $MgSO_4$	Thermo Scientific	Waltham, USA
10x restriction buffers G, O, R, Tango	Thermo Scientific	Waltham, USA
Agarose	Biozym	Hessisch Oldendorf, Germany
Ampicillin	Carl Roth	Karlsruhe, Germany
Ampuwa water	Fresenius Kabi	Bad Homburg, Germany

Bovine Serum Albumin (BSA), fraction V	Carl Roth	Karlsruhe, Germany
Calcium chloride ($CaCl_2$)	Sigma-Aldrich	St. Louis, USA
Chloroform	Carl Roth	Karlsruhe, Germany
Chlorhidric acid (HCl)	Carl Roth	Karlsruhe, Germany
Dimethylsulfoxide (DMSO)	Thermo Scientific	Waltham, USA
dATP	Thermo Scientific	Waltham, USA
dCTP	Thermo Scientific	Waltham, USA
dGTP	Thermo Scientific	Waltham, USA
Emetine dihydrochloride hydrate	Sigma-Aldrich	St. Louis, USA
Ethanol (EtOH)	Carl Roth	Karlsruhe, Germany
GeneRuler 1 kb	Thermo Scientific	Waltham, USA
Glucose	PanReac AppliChem	Darmstadt, Germany
HEPES	Carl Roth	Karlsruhe, Germany
Isoflurane	Piramal Healthcare	Mumbai, India
Isopropanol	Carl Roth	Karlsruhe, Germany
Kanamycin	Sigma-Aldrich	St. Louis, USA
Ketamine	WDT	Garbsen, Germany
Luria Broth-Agar (Luria-Miller)	Carl Roth	Karlsruhe, Germany
Luria Broth-Medium (Luria-Miller)	Carl Roth	Karlsruhe, Germany
Magnesium Chloride $MgCl_2$	PanReac AppliChem	Darmstadt, Germany
Mowiol 4-88	Carl Roth	Karlsruhe, Germany
Normal goat serum (NGS)	Life Technologies	Waltham, USA
Paraformaldehyde	Sigma-Aldrich	St. Louis, USA
PeqGreen DNA/RNA Dye	VWR	Radnor, USA
Phenol chlorophorm	Carl Roth	Karlsruhe, Germany
Phosphate buffered saline (PBS)	Millipore	Burlington, USA
Polyethylenimine (PEI)	Polysciences	Warrington, USA
Poly-D-lysine	Sigma-Aldrich	St. Louis, USA
Potassium chloride (KCl)	Carl Roth	Karlsruhe, Germany
SOC Medium	Takara	Kyoto, Japan
Sodium acetate (NaOAc)	Carl Roth	Karlsruhe, Germany
Sodium Carbonate ($NaHCO_3$)	PanReac AppliChem	Darmstadt, Germany
Sodium hydroxide (NaOH)	Carl Roth	Karlsruhe, Germany
Sodium chloride (NaCl)	Carl Roth	Karlsruhe, Germany
Sodium phosphate (Na_2HPO_4)	Sigma-Aldrich	St. Louis, USA
Sodium phosphate (NaH_2PO_4)	G-Biosciences	St. Louis, USA
Sucrose	PanReac AppliChem	Darmstadt, Germany
Triton-X100	Sigma-Aldrich	St. Louis, USA
Tris	Carl Roth	Karlsruhe, Germany
TTP	Thermo Scientific	Waltham, USA
Xylazine	Ceva Tiergesundheit	Düsseldorf, Germany

6.3 Cell culture media and reagents

Cell culture medium	Company	Country
Basal Medium Eagle (BME)	Life Technologies	Waltham, USA
Dulbecco's Modified Eagle Medium (DMEM)		
Dulbecco's Phosphate Buffered Saline (DPBS)		
Iscove's Modified Dulbecco's Medium (IMDM)		
Fetal bovine/calf serum (FBS/FCS)		
Neurobasal Medium (NB+)		
Penicillin-Streptomycin		
0.05% Trypsin-EDTA		

6.4 Antibodies

6.4.1 Primary antibodies

Antibody	Assay	Dilution	Company	Country
Mouse anti-Vamp2 (*104211*)	IC	1:1000	Synaptic systems	Göttingen, Germany
Rabbit anti-Syph1 (*ab52636*)	IC	1:1000	Abcam	Cambridge, UK

6.4.2 Secondary antibodies

Antibody	Assay	Dilution	Company	Country
Alexa405 Fluor goat anti-mouse	IC	1:200	Life technologies	Waltham, USA
Alexa405 Fluor goat anti-rabbit	IC	1:200		

6.5 Enzymes

Enzyme	Company	Country
In-fusion cloning enzyme	Takara	Kyoto, Japan
pfu DNA polymerase	Thermo Scientific	Waltham, USA
Phusion DNA polymerase		
Restriction enzymes: *BamHI, EcoRI, HindIII, SalI, XbaI*		
Shrimp alkaline phosphatase		
T4 DNA ligase		
T4 polynucleotide kinase		

6.6 Kits

Kit	Company	Country
DNA Clean and Concentrator kit	Zymo Research	Irvine, USA
EndoFree Plasmid Maxi kit	Qiagen	Venlo, Netherlands
Gel DNA recovery kit	Zymo Research	Irvine, USA
GenJET Plasmid Miniprep kit	Thermo Scientific	Waltham, USA
In-fusion Cloning kit	Takara	Kyoto, Japan
NucleoSpin Gel and PCR Clean-up kit	Macherey-Nagel	Düren, Germany
PureLink HiPure Plasmid Filter Maxiprep kit	Thermo Scientific	Waltham, USA
PureLink HiPure Plasmid Filter Midiprep kit	Thermo Scientific	Waltham, USA

6.7 Other materials

Product	Company	Country
15 ml falcon	Greiner Bio-One	Frickenhausen, Germany
24-well plate	VWR	Radnor, USA
50 ml falcon	Greiner Bio-One	Frickenhausen, Germany
100x20 mm dishes	Greiner Bio-One	Frickenhausen, Germany
Amicon Ultra Centrifugal filters	Milipore	Burlington, USA
Cell culture flask	Greiner Bio-One	Frickenhausen, Germany
Coverslips	Hecht	Sondheim, Germany
Filter pipette tips 10 µl, 200 µl, 1000 µl	Nerbe Plus	Winsen, Germany
35 mm µ-dish	Ibidi	Planegg, Germany
Reaction tubes	Greiner Bio-One	Frickenhausen, Germany
Syringe filter 0.2 µm cellulose acetate	VWR	Radnor, USA
Pipette tips 10 µl, 200 µl, 1000 µl	Greiner Bio-One	Frickenhausen, Germany

6.8 DNA

6.8.1 Cloning primers

All the oligonucleotides were synthesized either by Invitrogen (Waltham, USA) or by Ella Biotech (Martinsried, Germany).

Gene	Direction	Internal lab #	Primer 5'-3' sequence	En-zyme
Fluorescent protein pairs for FRET estimation				
mNeon, mEGFP, mTFP1	Fw	c918	gcggaattcatggtgagcaagggcgaggag	EcoRI
	Rev	c919	gcgtctagacttgtacagctcgtccatgcc	XbaI
	Fw	c988	gcgggatccatggtgagcaagggcgaggag	BamHI
	Rev	c1103	gcgaagctttacttgtacagctcgtccatgcc	HindIII
mClover	Fw	c1106	gcggaattcggcatggtgagcaagg	EcoRI
	Rev	c1107	gcgtctagacttgtacagctcgtccatgccat	XbaI
mClover3	Fw	c1793	gcggaattcatggtgagcaagggcgaggagctgttc	EcoRI
	Rev	c1794	gcgtctagaggcggcggtcacgaactccag	XbaI
mRFP	Fw	c922	gcgggatccatggcctcctccgaggacgtcatcaa	BamHI
	Rev	c923	gcgaagcttctaggcgccggtggagtggc	HindIII
TagRFP	Fw	c920	gcgggatccatggtgtctaagggcgaag	BamHI
	Rev	c921	gcgaagcttctaattaagtttgtgccccagtttgc	HindIII
	Fw	c1097	gcggaattcatggtgtctaagggcgaag	EcoRI
	Rev	c1098	gcgtctagaattaagtttgtgccccagtttgc	XbaI
mCherry2	Fw	c1429	gcgggatccatggtgagcaagggcgagg	BamHI
	Rev	c1430	gcgaagcttttacttgtacagctcgtccatgccg	HindIII
mRuby2, mRuby3	Fw	c1108	gcgggatccatggtgtctaagggcgaag	BamHI
mRuby2	Rev	c1109	gcgaagctttacttgtacagctcgtccatcc	HindIII
mRuby3	Rev	c1795	gcgaagctttacttgtacagctcgtccatg	HindIII
mCer, mTurq2, mTFP1	Fw	c1159	gcggaattcgccaccatggtgagcaagggcgaggag	EcoRI
mCer	Rev	c1160	gcgtctagacttgtacagctcgtccatgccgagagtg	XbaI
mTurq2	Rev	c1400	gcgtctagacttgtacagctcgtccatgccgagagtg	XbaI
YPet	Fw	c1112	gcgggatccatggtgagcaaaggcgaagagc	BamHI
	Rev	c1158	gcgaagctttacttatagagctcgttcatgccctcgg	HindIII
Venus, Venus(L68V)	Fw	c1170	cgcggatccgtgagcaagggcgaggagctgttcaccggg	BamHI
	Rev	c1171	gcgaagcttgtaccgtcgactgcagaactacttgtacagctcgtccatgccg	HindIII
mOrange2	Fw	c1431	gcgggatccatggtgagcaagggcgaggagaa	BamHI
	Rev	c1116	gcgaagctttacttgtacagctcgtccatgccg	HindIII
Protein-protein interactions (in-Fusion cloning)				
Syph1	Fw	c1677	aattccccggggatccatggacgtggtg	
	Rev	c1678	cgccgccgcttccaccgccgccctgattggagaaggaggtgggcs	
mNeon, mTurq2	Fw	c1679	gtggaagcggcggcggtggaagcatggtgagcaagggcgag	
	Rev	c1680	gcttctgcaggtcgacctaggatcctccacctccagac	
	Fw	c1759	ggcggcggaggatcaggcggcggcggctcggtgagcaagggcgagg	
	Rev	c1760	tgctcgaggcaagcttctacttgtacagctcgtccatgc	
mRFP	Rev	c1681	gcttctgcaggtcgactaggcgccggtgg	
	Fw	c1747	aattccccggggatccatggcctcctccgagg	
	Rev	c1683	cgccgccgcttccaccgccgccggcgccggtggagt	
YPet	Rev	c1957	tgctcgaggcaagctaagcttttacttatagagctcgt	
	Fw	c1918	aattccccggggatccatggtgagcaaa	
	Rev	c1158	gcgaagcttttacttatagagctcgttcatgccctcgg	
Syb2	Fw	c1684	gtggaagcggcggcggtggaagcatgtcggctaccgctgc	
	Rev	c1606	tgctcgaggcaagcttttaagtgctgaagtaaacgatgatgatgatgag	

Vglut1	Fw	c1809	ccggggatcctctagaatggagttccggcaggagg
	Rev	c1810	gccgccgcctgatcctccgccgcctctcgagtagtcccggacaggggg

6.8.2 Sequencing primers

Vector	Direction	Internal lab #	Primer 5'-3' sequence
pAAV-CMV	Fw	s109	gattattctgagtccaagctagg
	Rev	s184	ttgccccttgctccatac

6.8.3 Oligonucleotides used for cloning

Name	Strand	Internal lab #	Primer 5'-3' sequence	Enzyme
linker	upper	c955	ctagaggaggaggtgggtctggaggtgga**ggatcc**taga	XbaI, BamHI, HindIII
	lower	c956	agcttcta**ggatcc**tccacctccagacccacctcctcct	XbaI, BamHI, HindIII

6.8.4 Generated constructs

For all the generated constructs AAV-CMV-MCS plasmid (section 6.8.5) was used as a vector. Templates for cloning of the genes are listed in section 6.8.5.

Name	Inserted genes
AAV-mNeon-linker	mNeonGreen
AAV-mNeon-linker-mRFP	mNeonGreen, mRFP
AAV-mNeon-linker-TagRFP	mNeonGreen, TagRFP
AAV-mNeon-linker-mCherry2	mNeonGreen, mCherry2
AAV-mNeon-linker-mRuby3	mNeonGreen, mRuby3
AAV-mNeon-linker-mNeon	mNeonGreen
AAV-TagRFP-linker-mNeon	mNeonGreen, TagRFP
AAV-mEGFP-linker	mEGFP
AAV-mEGFP-linker-mRFP	mEGFP, mRFP
AAV-mEGFP-linker-TagRFP	mEGFP, TagRFP
AAV-mEGFP-linker-mCherry2	mEGFP, mCherry2
AAV-mClover-linker	mClover
AAV-mClover-linker-mRuby2	mClover, mRuby2
AAV-mClover3-linker	mClover3
AAV-mClover3-linker-mRuby3	mClover3, mRuby3
AAV-mCer-linker	mCerulean
AAV-mCer-linker-YPet	mCerulean, YPet
AAV-mCer-linker-Venus	mCerulean, Venus
AAV-mTurq2-linker	mTurquoise2
AAV-mTurq2-linker-YPet	mTurquoise2, YPet
AAV-mTurq2-linker-Venus(L68V)	mTurquoise2, Venus(L68V)
AAV-mTurq2-linker-mOrange2	mTurquoise2, mOrange2
AAV-mTurq2-linker-mNeon	mTurquoise2, mNeonGreen
AAV-mTFP1-linker	mTFP1
AAV-mTFP1-linker-YPet	mTFP1, YPet
AAV-mTFP1-linker-Venus(L68V)	mTFP1, Venus(L68V)
AAV-mTFP1-linker-mOrange2	mTFP1, mOrange2
AAV-mRFP	mRFP
AAV-TagRFP	TagRFP
AAV-mCherry2	mCherry2
AAV-mRuby2	mRuby2
AAV-mRuby3	mRuby3

AAV-YPet	YPet
AAV-Venus	Venus
AAV-Venus(L68V)	Venus(L68V)
AAV-mOrange2	mOrange2
AAV-Syph1-linker-mNeon	Synaptophysin1, mNeonGreen
AAV-Syph1-linker-mNeon-linker-mRFP	Synaptophysin1, mNeonGreen, mRFP
AAV-Syph1-linker-mTurq2	Synaptophysin1, mTurquoise2
AAV-Syph1-linker-mTurq2-linker-YPet	Synaptophysin1, mTurquoise2, YPet
AAV-mRFP-linker-Syb2	Synaptobrevin2 (=Vamp2), mRFP
AAV-YPet-linker-Syb2	Synaptobrevin2 (=Vamp2), YPet
AAV-Vglut1-linker-mNeon	Vglut1, mNeonGreen
AAV-Vglut1-linker-mTurq2	Vglut1, mTurquoise2

6.8.5 Plasmids, provided by other sources

Plasmid name	Source	Addgene #	Country or lab
pAAV-CMV-MCS	Stratagene		La Jolla, USA
pEGFP-N2	Clontech		Mountain View, USA
pNCS-mNeonGreen	Allele Biotechnology		San Diego, USA
CMV:ratSyGCaMP2 (Syph1 gene)	Addgene (Cambridge, USA)	26124	L. Lagnado (Dreosti et al. 2009)
C5V (mCer-Venus)		26394	S. Vogel (Koushik et al. 2006)
Cdk1 FRET sensor (mCer-YPet)		26064	J. Pines (Gavet & Pines 2010)
mCherry2-N1		54517	M. Davidson
mOrange-C1		54650	M. Davidson, R. Tsien (Shaner et al. 2008)
mRFP-N1		54635	R. Campbell, M. Davidson, R. Tsien (Campbell et al. 2002)
mTFP1-N1		54521	R. Campbell, M. Davidson (Ai et al. 2006; Ai et al. 2008)
pcDNA3.1-Clover-mRuby2		49089	K. Beam
pKan-CMV-mClover3-mRuby3		74252	M. Lin (Bajar, E. S. Wang, et al. 2016)
pmVenus(L68V)-mTurquoise2		60493	D. Gadella (Goedhart et al. 2012)
pRSI9-U6-(sh)-UbiC-TagRFP-2A-Puro		28289	A. Chenchik, G. Frangou

6.9 Cells and animals

Cell or animal line	Company	Company
E. coli DH5α	Thermofisher Scientific	Waltham, USA
Stellar competent cells	Takara	Kyoto, Japan
HEK293T cells	Agilent Technologies	Santa Clara, USA
wt C57/BL6 mice	Charles River	Wilmington, USA

6.10 Programms and URLs

ImageJ (NIH, Bethesda, USA)

Igor Pro 7 (WaveMetrics, Portland, USA)

PyMOL (Schrödinger Inc., New York, USA)

SnapGene v.2.3.5 (GSL Biotech, Chicago, USA)

SPCImage (Becker&Hickl, Berlin, Germany)

Spcm64 (Becker&Hickl, Berlin, Germany

StatPlus (AnalystSoft, Walnut, USA)

https://www.uniprot.org/

https://www.ncbi.nlm.nih.gov/

https://www.itl.nist.gov/div898/handbook/eda/section3/eda3673.htm

7 Abbreviations

A		**I**	
A	Acceptor of Förster Resonance Energy Transfer	IMDM	Iscove's modified Dulbecco's medium
aa	Amino acid	**K**	
AAV	Adeno associated virus	kDa	Kilo Dalton
ACSF	Artificial cerebrospinal fluid	kg	Kilograms
Å	Angstroms	**L**	
B		l	Liters
BFP(s)	Blue fluorescent protein(s)	**M**	
BME	Bassal medium Eagle	M	Mol per liter
C		MCS	Multiple cloning site
CaMKII	Ca^{2+}/calmodulin-dependent protein kinase II	mEGFP	Monomeric enhanced green fluorescent protein
cAMP	Cycline adenosine-3,5-monophosphate	min	Minutes
CFP(s)	Cyan fluorescent protein(s)	ml	Milliliters
cm	Centimeters	mm	Millimeters
CMV	Cytomegalovirus	mM	Millimolar
cpVenus	Circular permutation Venus	mRFP(1)	Monomeric red fluorescent protein
C-terminus	Carboxyl terminus	ms	Milliseconds
CyPet	Cyan fluorescent protein for energy transfer	Munc13	Mammalian uncoordinated 13
D		µg	Micrograms
D	Donor of Förster Resonance Energy Transfer	µl	Microliters
DIV	Day *in vitro*	**N**	
DMEM	Dulbecco's modified Eagle's medium	NB	Neurobasal medium
DMSO	Dimethyl sulfoxide	NGS	Normal goat serum
dH_2O	Distilled water	nl	Nanoliters
DNA	Deoxyribonucleic acid	lm	Nanometers
dNTP	Deoxyribonucleotide triphosphate	ns	Nanoseconds
E		N-terminus	Amino-terminus
EBFP	Enhanced blue fluorescent protein	NTPC	Normalized total photon count
ECFP	Enhanced cyan fluorescent protein	**P**	
EGFP	Enhanced green fluorescent protein	PA-GFP	Photo-activatable green fluorescent protein
EYFP	Enhanced yellow fluorescent protein	PA-FP(s)	Photo-activatable fluorescent protein(s)
F		PBS	Phosphate buffered saline
FBS	Fetal bovine serum	PCR	Polymerase chain reaction
FD FLIM	Frequency domain fluorescence lifetime imaging microscopy	PFA	Paraformaldehyde
FLIM	Fluorescence lifetime imaging microscopy	Pen/ Strep	Penicillin/Streptomycin
FP(s)	Fluorescent protein(s)	PKA	Protein kinase A
FPLC	Fast protein liquid chromatography	PPI(s)	Protein-protein interaction(s)
FRET	Förster Resonance Energy Transfer	**R**	
fw	Forward	rAAV	Recombinant adeno associated virus
G		rev	Reverse
GFP(s)	Green fluorescent protein(s)	Rab3	Ras related in brain 3
g	Grams	RIM	Rab3 interacting molecule
H		RNA	Ribonucleic acid
h	Hours	RFP(s)	Red fluorescent protein(s)
HEBS	HEPES buffered saline	rpm	Rotation per minute
HEK 293T	Human embryonic kidney cell line 293T		

S		TCSPC	Time correlated single photon counting
s	Seconds	**U**	
SBFP2	Super blue fluorescent protein 2	U	Units
SBT	Spectral bleed-through	**V**	
SEM	Standard error of the mean	Vamp2	Vesicle associated membrane protein 2 (=Syb2)
SNARE	Soluble N-ethylmaleimide-sensitive factor (NSF) attachment protein receptors	Vglut1	Vesicular glutamate transporter 1
Syb2	Synaptobrevin 2 (=Vamp2)	**W**	
Syph1	Synaptophysin 1	wt	Wild type
Syt	Synaptotagmin	**Y**	
T		YFP(s)	Yellow fluorescent protein(s)
TBS	Tris buffered saline	YPet	Yellow fluorescent protein for energy transfer
TD FLIM	Time domain fluorescence lifetime imaging microscopy		

8 Literature

Adams, S.R. et al., 1991. Fluorescence ratio imaging of cyclic AMP in single cells. *Nature*, 349, pp.1–4.

Ai, H.-W. et al., 2006. Directed evolution of a monomeric, bright and photostable version of Clavulariacyan fluorescent protein: structural characterization and applications in fluorescence imaging. *Biochemical Journal*, 400(3), pp.531–540.

Ai, H.-W. et al., 2008. Hue-shifted monomeric variants of *Clavularia* cyan fluorescent protein: identification of the molecular determinants of color and applications in fluorescence imaging. *BMC Biology*, 6(13), pp.1–13.

Allen, M.D. & Zhang, J., 2006. Subcellular dynamics of protein kinase A activity visualized by FRET-based reporters. *Biochemical and Biophysical Research Communications*, 348(2), pp.716–721.

Aow, J., Doré, K. & Malinow, R., 2015. Conformational signaling required for synaptic plasticity by the NMDA receptor complex. *Proceedings of the National Academy of Sciences*, 112(47), pp.14711–14716.

Bajar, B., Wang, E., et al., 2016. A Guide to Fluorescent Protein FRET Pairs. *Sensors*, 16(9), pp.1488–24.

Bajar, B.T., Wang, E.S., et al., 2016. Improving brightness and photostability of green and red fluorescent proteins for live cell imaging and FRET reporting. *Nature Scientific Reports*, pp.1–12.

Balleza, E., Kim, J.M. & Cluzel, P., 2017. Systematic characterization of maturation time of fluorescent proteins in living cells. *Nature Methods*, 15(1), pp.47–51.

Becker, W., 2012. Fluorescence lifetime imaging - techniques and applications. *Journal of Microscopy*, 247(2), pp.119–136.

Berezin, M.Y. & Achilefu, S., 2010. Fluorescence Lifetime Measurements and Biological Imaging. *Chemical Reviews*, 110(5), pp.2641–2684.

Berney, C. & Danuser, G., 2003. FRET or No FRET: A Quantitative Comparison. *Biophysical Journal*, 84, pp.3992–4010.

Betzig, E. et al., 2006. Imaging intracellular fluorescent proteins at nanometer resolution. *Science*, 313(5793), pp.1642–1645.

Borden, P.Y. et al., 2017. Genetically expressed voltage sensor ArcLight for imaging large scale cortical activity in the anesthetized and awake mouse. *Neurophotonics*, 4(3), pp.031212–22.

Bossuyt, J. & Bers, D.M., 2013. Visualizing CaMKII and CaM activity: a paradigm of compartmentalized signaling. *Journal of Molecular Medicine*, 91(8), pp.907–916.

Burré, J., Sharma, M. & Südhof, T.C., 2014. α-Synuclein assembles into higher-order multimers upon membrane binding to promote SNARE complex formation. *Proceedings of the National Academy of Sciences*, 111(40), pp.E4274–E4283.

Campbell, R.E. et al., 2002. A monomeric red fluorescent protein. *PNAS*, 99(12), pp.7877–7882.

Chalfie, M. et al., 1994. Green fluorescent protein as a marker for gene expression. *Science*, 263(5148), pp.802–805.

Chance, B. et al., 1979. Oxidation-Reduction Ratio Studies of Mitochondria in Freeze-trapped Samples. *Journal of Biological Chemistry*, 254(11), pp.4764–4771.

Chen, Y. et al., 2014. A PKA activity sensor for quantitative analysis of endogenous GPCR signaling *via* 2-photon FRET-FLIM imaging. *Frontiers in Pharmacology*, 5, pp.1–12.

Cormack, B.P., Valdivia, R.H. & Falkow, S., 1995. FACS-optimized mutants of the green fluorescent protein (GFP). *Gene*, 173(1), pp.33–38.

Craggs, T.D., 2009. Green fluorescent protein: structure, folding and chromophore maturation. *Chemical Society Reviews*, 38(10), pp.2865–12.

Cubitt, A.B., Woollenweber, L.A. & Heim, R., 1999. Understanding Structure — Function Relationships in the *Aequorea victoria* Green Fluorescent Protein. 58, pp.19–30.

Day, R.N. & Davidson, M.W., 2012. Fluorescent proteins for FRET microscopy: Monitoring protein interactions in living cells. *BioEssays*, 34(5), pp.341–350.

Degtyar, V. et al., 2013. Dance of the SNAREs: Assembly and Rearrangements Detected with FRET at Neuronal Synapses. *Journal of Neuroscience*, 33(13), pp.5507–5523.

Demarco, I.A. et al., 2006. Monitoring dynamic protein interactions with photoquenching FRET. *Nature Methods*, 3(7), pp.519–524.

Depry, C., Allen, M.D. & Zhang, J., 2011. Visualization of PKA activity in plasma membrane microdomains. *Molecular BioSystems*, 7(1), pp.52–58.

Digman, M.A. et al., 2008. The Phasor Approach to Fluorescence Lifetime Imaging Analysis. *Biophysj*, 94(2), pp.L14–L16.

DiPilato, L.M. & Zhang, J., 2009. The role of membrane microdomains in shaping β2-adrenergic receptor-mediated cAMP dynamics. *Molecular BioSystems*, 5(8), pp.832–6.

Doré, K. et al., 2014. FRET-FLIM Investigation of PSD95-NMDA Receptor Interaction in Dendritic Spines; Control by Calpain, CaMKII and Src Family Kinase L. Groc, ed. *PLoS ONE*, 9(11), pp.e112170–12.

Dreosti, E. et al., 2009. A genetically encoded reporter of synaptic activity *in vivo*. *Nature Methods*, 6(12), pp.883–889.

Drobizhev, M. et al., 2009. Absolute Two-Photon Absorption Spectra and Two-Photon Brightness of Orange and Red Fluorescent Proteins. *The Journal of Physical Chemistry B*, 113(4), pp.855–859.

Drobizhev, M. et al., 2011. Two-photon absorption properties of fluorescent proteins. *Nature Methods*, 8(5), pp.393–399.

Efendiev, R. et al., 2010. AKAP79 Interacts with Multiple Adenylyl Cyclase (AC) Isoforms and Scaffolds AC5 and -6 to α-Amino-3-hydroxyl-5-methyl-4-isoxazole-propionate (AMPA) Receptors. *Journal of Biological Chemistry*, 285(19), pp.14450–14458.

Erickson, J.R. et al., 2011. Fluorescence Resonance Energy Transfer-Based Sensor Camui Provides New Insight Into Mechanisms of Calcium/Calmodulin-Dependent Protein Kinase II Activation in Intact Cardiomyocytes. *Circulation Research*, 109(7), pp.729–738.

Förster, T., 1965. Delocalized excitation and excitation transfer. In O. Sinanoglu, ed. New York: Academic Press, pp. 93–137.

Funk, K. et al., 2008. Modulation of Chloride Homeostasis by Inflammatory Mediators in Dorsal Root Ganglion Neurons. *Molecular Pain*, 4, pp.1744–8069–4–32–12.

Ganesan, S. et al., 2006. A dark yellow fluorescent protein (YFP)-based Resonance Energy-Accepting Chromoprotein (REACh) for Förster resonance energy transfer with GFP. *PNAS*, 103(11), pp.4089–4094.

Gavet, O. & Pines, J., 2010. Progressive Activation of CyclinB1-Cdk1 Coordinates Entry to Mitosis. *Developmental Cell*, 18(4), pp.533–543.

Goedhart, J. et al., 2012. Structure-guided evolution of cyan fluorescent proteins towards a quantum yield of 93%. *Nature Publishing Group*, 3(1), pp.509–9.

Gordon, S.L. & Cousin, M.A., 2013. The Sybtraps: Control of Synaptobrevin Traffic by Synaptophysin, α-Synuclein and AP-180. *Traffic*, 15(3), pp.245–254.

Gratton, E. et al., 2003. Fluorescence lifetime imaging for the two-photon microscope: time-domain and frequency-domain methods. *Journal of Biomedical Optics*, 8(3), pp.381–10.

Griesbeck, O. et al., 2001. Reducing the Environmental Sensitivity of Yellow Fluorescent Protein. *Journal of Biological Chemistry*, 276(31), pp.29188–29194.

Hanson, K.M. et al., 2002. Two-Photon Fluorescence Lifetime Imaging of the Skin Stratum Corneum pH Gradient. *Biophysj*, 83(3), pp.1682–1690.

Heim, R. & Tsien, R.Y., 1996. Engineering green fluorescent protein for improved brightness, longer wavelengths and fluorescence resonance energy transfer. *Current Biology*, 6(2), pp.178–182. Available at: https://doi.org/10.1016/S0960-9822(02)00450-5.

Hendrix, J. et al., 2008. Dark States in Monomeric Red Fluorescent Proteins Studied by Fluorescence Correlation and Single Molecule Spectroscopy. *Biophysical Journal*, 94(10), pp.4103–4113.

Hess, S.T., Girirajan, T.P.K. & Mason, M.D., 2006. Ultra-High Resolution Imaging by Fluorescence Photoactivation Localization Microscopy. *Biophysj*, 91(11), pp.4258–4272.

Inoue, S. et al., 2002. Fluorescence polarization of green fluorescence protein. *PNAS*, 99,

pp.4272–4277.

Jablonski, A., 1933. Efficiency of Anti-Stokes Fluorescence in Dyes. *Nature*, 131(3319), pp.839–840.

Joosen, L. et al., 2014. Effect of fixation procedures on the fluorescence lifetimes of *Aequorea victoria* derived fluorescent proteins. *Journal of Microscopy*, 256(3), pp.166–176.

Kaneko, H. et al., 2004. Chloride Accumulation in Mammalian Olfactory Sensory Neurons. *Journal of Neuroscience*, 24(36), pp.7931–7938.

Kim, J. et al., 2011. Quantification of protein interaction in living cells by two-photon spectral imaging with fluorescent protein fluorescence resonance energy transfer pair devoid of acceptor bleed-through. *Cytometry Part A*, 81A(2), pp.112–119.

Kim, K. & Hayashi, Y., 2014. CaMKII: the Swiss army knife of synaptic plasticity. *The Journal of Physiology*, 592(22), pp.4807–4808.

Klarenbeek, J.B. et al., 2011. A mTurquoise-Based cAMP Sensor for Both FLIM and Ratiometric Read-Out Has Improved Dynamic Range N. A. Hotchin, ed. *PLoS ONE*, 6(4), pp.e19170–6.

Koushik, S.V. et al., 2006. Cerulean, Venus, and VenusY67C FRET Reference Standards. *Biophysical Journal*, 91(12), pp.L99–L101.

Kredel, S. et al., 2009. mRuby, a Bright Monomeric Red Fluorescent Protein for Labeling of Subcellular Structures A. S. Gladfelter, ed. *PLoS ONE*, 4(2), pp.e4391–7.

Kremers, G.-J. et al., 2006. Cyan and Yellow Super Fluorescent Proteins with Improved Brightness, Protein Folding, and FRET Förster Radius †,‡. *Biochemistry*, 45(21), pp.6570–6580.

Kremers, G.-J. et al., 2009. Photoconversion in orange and red fluorescent proteins. *Nature Methods*, 6(5), pp.355–358.

Kuchibhotla, K.V. et al., 2009. Synchronous Hyperactivity and Intercellular Calcium Waves in Astrocytes in Alzheimer Mice. *Science*, 323(5918), pp.1211–1215.

Kuimova, M.K. et al., 2008. Molecular Rotor Measures Viscosity of Live Cells via Fluorescence Lifetime Imaging. *Journal of the American Chemical Society*, 130(21), pp.6672–6673.

Lakowicz, J.R., 2006. *Principles of Fluorescence Spectroscopy* 3rd ed., Springer Science.

Lam, A.J. et al., 2012. Improving FRET dynamic range with bright green and red fluorescent proteins. *Nature Methods*, 9(10), pp.1005–1012.

Laviv, T. et al., 2011. Compartmentalization of the $GABA_B$ Receptor Signaling Complex Is Required for Presynaptic Inhibition at Hippocampal Synapses. *Journal of Neuroscience*, 31(35), pp.12523–12532.

Laviv, T. et al., 2016. Simultaneous dual-color fluorescence lifetime imaging with novel

red-shifted fluorescent proteins. *Nature Methods*, 13(12), pp.989–992.

Lee, S.-J.R. et al., 2009. Activation of CaMKII in single dendritic spines during long-term potentiation. *Nature*, 458(7236), pp.299–304.

Levitt, J.A. et al., 2009. Membrane-Bound Molecular Rotors Measure Viscosity in Live Cells via Fluorescence Lifetime Imaging. *The Journal of Physical Chemistry C*, 113(27), pp.11634–11642.

Lucas, R., 2004. Detection of protein-protein interactions using the GST fusion protein pull-down technique. *Nature Methods*, 1, pp.275–276.

Ma, L. et al., 2018. A Highly Sensitive A-Kinase Activity Reporter for Imaging Neuromodulatory Events in Awake Mice. *Neuron*, 99, pp.1–21.

Marvin, J.S. et al., 2013. An optimized fluorescent probe for visualizing glutamate neurotransmission. *Nature Methods*, 10(2), pp.162–170.

Marvin, J.S. et al., 2017. Stability, affinity and chromatic variants of the glutamate sensor iGluSnFR. *bioRxiv*, pp.1–11.

Mastop, M. et al., 2017. Characterization of a spectrally diverse set of fluorescent proteins as FRET acceptors for mTurquoise2. *Nature Scientific Reports*, pp.1–18.

Matz, M.V. et al., 1999. Fluorescent proteins from nonbioluminescent Anthozoa species. *Nature Biotechnology*, 17, pp.1–5.

McPherson, A. & Gavira, J.A., 2014. Introduction to protein crystallization. *Acta Crystallographica Section F Structural Biology and Crystallization Communications*, F70, pp.2–20.

Merzlyak, E.M. et al., 2007. Bright monomeric red fluorescent protein with an extended fluorescence lifetime. *Nature Methods*, 4(7), pp.555–557.

Miyawaki, A. et al., 1997. Fluorescent indicators for Ca^{2+} based on green fluorescent proteins and calmodulin. *Nature*, 388(6645), pp.882–887.

Miyawaki, A., Sawano, A. & Kogure, T., 2003. Lighting up cells: labelling proteins with fluorophores. *Nature Cell Biology*, 5, pp.S1–S7.

Murakoshi, H., Lee, S.-J. & Yasuda, R., 2008. Highly sensitive and quantitative FRET–FLIM imaging in single dendritic spines using improved non-radiative YFP. *Brain Cell Biology*, 36(1-4), pp.31–42.

Murakoshi, H., Wang, H. & Yasuda, R., 2011. Local, persistent activation of Rho GTPases during plasticity of single dendritic spines. *Nature*, 472(7341), pp.100–104.

Nagai, T. et al., 2002. A variant of yellow fluorescent protein with fast and efficient maturation for cell-biological applications. *Nature Biotechnology*, 20, pp.87–90.

Nguyen, A.W. & Daugherty, P.S., 2005. Evolutionary optimization of fluorescent proteins for intracellular FRET. *Nature Biotechnology*, 23(3), pp.355–360.

Nikolaev, V.O. et al., 2004. Novel Single Chain cAMP Sensors for Receptor-induced Signal Propagation. *Journal of Biological Chemistry*, 279(36), pp.37215–37218.

Nooren, I.M.A. & Thornton, J.M., 2003. Structural Characterisation and Functional Significance of Transient Protein–Protein Interactions. *Journal of Molecular Biology*, 325(5), pp.991–1018.

O'Connor, D.V. & Phillips, D., 1984. *Time-Correlated Single Photon Counting*, Academic Press. Available at: https://www.sciencedirect.com/book/9780125241403/time-correlated-single-photon-counting#book-info.

Ohashi, T. et al., 2007. An experimental study of GFP-based FRET, with application to intrinsically unstructured proteins. *Protein Science*, 16(7), pp.1429–1438.

Oldach, L. & Zhang, J., 2014. Genetically Encoded Fluorescent Biosensors for Live-Cell Visualization of Protein Phosphorylation. *Chemistry & Biology*, 21(2), pp.186–197.

Olenych, S.G. et al., 2007. The Fluorescent Protein Color Palette J. S. Bonifacino et al., eds. *Current Protocols in Cell Biology*, 36(1), pp.21.5.1–21.5.34.

Otmakhov, N. et al., 2015. Excitotoxic Insult Results in a Long-Lasting Activation of CaMKIIα and Mitochondrial Damage in Living Hippocampal Neurons A. A. Mongin, ed. *PLoS ONE*, 10(3), pp.e0120881–24.

Padilla-Parra, S. et al., 2009. Quantitative Comparison of Different Fluorescent Protein Couples for Fast FRET-FLIM Acquisition. *Biophysj*, 97(8), pp.2368–2376.

Patel, N. & Gold, M.G., 2015. The genetically encoded tool set for investigating cAMP: more than the sum of its parts. *Frontiers in Pharmacology*, 6(27), pp.694–11.

Patterson, G.H., 2004. A new harvest of fluorescent proteins. *Nature Biotechnology*, 22(12), pp.1524–1525.

Patterson, G.H. & Lippincott-Schwartz, J., 2002. A photoactivatable GFP for selective photolabeling of proteins and cells. *Science*, 297(5588), pp.1873–1877. Available at: http://www.sciencemag.org/cgi/doi/10.1126/science.1074952.

Perkins, J.R. et al., 2010. Transient Protein-Protein Interactions: Structural, Functional, and Network Properties. *Structure/Folding and Design*, 18(10), pp.1233–1243.

Peulen, T.-O., Opanasyuk, O. & Seidel, C.A.M., 2017. Combining Graphical and Analytical Methods with Molecular Simulations To Analyze Time-Resolved FRET Measurements of Labeled Macromolecules Accurately. *The Journal of Physical Chemistry B*, 121(35), pp.8211–8241.

Phizicky, E.M. & Fields, S., 1995. Protein-Protein Interactions: Methods for Detection and Analysis. *Microbiological Reviews*, 59(1), pp.94–123.

Piatkevich, K.D. et al., 2010. Red fluorescent proteins and their properties. *Russian Chemical Reviews*, 79(3), pp.243–258.

Piston, D.W. & Kremers, G.-J., 2007. Fluorescent protein FRET: the good, the bad and the ugly. *Trends in Biochemical Sciences*, 32(9), pp.407–414.

Raimondo, J.V. et al., 2013. A genetically-encoded chloride and pH sensor for dissociating ion dynamics in the nervous system. *Frontiers in Cellular Neuroscience*, 7(202), pp.1–10.

Rajappa, R. et al., 2016. Synaptophysin 1 Clears Synaptobrevin 2 from the Presynaptic Active Zone to Prevent Short-Term Depression. *CellReports*, 14(6), pp.1369–1381.

Remington, S.J., 2006. Fluorescent proteins: maturation, photochemistry and photophysics. *Current Opinion in Structural Biology*, 16(6), pp.714–721.

Rickman, C. & Duncan, R.R., 2010. Munc18/Syntaxin Interaction Kinetics Control Secretory Vesicle Dynamics. *Journal of Biological Chemistry*, 285(6), pp.3965–3972.

Rizzo, M.A., Springer, G.H., Granada, B. & Piston, D.W., 2004a. An improved cyan fluorescent protein variant useful for FRET. *Nature Biotechnology*, 22(4), pp.445–449.

Rizzo, M.A., Springer, G.H., Granada, B. & Piston, D.W., 2004b. An improved cyan fluorescent protein variant useful for FRET. *Nature Biotechnology*, 22(4), pp.445–449.

Royant, A. et al., 2007. Advances in spectroscopic methods for biological crystals. 1. Fluorescence lifetime measurements. *Journal of Applied Crystallography*, 40(6), pp.1105–1112.

Sanders, R. et al., 1995. Quantitative pH Imaging in Cells Using Confocal Fluorescence Lifetime Imaging Microscopy. *Analytical Biochemistry*, 227(2), pp.302–308.

Schindelin, J. et al., 2012. Fiji: an open-source platform for biological-image analysis. *Nature Methods*, 9(7), pp.676–682. Available at: https://www.nature.com/articles/nmeth.2019.pdf.

Sekar, R.B. & Periasamy, A., 2003. Fluorescence resonance energy transfer (FRET) microscopy imaging of live cell protein localizations. *The Journal of Cell Biology*, 160(5), pp.629–633.

Shagin, D.A. et al., 2004. GFP-like Proteins as Ubiquitous Metazoan Superfamily: Evolution of Functional Features and Structural Complexity. *Molecular Biology and Evolution*, 21(5), pp.841–850.

Shaner, N.C. et al., 2013. A bright monomeric green fluorescent protein derived from Branchiostoma lanceolatum. *Nature Methods*, 10(5), pp.407–409.

Shaner, N.C. et al., 2004. Improved monomeric red, orange and yellow fluorescent proteins derived from Discosoma sp. red fluorescent protein. *Nature Biotechnology*, 22(12), pp.1567–1572.

Shaner, N.C. et al., 2008. Improving the photostability of bright monomeric orange and red fluorescent proteins. *Nature Methods*, 5(6), pp.545–551.

Shaner, N.C., Patterson, G.H. & Davidson, M.W., 2007. Advances in fluorescent protein technology. *Journal of Cell Science*, 120(24), pp.4247–4260.

Shen, Y. et al., 2017. Engineering of mCherry variants with long Stokes shift, red-shifted fluorescence, and low cytotoxicity K. I. Anderson, ed. *PLoS ONE*, 12(2),

pp.e0171257–14.

Shibata, A.C.E. et al., 2015. Development of a Molecularly Evolved, Highly Sensitive CaMKII FRET Sensor with Improved Expression Pattern Y. Wang, ed. *PLoS ONE*, 10(3), pp.e0121109–22.

Shimomura, O., Johnson, F.H. & Saiga, Y., 1962. Extraction, Purification and Properties of Aequorin, a Bioluminescent Protein from the Luminous Hydromedusan, Aequorea. 59(3), pp.223–239.

Shkrob, M.A. et al., 2005. Far-red fluorescent proteins evolved from a blue chromoprotein from Actinia equina. *Biochemical Journal*, 392(3), pp.649–654.

Smith, K.E., 2006. cAMP-Dependent Protein Kinase Postsynaptic Localization Regulated by NMDA Receptor Activation through Translocation of an A-Kinase Anchoring Protein Scaffold Protein. *Journal of Neuroscience*, 26(9), pp.2391–2402.

Sniegowski, J.A. et al., 2005. Base Catalysis of Chromophore Formation in Arg 96and Glu 222Variants of Green Fluorescent Protein. *Journal of Biological Chemistry*, 280(28), pp.26248–26255.

Stokes, G.G., 1852. On the change of refrangibility of light. *Philosophcial Transactions of the Royal Society*, 142, pp.463–562.

Stryer, L., 1978. Fluorescence Energy Transfer as a Spectroscopic Ruler. *Annual Review of Biochemistry*, 47, pp.819–846.

Sun, Y., Day, R.N. & Periasamy, A., 2011. Investigating protein-protein interactions in living cells using fluorescence lifetime imaging microscopy. *Nature Protocols*, 6(9), pp.1324–1340.

Szmacinski, H., Toshchakov, V. & Lakowicz, J.R., 2014. Application of phasor plot and autofluorescence correction for study of heterogeneous cell population. *Journal of Biomedical Optics*, 19(4), pp.046017–10.

Takahashi, N. et al., 1AD. Two-photon fluorescence lifetime imaging of primed SNARE complexes in presynaptic terminals and β cells. *Nature Communications*, 6, pp.1–15.

Ting, A.Y. et al., 2001. Genetically encoded fluorescent reporters of protein tyrosine kinase activities in living cells. *Proceedings of the National Academy of Sciences*, 98(26), pp.15003–15008.

Tramier, M. et al., 2006. Sensitivity of CFP/YFP and GFP/mCherry pairs to donor photobleaching on FRET determination by fluorescence lifetime imaging microscopy in living cells. *Microscopy Research and Technique*, 69(11), pp.933–939.

Treanor, B. et al., 2005. Imaging fluorescence lifetime heterogeneity applied to GFP-tagged MHC protein at an immunological synapse. *Journal of Microscopy*, 217(1), pp.36–43.

Tsien, R.Y., 1998. The Green Fluorescent Protein. *Annual Review of Biochemistry*, pp.1–38.

van Zandvoort, M.A.M.J. et al., 2002. Discrimination of DNA and RNA in cells by a vital fluorescent probe: Lifetime imaging of SYTO13 in healthy and apoptotic cells. *Cytometry Part A*, 47(4), pp.226–235.

Vinkenborg, J.L. et al., 2007. Enhanced Sensitivity of FRET-Based Protease Sensors by Redesign of the GFP Dimerization Interface. *ChemBioChem*, 8(10), pp.1119–1121.

Wahl, M., 2014. *Time-Correlated Single Photon Counting*, Available at: https://www.picoquant.com/images/uploads/page/files/7253/technote_tcspc.pdf.

Wall, M.A., Socolich, M. & Ranganathan, R., 2000. The structural basis for red fluorescence in the tetrameric GFP homolog DsRed. *Nature Structural Biology*, 7(12), pp.1–6.

Wallrabe, H. & Periasamy, A., 2005. Imaging protein molecules using FRET and FLIM microscopy. *Current Opinion in Biotechnology*, 16(1), pp.19–27.

Wang, L. et al., 2004. Evolution of new nonantibody proteins via iterative somatic hypermutation. *PNAS*, 101(48), pp.16745–16749.

Woitecki, A.M.H. et al., 2016. Identification of Synaptotagmin 10 as Effector of NPAS4-Mediated Protection from Excitotoxic Neurodegeneration. *Journal of Neuroscience*, 36(9), pp.2561–2570.

Wood, T.I. et al., 2005. Defining the Role of Arginine 96 in Green Fluorescent Protein Fluorophore Biosynthesis. *Biochemistry*, 44(49), pp.16211–16220.

Yang, Y. et al., 2018. Improved calcium sensor GCaMP-X overcomes the calcium channel perturbations induced by the calmodulin in GCaMP. *Nature Communications*, 9(1504), pp.1–18.

Yarbrough, D. et al., 2001. Refined crystal structure of DsRed, a red fluorescent protein from coral, at 2.0-Å resolution. *PNAS*, 98(2), pp.462–467.

Ye, L. et al., 2017. Comparison of GCaMP3 and GCaMP6f for studying astrocyte Ca2+ dynamics in the awake mouse brain A. Guerrero-Hernandez, ed. *PLoS ONE*, 12(7), pp.e0181113–17.

Zacharias, D.A., 2002. Partitioning of Lipid-Modified Monomeric GFPs into Membrane Microdomains of Live Cells. *Science*, 296(5569), pp.913–916.

Zhou, X., Herbst-Robinson, K.J. & Zhang, J., 2012. *Visualizing Dynamic Activities of Signaling Enzymes Using Genetically Encodable FRET-Based Biosensors: From Designs to Applications* 1st ed., Elsevier Inc.

9 Acknowledgments

The realization of my work would not be possible without the help and support of others and I would like to express my gratitude to them.

I would like to cordially thank Prof. Dr. Susanne Schoch and Prof. Dr. Dirk Dietrich for giving me the opportunity to work in their labs, for their mentorship, optimism, enthusiasm and humor. It was a great experience and pleasure to work with them; they were the best mentors I could wish for.

I would also like to thank Prof. Dr. Walter Witke for being the co-advisor and Prof. Dr. Alf Lamprecht for being a part of my thesis committee.

I thank Prof. Dr. Matthias Geyer, Prof. Dr. Heinz Beck, Prof. Dr. Christian Henneberger and Prof. Dr. Albert Becker for their helpful comments and questions, for the opportunity to collaborate with them in various projects.

Deep gratitude to the technical assistants of the lab, especially to Sabine Opitz, who was preparing tons of great cultured neurons, giving helpful advices and being a great friend.

A huge thanks to all the master students helping me with the project especially to Dnyanada Sahasrabudhe aka Nano.

Thanks to the whole AG Schecker and AG Dietrich for their help, support and friendship.

Thanks to all my friends for their patience to my complaints and their support. Both my Russian friends Анюта, Ира, Оксич, Олич, Олька, Катя and my foreign friends Alex, Annachiara, Annechen, Annika, Arlind, Chrysa, Gunther, Hyuntae, Idil, Julia Bungenberg, Julia Kühn, Silvia and others (listed alphabetically XD).

Special thanks goes to my family: my mom, my grandma, Женька1, Женька2, Алиска, and of course to my dear Мэнчик. Finally, I would like to thank my musculoskeletal system for all the support it has been giving me all these years.